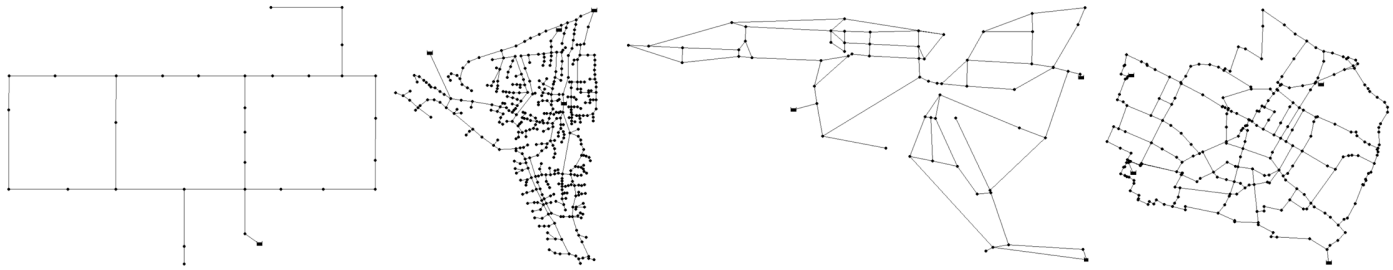
Supplementary Materials – Fractal Dimension as a Criterion for the Optimal Design and Operation of Water Distribution Systems

This supplementary material presents the detailed results obtained from the application of fractal analysis on the mono-objective and bi-objective design outcomes considering the benchmark water distribution systems (WDS) used in this research. Additional information specific to the hydraulic design methodologies and fractal analysis results and algorithms is available by contacting the authors.

1. Case Studies

Four benchmark water distribution systems with distinct sizes, topologies and design constraints were considered in this study: Hanoi, Balerma, Pescara and Modena. Figure S1 presents the considered case studies. Table S1 presents the main characteristics of these case studies. Table S2 presents the diameter options of each case study according to the literature.



(a) *(b)* *(c)* *(d)*

Figure S1. Case studies: (a) Hanoi; (b) Balerma; (c) Pescara; (d) Modena.

Table S1. Characteristics of the case studies.

Network	Nodes	Pipes	Reservoirs	Pressure Constraints	Velocity Constraints	Search Space (Wang et al., 2015)	Problem Size (Wang et al., 2015)	OHGS (Jaramillo & Saldarriaga, 2023)
Hanoi (Fujiwara & Khang, 1990)	31	34	1	p_{min} 30 m	No	$2.87 \cdot 10^{26}$	Medium	2.0214
Balerma (Reca & Martínez, 2006)	443	454	4	p_{min} 20 m	No	$1.00 \cdot 10^{455}$	Large	2.2982
Pescara (Bragalli et al., 2012)	68	99	3	p_{min} 20 m p_{max} variable	v_{max} 2 m/s	$1.91 \cdot 10^{110}$	Intermediate	2.3125
Modena (Bragalli et al., 2012)	268	317	4	p_{min} 20 m p_{max} variable	v_{max} 2 m/s	$1.32 \cdot 10^{353}$	Large	2.3204

Table S2. Diameter options of the case studies.

Network	Diameters
Hanoi (Fujiwara & Khang, 1990)	{12 in, 16.0 in, 20.0 in, 24.0 in, 30.0 in, 40 in}

Balerma (Fujiwara & Khang, 1990)	{113 mm, 126.6 mm, 144.6 mm, 162.8 mm, 180.8 mm, 226.2 mm, 285 mm, 361.8 mm, 452.2 mm, 581.8 mm}
Pescara (Bragalli et al., 2012)	{100 mm, 125 mm, 150 mm, 200 mm, 250 mm, 300 mm, 350 mm, 400 mm, 450 mm, 500 mm, 600 mm, 700 mm, 800 mm}
Modena (Bragalli et al., 2012)	{100 mm, 125 mm, 150 mm, 200 mm, 250 mm, 300 mm, 350 mm, 400 mm, 450 mm, 500 mm, 600 mm, 700 mm, 800 mm}

2. Design Parameters

2.1. OPUS

The OPUS methodology was employed using the parameters proposed by Saldarriaga et al. (2020). Hence, to obtain the Optimal Power Use Surface (OPUS) designs, the main calibrated parameters correspond to the topological properties of each water distribution system (WDS), the constructive cost function (C), the set of pipe materials and commercial diameters (d) for each case study, as well as the hydraulic modelling equations, the sag value (F), the benefit/cost (B/C) relationship, the potential round-off exponent (b), the equation for recalculating the sag (F) value and the chosen arrangement criterion of the optimization step. Table S3 shows the base parameters used to obtain the OPUS–designed water distribution systems (WDS).

Table S1. Parameters, OPUS methodology. Adapted from Saldarriaga et al. (2020).

Network	Hydraulic Equation	Roughness	C	F	F Equation	B/C	b	Arrangement Criterion
Hanoi	Hazen – Williams	C 130	$1.1002d^{1.500}$ $/in	0.25	Highest Pressure	Highest Relation	2.6	H/L
Balerma	Darcy – Weisbach	k_s 0.0025 mm	$0.0004d^{2.0618}$ €/mm	0.25	Highest Pressure	Highest Relation	2.6	H/L
Pescara	Hazen – Williams	C 130	$0.0728d^{1.2702}$ €/mm	0.10	Highest Pressure	Highest Relation	2.6	H/L
Modena	Hazen – Williams	C 130	$0.0728d^{1.2702}$ €/mm	0.20	Highest Pressure	Highest Relation	2.6	H/L

2.2. NSGA-II and OPUS/NSGA-II

To study the variation of the fractal dimension (D) through sets of feasible designs of varying costs, NSGA-II and OPUS/NSGA-II were implemented following the methodology proposed by Páez et al. (2020). To implement NSGA-II, it was necessary to calibrate the number of individuals, the number of generations, the mutation distribution index, the crossover distribution Index, the probability of crossover and the probability of mutation.

To implement OPUS/NSGA-II, the retrofitted frequency, and the equation of OPUS-recommended diameters for each study case were calibrated as well. The probability of crossover and the probability of mutation remained constant and equal to 0.9 and 0.1 in both implementations. Table S4 shows the parameters used to obtain the non-dominated Pareto Fronts (PF) through the mentioned multi-objective water distribution system (WDS) design methodologies.

Table S2. Parameters, NSGA-II and OPUS/NSGA-II. Adapted from Páez et al.(2020).

Network	Hydraulic Equation	Roughness	C	Individuals	Generations	Mutation Distribution Index	Crossover Distribution Index	Retrofitted Frequency
Hanoi	Hazen – Williams	C 130	$1.1002d^{1.500}$ $/in	500	500	20	3	5

Balerma	Darcy – Weisbach	k_s 0.0025 mm	$0.0004d^{2.0618}$ €/mm	2000	4500	100	2	10
Pescara	Hazen – Williams	C 130	$0.0728d^{1.2702}$ €/mm	500	2000	100	10	20
Modena	Hazen – Williams	C 130	$0.0728d^{1.2702}$ €/mm	2000	4000	20	7	50

2.3. GALAXY

In this study, GALAXY was employed to gain a deeper understanding of the behavior of the fractal dimension (D) and its implications in water distribution system (WDS) design. GALAXY is a hybrid, more recent bi-objective optimization methodology that builds upon previous methodologies of water distribution system (WDS) design. This study uses the implementation of GALAXY proposed by Wang et al. (2017). Unlike the implementation of NSGA-II and OPUS/NSGA-II, GALAXY only requires the specification of the population size, the number of function evaluations and the probability of dither creeping mutation (P_{dcm}) used in the dither creeping (DC) operator (see Table S5).

Table S3. Parameters, GALAXY. Adapted from Wang et al. (2017).

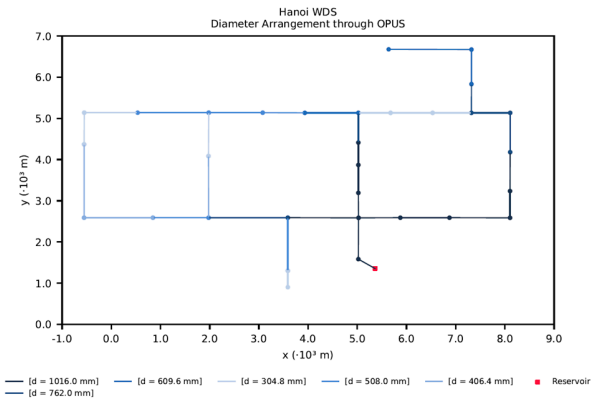
Network	Hydraulic Equation	Material	C	Population Size	Function Evaluations	P_{dcm}
Hanoi	Hazen – Williams	C 130	$1.1002d^{1.500}$ $/in	100	50000	0.7
Balerma	Darcy – Weisbach	k_s 0.0025 mm	$0.0004d^{2.0618}$ €/mm	200	400000	0.7
Pescara	Hazen – Williams	C 130	$0.0728d^{1.2702}$ €/mm	100	100000	0.7
Modena	Hazen – Williams	C 130	$0.0728d^{1.2702}$ €/mm	200	40000	0.7

3. Detailed Results

3.1. Mono – Objective Approach

3.1.1. Hanoi

Figure S2 presents the diameters and the computed fractal fractal dimensions (D) of the design of Hanoi obtained through the Optimal Power Use Surface (OPUS) methodology. Table S6 presents the magnitudes of the computed fractal dimensions (D) of the mono-objective design. Figure S3 presents the hydraulic gradient surface (HGS) of the mono-objective design. Table S7 presents statistics of the hydraulic gradient line (HGL) magnitudes at the nodes, the distribution of diameters (d) at the pipes and the flow rates (Q) at the nodes of the mono-objective design.



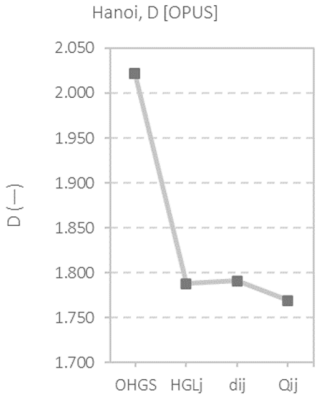


Table S6. Fractal dimensions (D). Hanoi, OPUS

D, OHGS	2.021	
w_j	D	R^2
HGL_j	1.788	0.999
d_{ij}	1.791	0.999
Q_{ij}	1.769	0.999

Figure S2. Hanoi, OPUS: (a) diameters of the design outcome; (b) computed fractal dimensions (D).

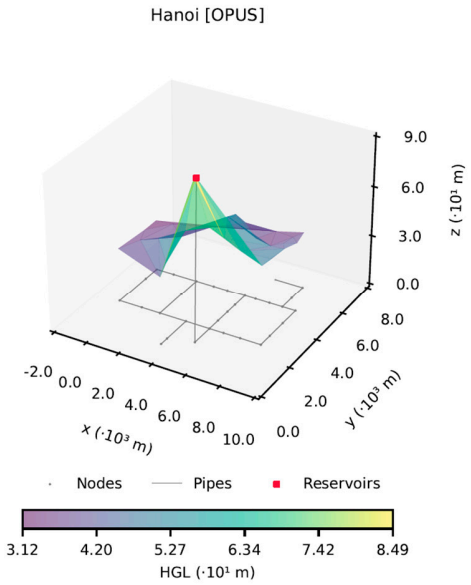


Figure S3. Hydraulic gradient surface (HGS) of Hanoi – OPUS.

Table S7. Statistics of the energy (HGL), infrastructural (d) and flow (Q) distributions, Hanoi – OPUS.

Hanoi, OPUS		Hanoi, OPUS		Hanoi, OPUS	
HGL (m)		d (m)		Q (m^3/s)	
Q1	35.938	Q1	0.406	Q1	0.205
Q2	42.179	Q2	0.610	Q2	0.542
Q3	53.729	Q3	1.016	Q3	1.378
σ	16.148	σ	0.279	σ	1.260
Min	16.148	Min	0.305	Min	0.013
Mean	46.853	Mean	0.668	Mean	0.966
Max	100.000	Max	1.016	Max	5.539

3.1.2. Balerma

Figure S4 presents the diameters and the computed fractal fractal dimensions (D) of the design of Balerma obtained through the Optimal Power Use Surface (OPUS) methodology. Table S8 presents the magnitudes of the computed fractal dimensions (D) of the mono-objective design. Figure S5 presents the hydraulic gradient surface (HGS) of the mono-objective design. Table S9 presents statistics of the hydraulic gradient line (HGL) magnitudes at the nodes, the distribution of diameters (d) at the pipes and the flow rates (Q) at the nodes of the mono-objective design.

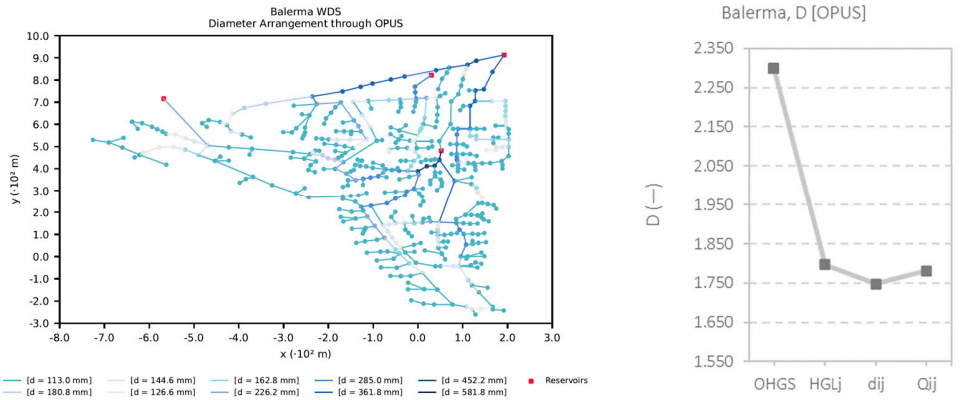


Figure S4. Balerma, OPUS: (a) diameters of the design outcome; (b) computed fractal dimensions (D).

Table S8. Fractal dimensions (D).

Balerma, OPUS		
D, OHGS	2.298	
w_j	D	R^2
HGL_j	1.796	0.999
d_{ij}	1.748	1.000
Q_{ij}	1.781	1.000

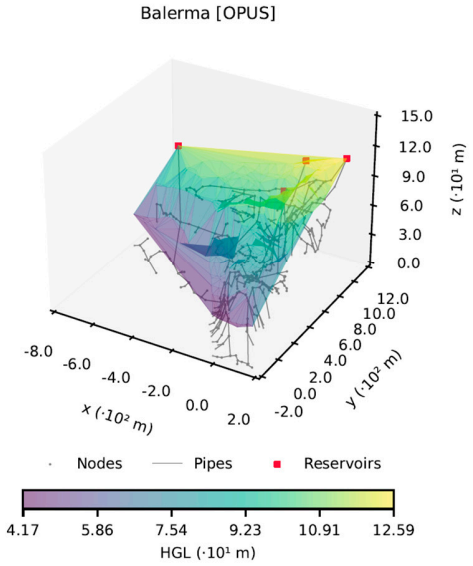


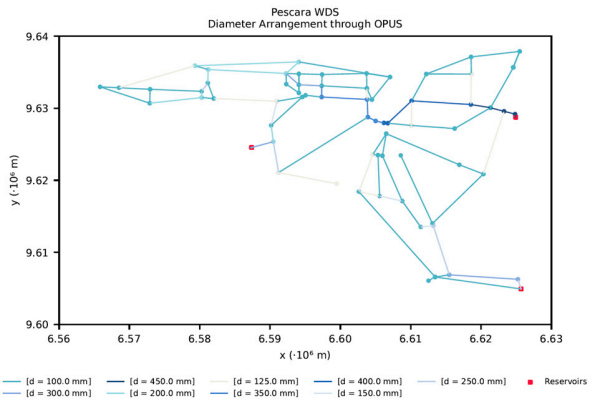
Figure S5. Hydraulic gradient surface (HGS) of Hanoi – OPUS.

Table S9. Statistics of the energy (HGL), infrastructural (d) and flow (Q) distributions, Balerma – OPUS.

Balerma, OPUS		Balerma, OPUS		Balerma, OPUS	
HGL (m)		d (m)		Q (m^3/s)	
Q1	79.194	Q1	0.113	Q1	0.002
Q2	96.516	Q2	0.113	Q2	0.007
Q3	107.969	Q3	0.145	Q3	0.023
σ	20.921	σ	0.072	σ	0.052
Min	41.542	Min	0.113	Min	0.000
Mean	91.741	Mean	0.150	Mean	0.027
Max	127	Max	0.582	Max	0.598

3.1.3. Pescara

Figure S6 presents the diameters and the computed fractal fractal dimensions (D) of the design of Pescara obtained through the Optimal Power Use Surface (OPUS) methodology. Table S10 presents the magnitudes of the computed fractal dimensions (D) of the mono-objective design. Figure S7 presents the hydraulic gradient surface (HGS) of the mono-objective design. Table S11 presents statistics of the hydraulic gradient line (HGL) magnitudes at the nodes, the distribution of diameters (d) at the pipes and the flow rates (Q) at the nodes of the mono-objective design.



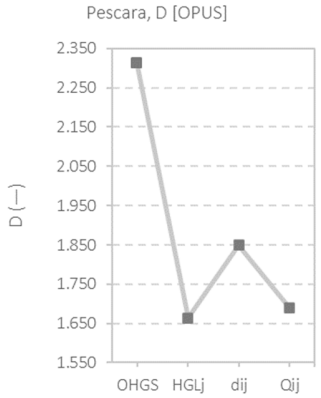


Table S10. Fractal dimensions (D).

Pescara, OPUS		
D, OHGS	2.313	
w_j	D	R^2
HGL_j	1.664	0.997
d_{ij}	1.849	0.999
Q_{ij}	1.689	0.998

Figure S6. Pescara, OPUS: (a) diameters of the design outcome; (b) computed fractal dimensions (D).

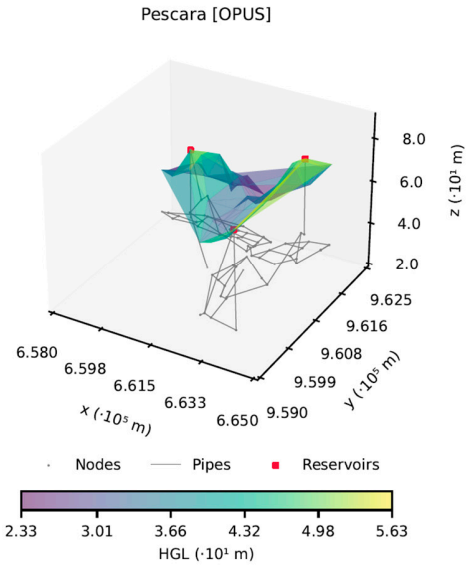


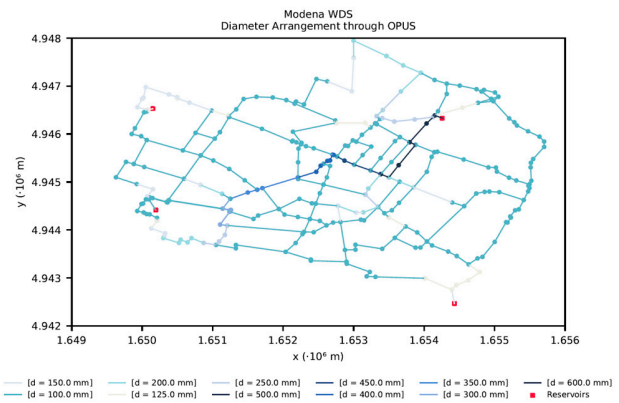
Figure S7. Hydraulic gradient surface (HGS) of Pescara – OPUS.

Table S11. Statistics of the energy (HGL), infrastructural (d) and flow (Q) distributions, Pescara – OPUS.

Pescara, OPUS		Pescara, OPUS		Pescara, OPUS	
HGL (m)		d (m)		Q (m^3/s)	
Q1	33.658	Q1	0.100	Q1	0.004
Q2	41.845	Q2	0.100	Q2	0.007
Q3	47.425	Q3	0.300	Q3	0.030
σ	9.220	σ	0.212	σ	0.063
Min	23.136	Min	0.100	Min	0.000
Mean	40.921	Mean	0.238	Mean	0.037
Max	57.000	Max	0.800	Max	0.268

3.1.4. Modena

Figure S8 presents the diameters and the computed fractal fractal dimensions (D) of the design of Modena obtained through the Optimal Power Use Surface (OPUS) methodology. Table S12 presents the magnitudes of the computed fractal dimensions (D) of the mono-objective design. Figure S9 presents the hydraulic gradient surface (HGS) of the mono-objective design. Table S13 presents statistics of the hydraulic gradient line (HGL) magnitudes at the nodes, the distribution of diameters (d) at the pipes and the flow rates (Q) at the nodes of the mono-objective design.



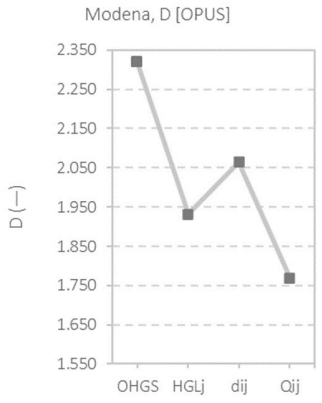


Table S12. Fractal dimensions (D).

Modena, OPUS		
D, OHGS	2.320	
w_j	D	R^2
HGL_j	1.932	0.998
d_{ij}	2.065	0.996
Q_{ij}	1.769	0.999

Figure S8. Modena, OPUS: (a) diameters of the design outcome; (b) computed fractal dimensions (D).

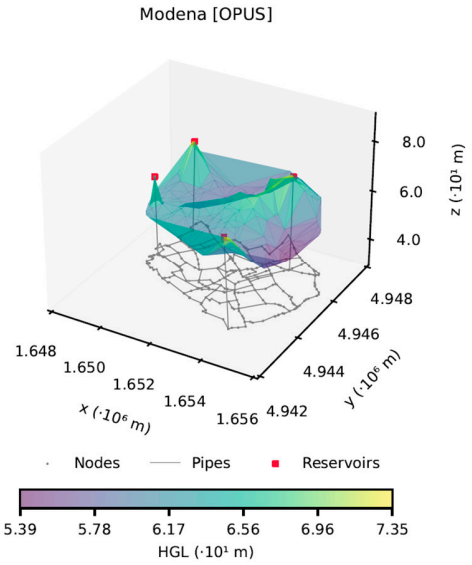


Figure S9. Hydraulic gradient surface (HGS) of Modena – OPUS.

Table S13. Statistics of the energy (HGL), infrastructural (d) and flow (Q) distributions, Modena – OPUS.

Modena, OPUS		Modena, OPUS		Modena, OPUS	
HGL (m)		d (m)		Q (m^3/s)	
Q1	59.519	Q1	0.100	Q1	0.002
Q2	61.725	Q2	0.100	Q2	0.004
Q3	64.222	Q3	0.200	Q3	0.010
σ	4.254	σ	0.130	σ	0.045
Min	53.809	Min	0.100	Min	0.000
Mean	62.045	Mean	0.168	Mean	0.018
Max	74.500	Max	0.800	Max	0.331

3.2. Bi – Objective Approach

3.2.1. Hanoi

Figure S10 shows the non-dominated Pareto Fronts (PF) of Hanoi obtained through the application of NSGA-II (Deb et al., 2022), OPUS/NSGA-II (Páez et al., 2020) and GALAXY (Wang et al., 2017).

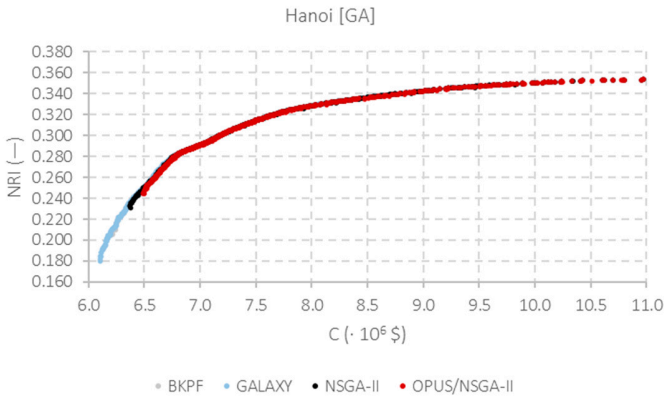


Figure S10. Hanoi, genetic algorithms. Note: Note: BKPF refers to the Best-Known Pareto Front found in the literature (Wang et al., 2015).

3.2.1.1. GALAXY

Figure S11 shows the non-dominated Pareto Front (PF) of Hanoi obtained through the application of GALAXY [18]. Figure S12 shows the hydraulic gradient surface (HGS) of the [min(C), min(D)], [knee(C), knee(NRI)], [max(C), max(NRI)] design outcomes representing the extreme values of the energy (HGL) infrastructural (d) and flow distribution patterns of Hanoi through this design methodology. Figure S13 shows the achieved fractal dimension (D) of the extreme GALAXY bi-objective designs. Table S14 shows the magnitudes of the fractal dimensions (D) of the extreme GALAXY bi-objective designs of Hanoi.

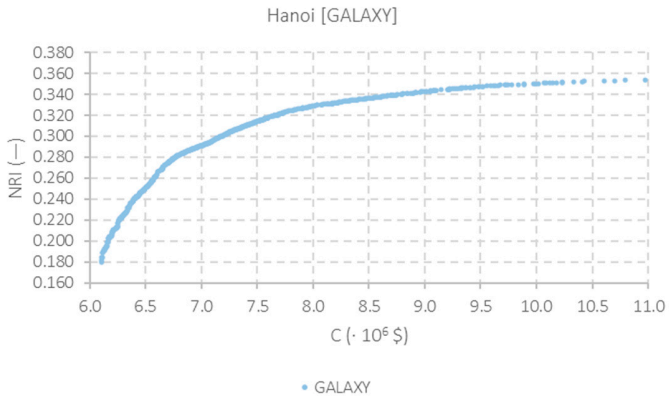
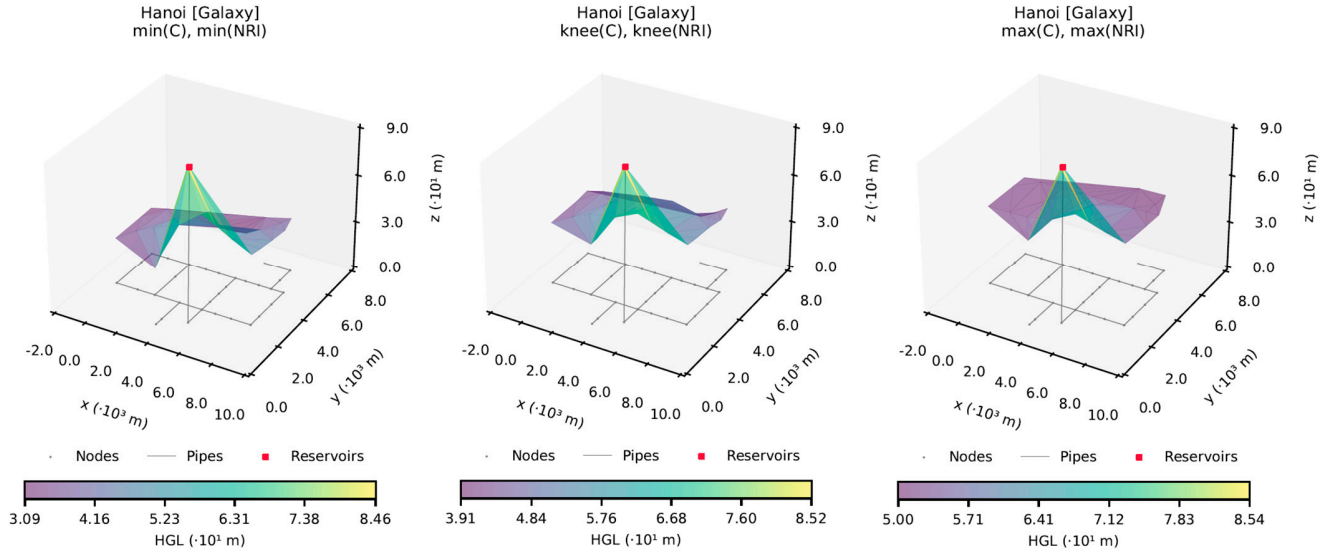
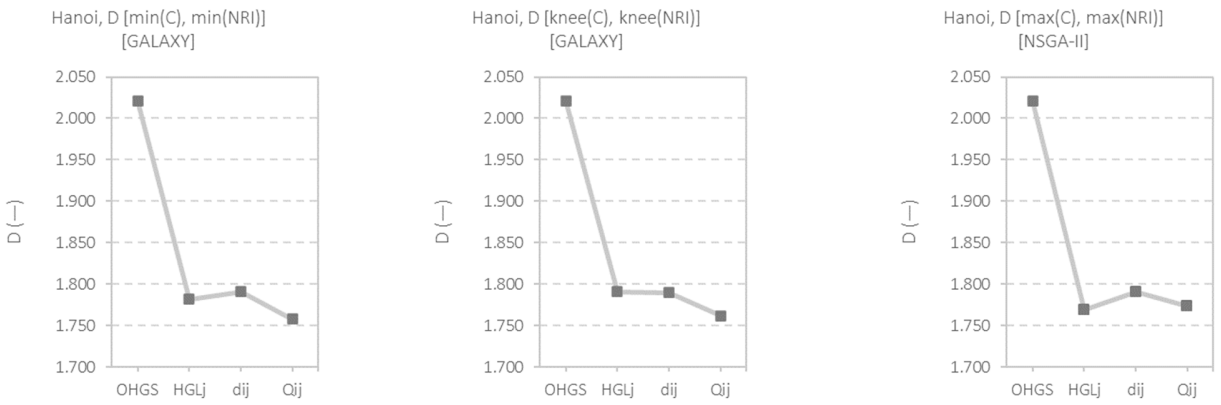


Figure S11. Hanoi, GALAXY, Pareto Front (PF).



(a) *(b)* *(c)*

Figure S12. Hanoi, GALAXY, hydraulic gradient surfaces (HGS): (a) [min(C), min(NRI)]; (b) [knee(C), knee(NRI)]; (c) [max(C), max(NRI)].



(a) *(b)* *(c)*

Figure S13. Hanoi, GALAXY, fractal dimensions (D): (a) [min(C), min(NRI)]; (b) [knee(C), knee(NRI)]; (c) [max(C), max(NRI)].

Table S14. Fractal dimensions (D) of the extreme GALAXY bi-objective designs of Hanoi.

Hanoi [min(C), min(NRI)] GALAXY			Hanoi [knee(C), knee(NRI)] GALAXY			Hanoi [max(C), max(NRI)] GALAXY		
D, OHGS	2.021		D, OHGS	2.021		D, OHGS	2.021	
w_j	D	R^2	w_j	D	R^2	w_j	D	R^2
HGL_j	1.782	0.999	HGL_j	1.791	0.999	HGL_j	1.769	0.999
d_{ij}	1.791	0.999	d_{ij}	1.790	0.999	d_{ij}	1.791	0.999
Q_{ij}	1.758	0.999	Q_{ij}	1.762	0.999	Q_{ij}	1.773	0.999

Figure S14 shows the fractal dimensions (D) of the individuals of the non-dominated Pareto Front (PF) obtained through GALAXY organized from minimum constructive cost (C) to maximum constructive cost (C). Figure S15 shows statistics of the design individuals obtained by the implementation of this methodology. Figure S16 to Figure S18 show the box whiskers plot of the fractal dimensions (D) considering the energy (HGL_j), infrastructure (d_{ij}) and flow (Q_{ij}) distribution patterns of each resulting individual. Finally, Table S15 to Table S17 show relevant statistics of the computed fractal dimensions (D) and the determination coefficients (R^2) associated to each computation.

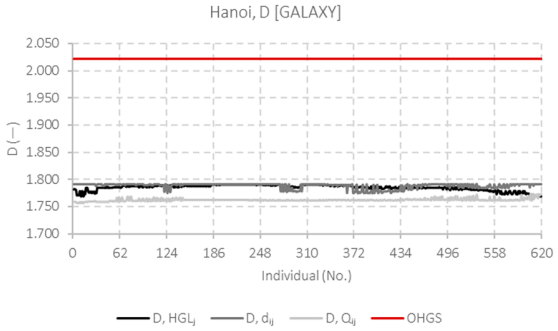
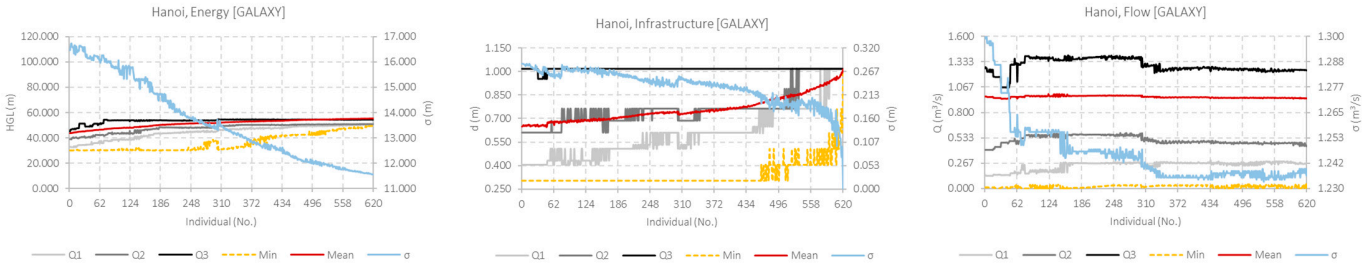


Figure S14. Hanoi, GALAXY, fractal dimensions (D).



(a) *(b)* *(c)*

Figure S15. Hanoi, GALAXY, statistics of the non-dominated individuals: (a) energy (HGL); (b) infrastructure (d); (c) flow (Q).

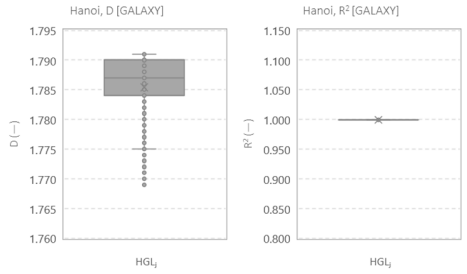


Figure S16. Hanoi, GALAXY, box whiskers plots, $w_j = HGL_j$: (a) fractal dimensions (D); (b) determination coefficients (R^2).

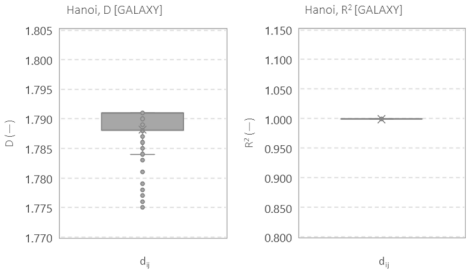


Figure S17. Hanoi, GALAXY, box whiskers plots, $w_j = d_{ij}$: (a) fractal dimensions (D); (b) determination coefficients (R^2).

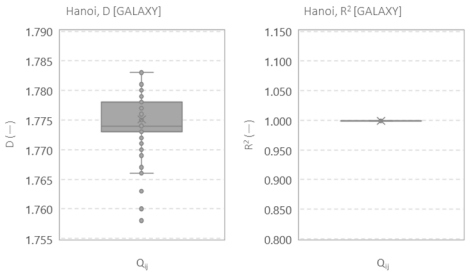


Figure S18. Hanoi, GALAXY, box whiskers plots, $w_j = Q_{ij}$: (a) fractal dimensions (D); (b) determination coefficients (R^2).

Table S15. Hanoi, GALAXY, statistics, $w_j = HGL_j$: (a) fractal dimensions (D); (b) determination coefficients (R^2).

Hanoi, GALAXY		Hanoi, GALAXY	
D, HGL_j		R^2, HGL_j	
Q1	1.784	Q1	0.999
Q2	1.787	Q2	0.999
Q3	1.790	Q3	0.999
σ	$5.424 \cdot 10^{-3}$	σ	$1.244 \cdot 10^{-14}$
Min	1.769	Min	0.999
Mean	1.785	Mean	0.999
Max	1.791	Max	0.999

Table S16. Hanoi, GALAXY, statistics, $w_j = d_{ij}$: (a) fractal dimensions (D); (b) determination coefficients (R^2).

Hanoi, GALAXY		Hanoi, GALAXY	
D, d_{ij}		R^2, d_{ij}	
Q1	1.788	Q1	0.999
Q2	1.791	Q2	0.999
Q3	1.791	Q3	0.999
σ	$4.752 \cdot 10^{-3}$	σ	$1.244 \cdot 10^{-14}$
Min	1.775	Min	0.999
Mean	1.788	Mean	0.999
Max	1.791	Max	0.999

Table S17. Hanoi, GALAXY, statistics, $w_j = Q_{ij}$: (a) fractal dimensions (D); (b) determination coefficients (R^2).

Hanoi, GALAXY		Hanoi, GALAXY	
D, Q_{ij}		R^2, Q_{ij}	
Q1	1.761	Q1	0.999
Q2	1.762	Q2	0.999
Q3	1.762	Q3	0.999
σ	$2.567 \cdot 10^{-3}$	σ	$1.244 \cdot 10^{-14}$
Min	1.756	Min	0.999
Mean	1.762	Mean	0.999
Max	1.773	Max	0.999

3.2.1.2. NSGA-II

Figure S19 shows the non-dominated Pareto Front (PF) of Hanoi obtained through the application of NSGA-II [17]. Figure S20 shows the hydraulic gradient surface (HGS) of the [min(C), min(D)], [knee(C), knee(NRI)], [max(C), max(NRI)] design outcomes representing the extreme values of the energy (HGL) infrastructural (d) and flow distribution patterns of Hanoi through this design methodology. Figure S21 shows the achieved fractal dimension (D) of the extreme NSGA-II bi-objective designs. Table S18 shows the magnitudes of the fractal dimensions (D) of the extreme NSGA-II bi-objective designs of Hanoi.

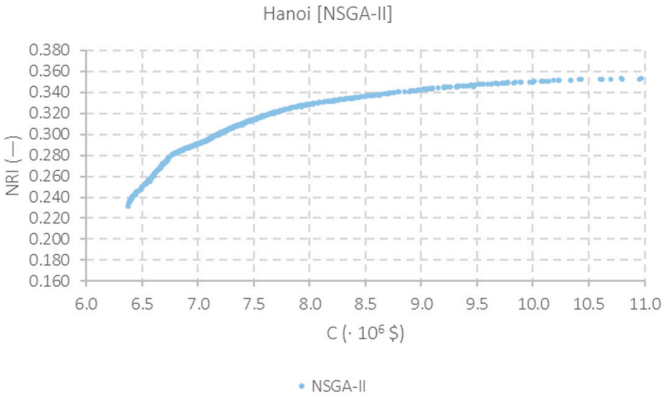
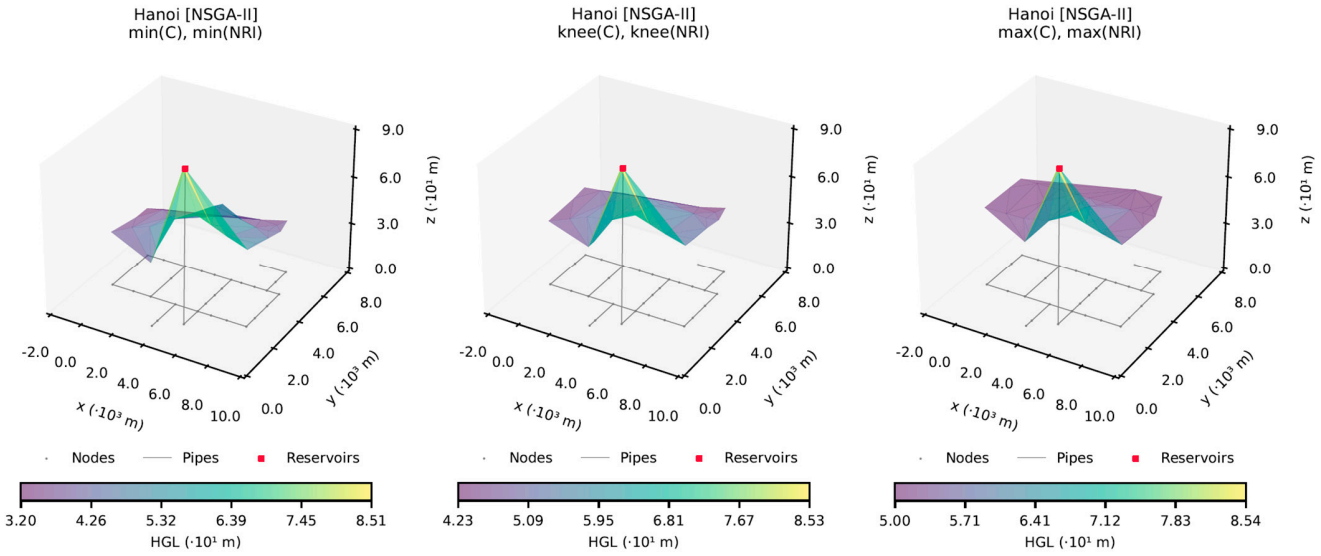
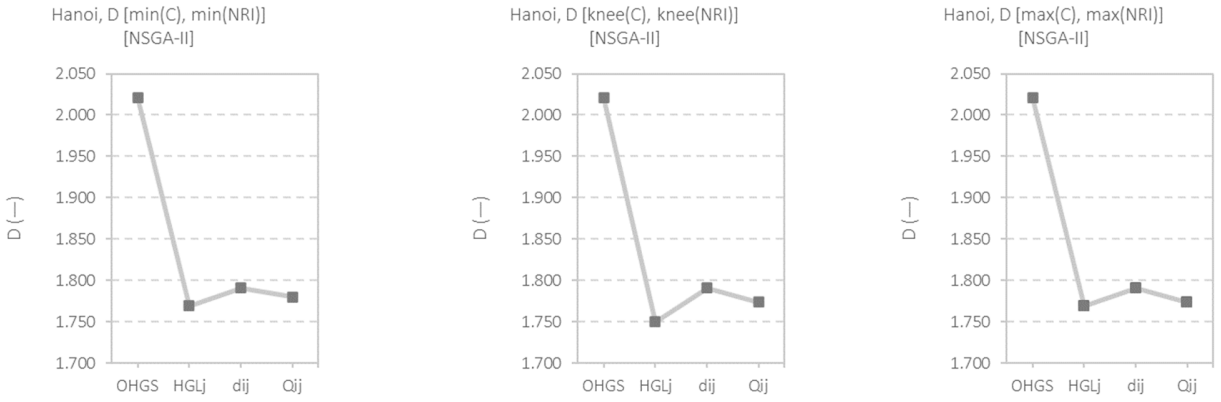


Figure S19. Hanoi, NSGA-II, Pareto Front (PF).



(a) *(b)* *(c)*

Figure S20. Hanoi, NSGA-II, hydraulic gradient surfaces (HGS): (a) [min(C), min(NRI)]; (b) [knee(C), knee(NRI)]; (c) [max(C), max(NRI)].



(a) *(b)* *(c)*

Figure S21. Hanoi, NSGA-II, fractal dimensions (D): (a) [min(C), min(NRI)]; (b) [knee(C), knee(NRI)]; (c) [max(C), max(NRI)].

Table S18. Fractal dimensions (D) of the extreme NSGA-II bi-objective designs of Hanoi.

Hanoi [min(C), min(NRI)] NSGA-II		
D, OHGS	2.021	
w_j	D	R^2
HGL_j	1.769	0.999
d_{ij}	1.791	0.999
Q_{ij}	1.780	0.999

Hanoi [knee(C), knee(NRI)] NSGA-II		
D, OHGS	2.021	
w_j	D	R^2
HGL_j	1.750	0.999
d_{ij}	1.791	0.999
Q_{ij}	1.774	0.999

Hanoi [max(C), max(NRI)] NSGA-II		
D, OHGS	2.021	
w_j	D	R^2
HGL_j	1.769	0.999
d_{ij}	1.791	0.999
Q_{ij}	1.773	0.999

Figure S22 shows the fractal dimensions (D) of the individuals of the non-dominated Pareto Front (PF) obtained through NSGA-II organized from minimum constructive cost (C) to maximum constructive cost (C). Figure S23 shows statistics of the design individuals obtained by the implementation of this methodology. Figure S24 to Figure S26 show the box whiskers plot of the fractal dimensions (D) considering the energy (HGL_j), infrastructure (d_{ij}) and flow (Q_{ij}) distribution patterns of each resulting individual. Finally, Table S19 to Table S21 show relevant statistics of the computed fractal dimensions (D) and the determination coefficients (R^2) associated to each computation.

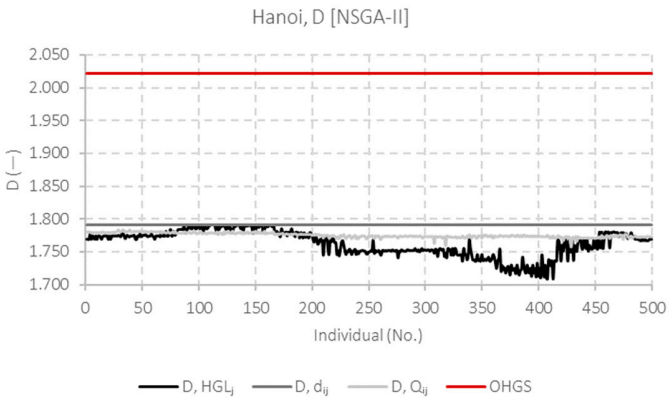
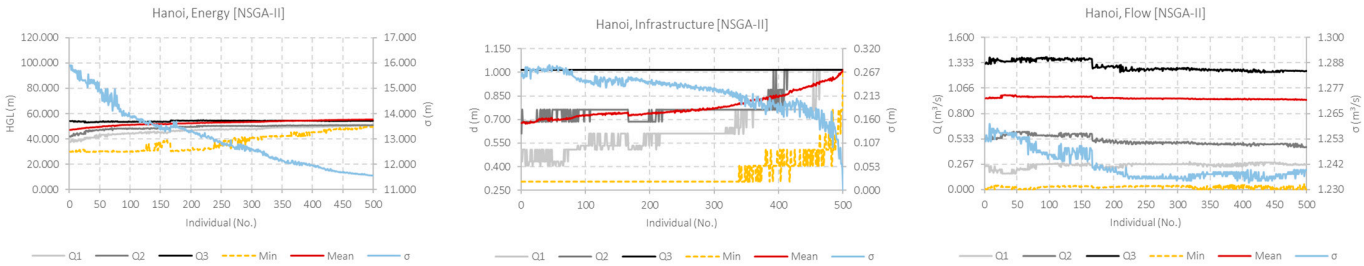


Figure S22. Hanoi, NSGA-II, fractal dimensions (D).



(a) *(b)* *(c)*

Figure S23. Hanoi, NSGA-II, statistics of the non-dominated individuals: (a) energy (HGL); (b) infrastructure (d); (c) flow (Q).

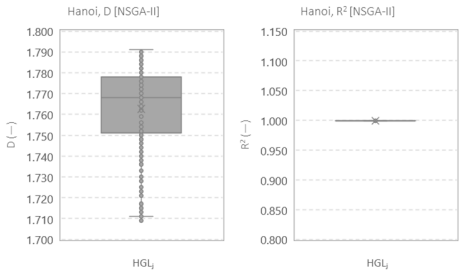


Figure S24. Hanoi, NSGA-II, box whiskers plots, $w_j = HGL_j$: (a) fractal dimensions (D); (b) determination coefficients (R^2).

Table S19. Hanoi, NSGA-II, statistics, $w_j = HGL_j$: (a) fractal dimensions (D); (b) determination coefficients (R^2).

Hanoi, NSGA-II		Hanoi, NSGA-II	
D, HGL_j		R^2, HGL_j	
Q1	1.751	Q1	0.999
Q2	1.768	Q2	0.999
Q3	1.778	Q3	0.999
σ	$1.977 \cdot 10^{-2}$	σ	$9.780 \cdot 10^{-15}$
Min	1.709	Min	0.999
Mean	1.763	Mean	0.999
Max	1.791	Max	0.999

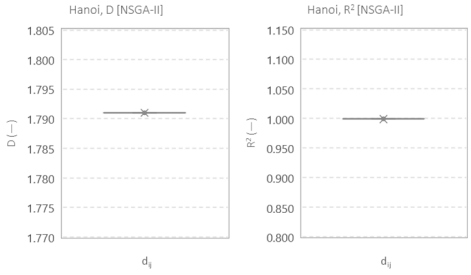


Figure S25. Hanoi, NSGA-II, box whiskers plots, $w_j = d_{ij}$: (a) fractal dimensions (D); (b) determination coefficients (R^2).

Table S20. Hanoi, NSGA-II, statistics, $w_j = d_{ij}$: (a) fractal dimensions (D); (b) determination coefficients (R^2).

Hanoi, NSGA-II		Hanoi, NSGA-II	
D, d_{ij}		R^2, d_{ij}	
Q1	1.791	Q1	0.999
Q2	1.791	Q2	0.999
Q3	1.791	Q3	0.999
σ	$2.156 \cdot 10^{-14}$	σ	$9.780 \cdot 10^{-15}$
Min	1.791	Min	0.999
Mean	1.791	Mean	0.999
Max	1.791	Max	0.999

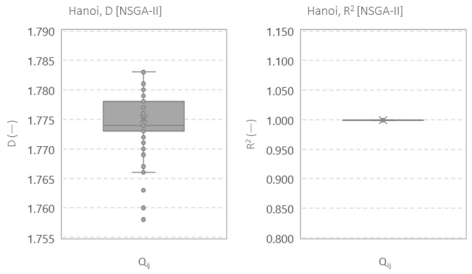


Figure S26. Hanoi, NSGA-II, box whiskers plots, $w_j = Q_{ij}$: (a) fractal dimensions (D); (b) determination coefficients (R^2).

Table S21. Hanoi, NSGA-II, statistics, $w_j = Q_{ij}$: (a) fractal dimensions (D); (b) determination coefficients (R^2).

Hanoi, OPUS/NSGA-II		Hanoi, OPUS/NSGA-II	
D, Q_{ij}		R^2, Q_{ij}	
Q1	1.773	Q1	0.999
Q2	1.774	Q2	0.999
Q3	1.778	Q3	0.999
σ	$3.363 \cdot 10^{-3}$	σ	$9.780 \cdot 10^{-15}$
Min	1.758	Min	0.999
Mean	1.775	Mean	0.999
Max	1.783	Max	0.999

3.2.1.3. OPUS/NSGA-II

Figure S27 shows the non-dominated Pareto Front (PF) of Hanoi obtained through the application of OPUS/NSGA-II [17]. Figure S28 shows the hydraulic gradient surface (HGS) of the [min(C), min(D)], [knee(C), knee(NRI)], [max(C), max(NRI)] design outcomes representing the extreme values of the energy (HGL) infrastructural (d) and flow distribution patterns of Hanoi through this design methodology. Figure S29 shows the achieved fractal dimension (D) of the extreme OPUS/NSGA-II bi-objective designs. Table S22 shows the magnitudes of the fractal dimensions (D) of the extreme OPUS/NSGA-II bi-objective designs of Hanoi.

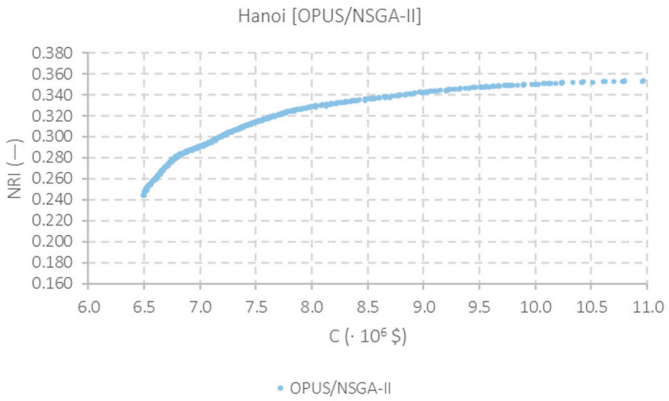


Figure S27. Hanoi, OPUS/NSGA-II, Pareto Front (PF).

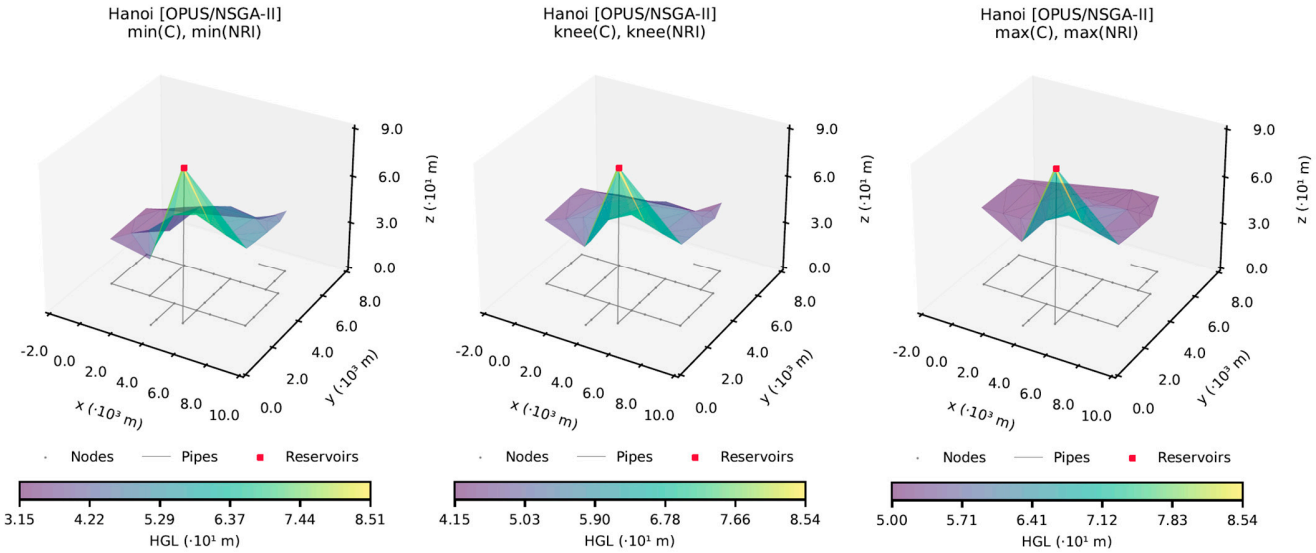


Figure S28. Hanoi, OPUS/NSGA-II, hydraulic gradient surfaces (HGS): (a) [min(C), min(NRI)]; (b) [knee(C), knee(NRI)]; (c) [max(C), max(NRI)].

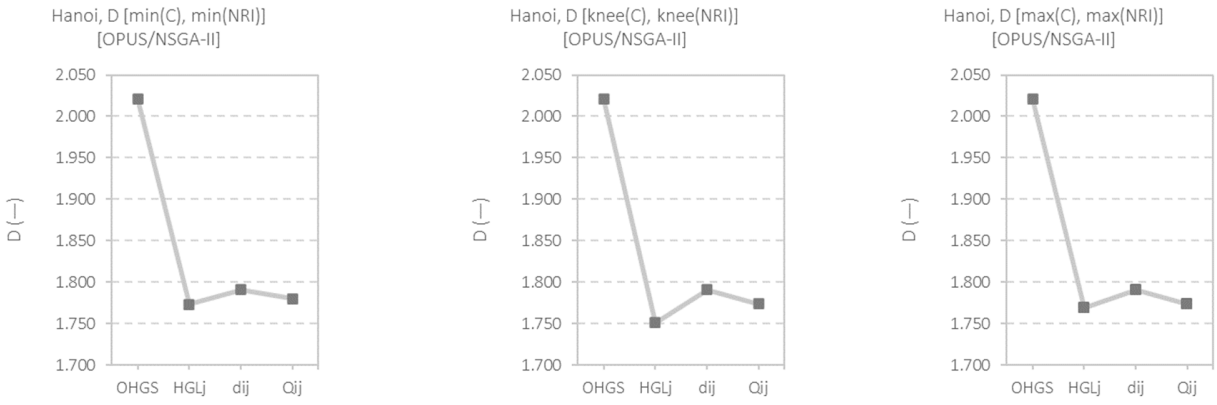


Figure S29. Hanoi, OPUS/NSGA-II, fractal dimensions (D): (a) [min(C), min(NRI)]; (b) [knee(C), knee(NRI)]; (c) [max(C), max(NRI)].

Table S22. Fractal dimensions (D) of the extreme OPUS/NSGA-II bi-objective designs of Hanoi.

Hanoi [min(C), min(NRI)] OPUS/NSGA-II		
D, OHGS	2.021	
w_j	D	R^2
HGL_j	1.773	0.999
d_{ij}	1.791	0.999
Q_{ij}	1.780	0.999

Hanoi [knee(C), knee(NRI)] OPUS/NSGA-II		
D, OHGS	2.021	
w_j	D	R^2
HGL_j	1.751	0.999
d_{ij}	1.791	0.999
Q_{ij}	1.774	0.999

Hanoi [max(C), max(NRI)] OPUS/NSGA-II		
D, OHGS	2.021	
w_j	D	R^2
HGL_j	1.769	0.999
d_{ij}	1.791	0.999
Q_{ij}	1.773	0.999

Figure S30 shows the fractal dimensions (D) of the individuals of the non-dominated Pareto Front (PF) obtained through OPUS/NSGA-II organized from minimum constructive cost (C) to maximum constructive cost (C). Figure S31 shows statistics of the design individuals obtained by the implementation of this methodology. Figure S32 to Figure S34 show the box whiskers plot of the fractal dimensions (D) considering the energy (HGL_j), infrastructure (d_{ij}) and flow (Q_{ij}) distribution patterns of each resulting individual. Finally, Table S23 to Table S25 show relevant statistics of the computed fractal dimensions (D) and the determination coefficients (R^2) associated to each computation.

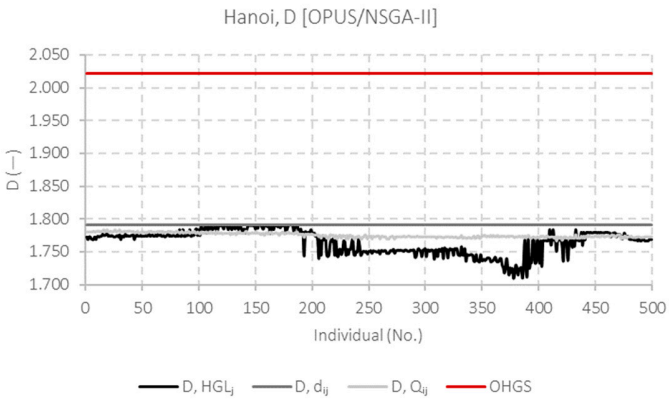
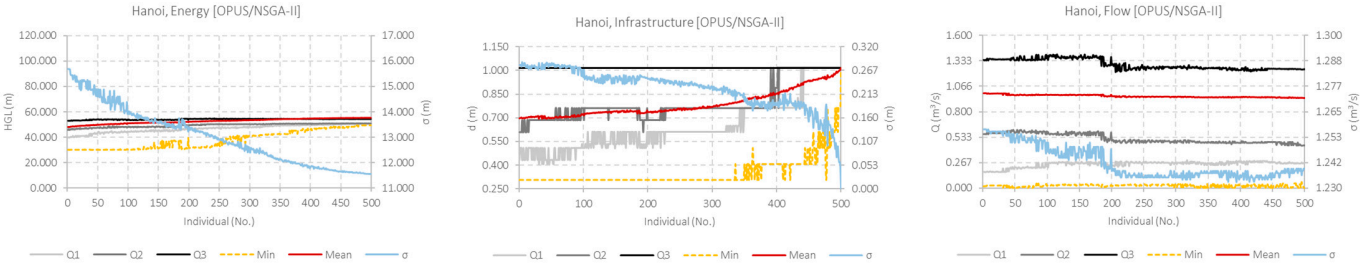


Figure S30. Hanoi, OPUS/NSGA-II, fractal dimensions (D).



(a) *(b)* *(c)*

Figure S31. Hanoi, OPUS/NSGA-II, statistics of the non-dominated individuals: (a) energy (HGL); (b) infrastructure (d); (c) flow (Q).

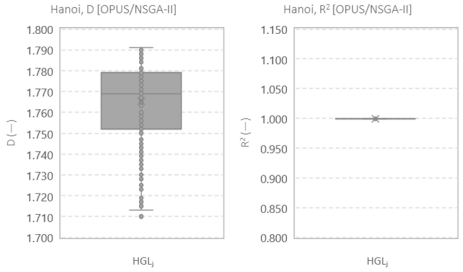


Figure S32. Hanoi, OPUS/NSGA-II, box whiskers plots, w_j = HGL_j: (a) fractal dimensions (D); (b) determination coefficients (R^2).

Table S23. Hanoi, NSGA-II, statistics, w_j = HGL_j: (a) fractal dimensions (D); (b) determination coefficients (R^2).

Hanoi, OPUS/NSGA-II		Hanoi, OPUS/NSGA-II	
D, HGL_j		R^2, HGL_j	
Q1	1.752	Q1	0.999
Q2	1.769	Q2	0.999
Q3	1.779	Q3	0.999
σ	$1.828 \cdot 10^{-2}$	σ	$9.780 \cdot 10^{-15}$
Min	1.710	Min	0.999
Mean	1.765	Mean	0.999
Max	1.791	Max	0.999

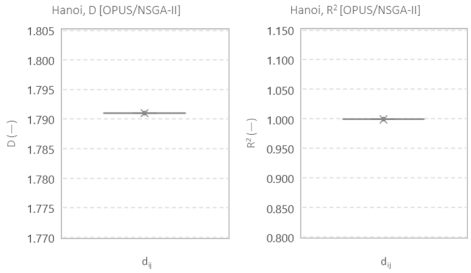


Figure S33. Hanoi, OPUS/NSGA-II, box whiskers plots, w_j = d_{ij}: (a) fractal dimensions (D); (b) determination coefficients (R^2).

Table S24. Hanoi, NSGA-II, statistics, w_j = d_{ij}: (a) fractal dimensions (D); (b) determination coefficients (R^2).

Hanoi, OPUS/NSGA-II		Hanoi, OPUS/NSGA-II	
D, d_{ij}		R^2, d_{ij}	
Q1	1.791	Q1	0.999
Q2	1.791	Q2	0.999
Q3	1.791	Q3	0.999
σ	$2.156 \cdot 10^{-14}$	σ	$9.780 \cdot 10^{-15}$
Min	1.791	Min	0.999
Mean	1.791	Mean	0.999
Max	1.791	Max	0.999

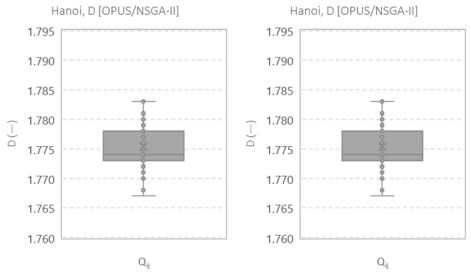


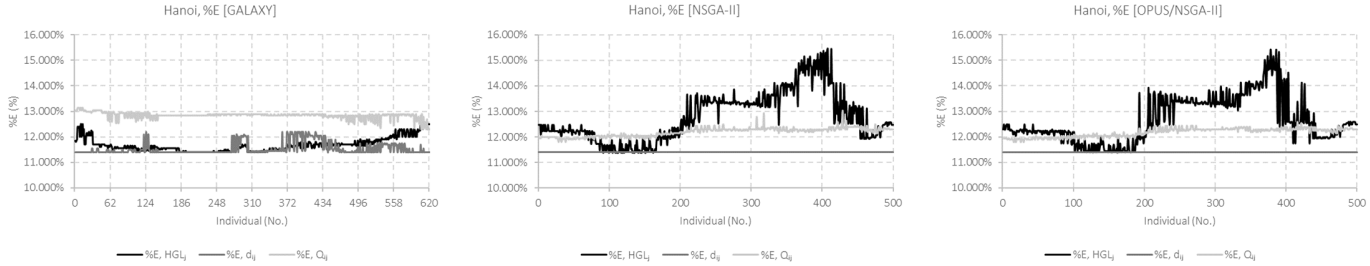
Figure S34. Hanoi, OPUS/NSGA-II, box whiskers plots, $w_j = Q_{ij}$: (a) fractal dimensions (D); (b) determination coefficients (R^2).

Table S25. Hanoi, NSGA-II, statistics, $w_j = Q_{ij}$: (a) fractal dimensions (D); (b) determination coefficients (R^2).

Hanoi, OPUS/NSGA-II		Hanoi, OPUS/NSGA-II	
D, Q_{ij}		R^2, Q_{ij}	
Q1	1.773	Q1	0.999
Q2	1.774	Q2	0.999
Q3	1.778	Q3	0.999
σ	$3.363 \cdot 10^{-3}$	σ	$9.780 \cdot 10^{-15}$
Min	1.767	Min	0.999
Mean	1.775	Mean	0.999
Max	1.783	Max	0.999

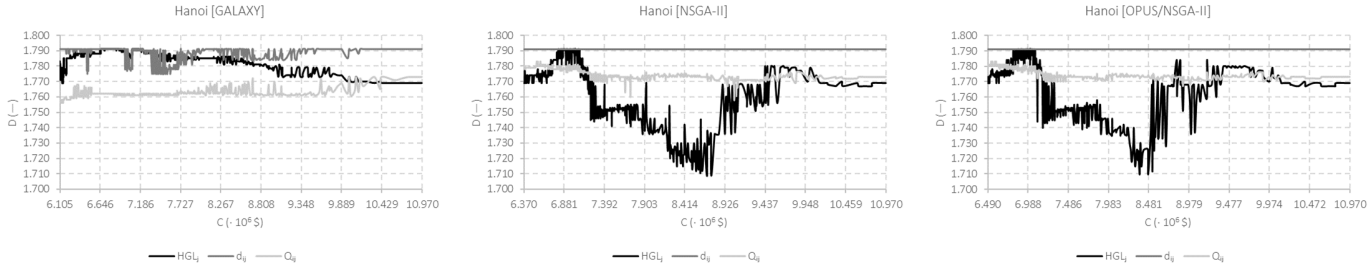
3.2.1.4. Analysis of Results

Figure S35 shows the percent error (%E) between the fractal dimension of the Optimal Hydraulic Gradient Surface (OHGS) with respect to the computed fractal dimensions (D) considering each hydraulic criterion (w_j) by case study. Figure S36 shows the relationship between the computed fractal dimensions (D) and the constructive cost (C) of each design solution by case study. Table S26 shows the reason between the fractal dimensions (D) of the minimum constructive cost (C) individual and the maximum constructive cost (C) individual by design methodology.



(a) *(b)* *(c)*

Figure S35. Percent error (%E) between the fractal dimension of the Optimal Hydraulic Gradient Surfaces (OHGS) and the computed fractal dimensions (D): Hanoi (a) GALAXY; (b) NSGA-II; (c) OPUS/NSGA-II.



(a) *(b)* *(c)*

Figure S36. Relationship between the fractal dimensions (D) and the constructive costs (C): Hanoi (a) GALAXY; (b) NSGA-II; (c) OPUS/NSGA-II,

Table S26. Reason between the fractal dimension (D) of the minimum and maximum constructive cost (C) individual: Hanoi (a) GALAXY; (b) NSGA-II; (c) OPUS/NSGA-II.

GALAXY		NSGA-II		OPUS/NSGA-II	
w_j	$D_{min(C)}/ D_{max(C)}$	w_j	$D_{min(C)}/ D_{max(C)}$	w_j	$D_{min(C)}/ D_{max(C)}$
HGL_j	0.993	HGL_j	1.000	HGL_j	0.998
d_{ij}	1.000	d_{ij}	1.000	d_{ij}	1.000
Q_{ij}	1.009	Q_{ij}	0.996	Q_{ij}	0.996

3.2.2. Balerma

Figure S37 shows the non-dominated Pareto Fronts (PF) of Balerma obtained through the application of NSGA-II (Deb et al., 2022), OPUS/NSGA-II (Páez et al., 2020) and GALAXY (Wang et al., 2017).

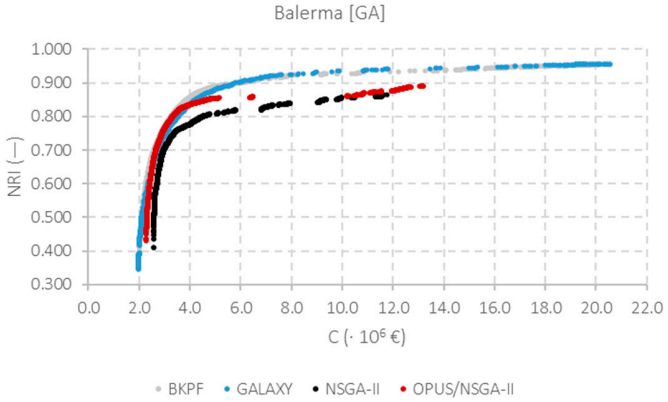


Figure S37. Balerma, genetic algorithms. Note: Note: BKPF refers to the Best-Known Pareto Front found in the literature (Wang et al., 2015).

3.2.2.1. GALAXY

Figure S38 shows the non-dominated Pareto Front (PF) of Balerma obtained through the application of GALAXY [18]. Figure S39 shows the hydraulic gradient surface (HGS) of the [min(C), min(D)], [knee(C), knee(NRI)], [max(C), max(NRI)] design outcomes representing the extreme values of the energy (HGL) infrastructural (d) and flow distribution patterns of Balerma through this design methodology. Figure S40 shows the achieved fractal dimension (D) of the extreme GALAXY bi-objective designs. Table S27 shows the magnitudes of the fractal dimensions (D) of the extreme GALAXY bi-objective designs of Balerma.

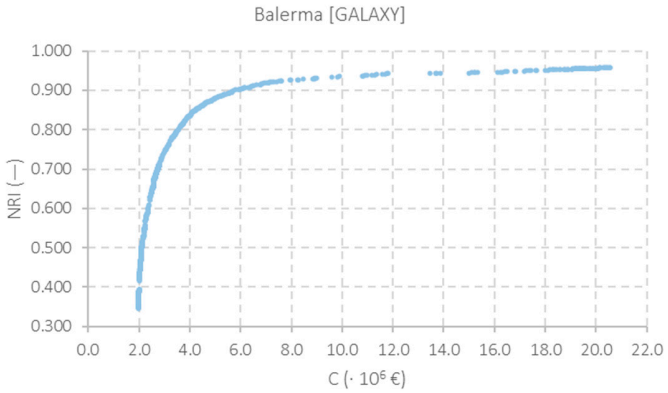
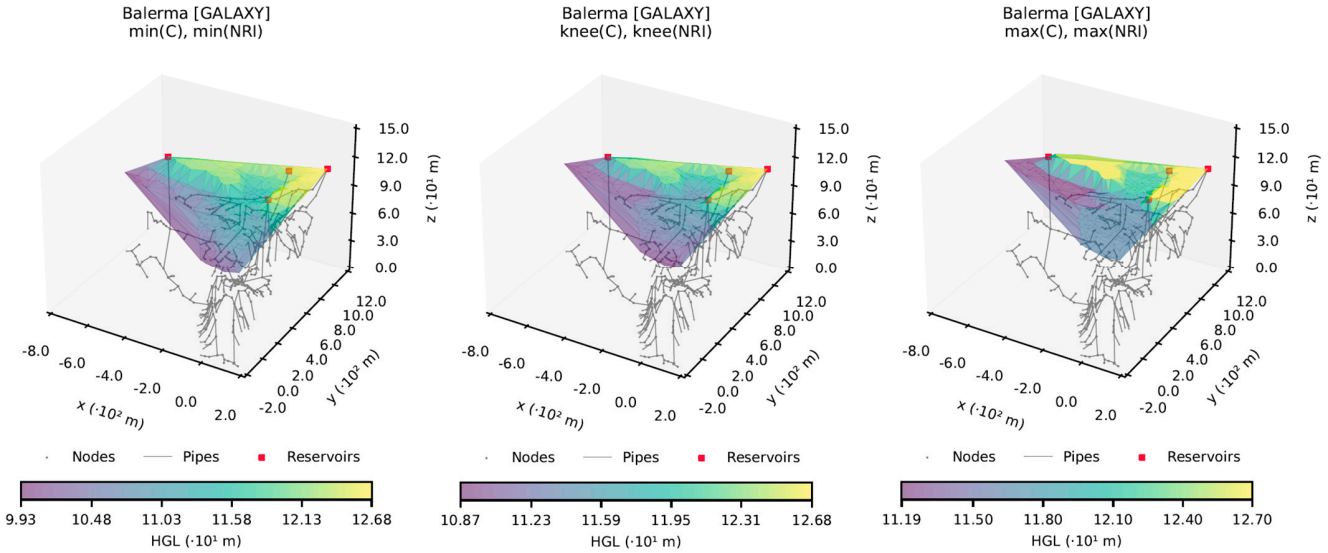
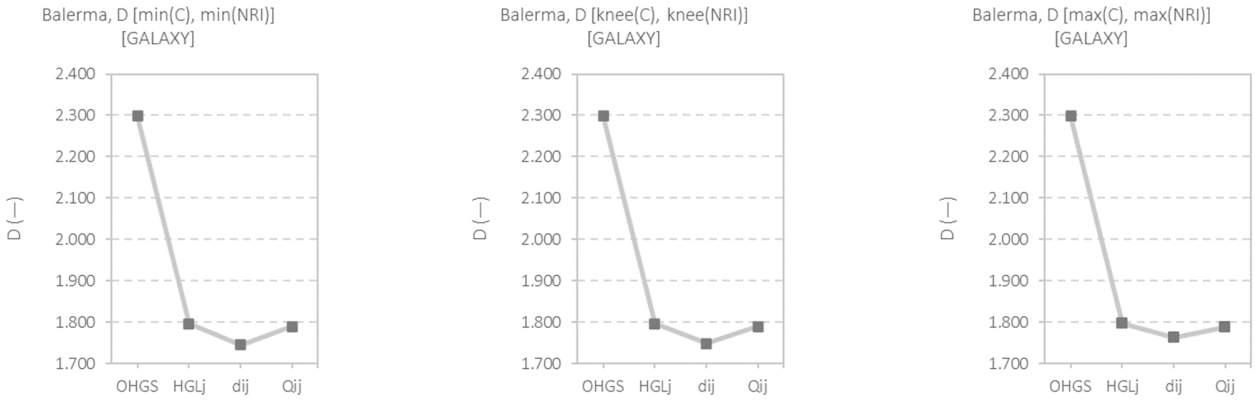


Figure S38. Balerma, GALAXY, Pareto Front (PF).



(a) *(b)* *(c)*

Figure S39. Balerma, GALAXY, hydraulic gradient surfaces (HGS): (a) [min(C), min(NRI)]; (b) [knee(C), knee(NRI)]; (c) [max(C), max(NRI)].



(a) *(b)* *(c)*

Figure S40. Balerma, GALAXY, fractal dimensions (D): (a) [min(C), min(NRI)]; (b) [knee(C), knee(NRI)]; (c) [max(C), max(NRI)].

Table S27. Fractal dimensions (D) of the extreme GALAXY bi-objective designs of Balerma.

Balerma [min(C), min(NRI)] GALAXY		
D, OHGS	2.298	
w_j	D	R^2
HGL_j	1.797	0.999
d_{ij}	1.745	1.000
Q_{ij}	1.790	0.999

Balerma [knee(C), knee(NRI)] GALAXY		
D, OHGS	2.298	
w_j	D	R^2
HGL_j	1.797	0.999
d_{ij}	1.749	1.000
Q_{ij}	1.790	0.999

Balerma [max(C), max(NRI)] GALAXY		
D, OHGS	2.298	
w_j	D	R^2
HGL_j	1.797	0.999
d_{ij}	1.790	1.000
Q_{ij}	1.789	0.999

Figure S41 shows the fractal dimensions (D) of the individuals of the non-dominated Pareto Front (PF) obtained through GALAXY organized from minimum constructive cost (C) to maximum constructive cost (C). Figure S42 shows statistics of the design individuals obtained by the implementation of this methodology. Figure S43 to Figure S45 show the box whiskers plot of the fractal dimensions (D) considering the energy (HGL_j), infrastructure (d_{ij}) and flow (Q_{ij}) distribution patterns of each resulting individual. Finally, Table S28 to Table S30 show relevant statistics of the computed fractal dimensions (D) and the determination coefficients (R^2) associated to each computation.

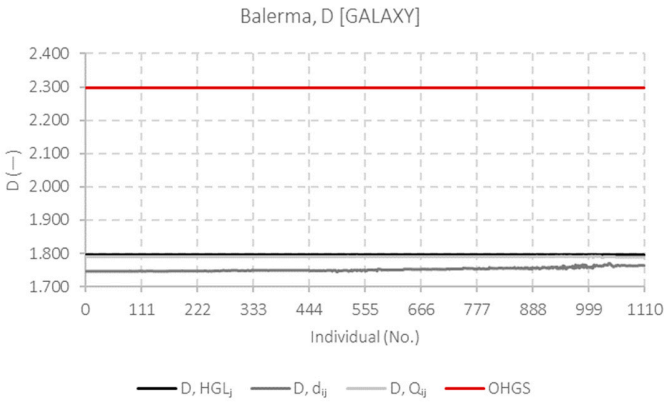
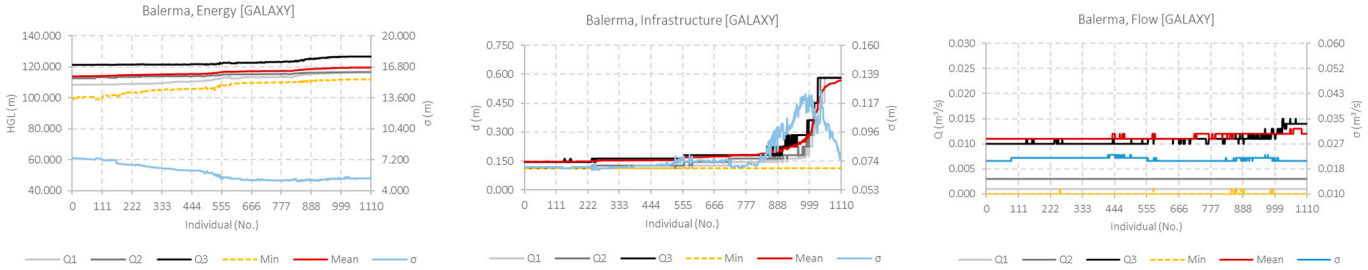


Figure S41. Balerma, GALAXY, fractal dimensions (D).



(a) *(b)* *(c)*

Figure S42. Balerma, GALAXY, statistics of the non-dominated individuals: (a) energy (HGL); (b) infrastructure (d); (c) flow (Q).

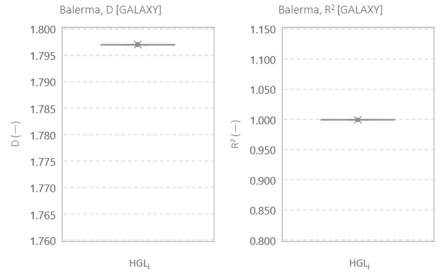


Figure S43. Balerma, GALAXY, box whiskers plots, $w_j = HGL_j$: (a) fractal dimensions (D); (b) determination coefficients (R^2).

Table S28. Balerma, GALAXY, statistics, $w_j = HGL_j$: (a) fractal dimensions (D); (b) determination coefficients (R^2).

Balerma, GALAXY		Balerma, GALAXY	
D, HGL_j		R^2, HGL_j	
Q1	1.797	Q1	0.999
Q2	1.797	Q2	0.999
Q3	1.797	Q3	0.999
σ	$2.177 \cdot 10^{-4}$	σ	$1.733 \cdot 10^{-14}$
Min	1.797	Min	0.999
Mean	1.797	Mean	0.999
Max	1.797	Max	0.999

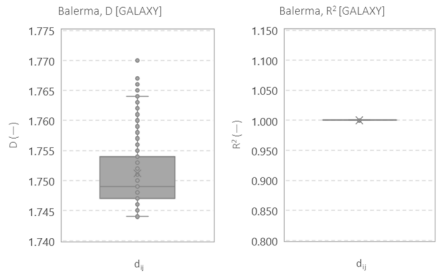


Figure S44. Balerma, GALAXY, box whiskers plots, $w_j = d_{ij}$: (a) fractal dimensions (D); (b) determination coefficients (R^2).

Table S29. Balerma, GALAXY, statistics, $w_j = d_{ij}$: (a) fractal dimensions (D); (b) determination coefficients (R^2).

Balerma, GALAXY		Balerma, GALAXY	
D, d_{ij}		R^2, d_{ij}	
Q1	1.747	Q1	1.000
Q2	1.749	Q2	1.000
Q3	1.754	Q3	1.000
σ	$5.769 \cdot 10^{-3}$	σ	$2.690 \cdot 10^{-4}$
Min	1.744	Min	0.999
Mean	1.751	Mean	1.000
Max	1.770	Max	1.000

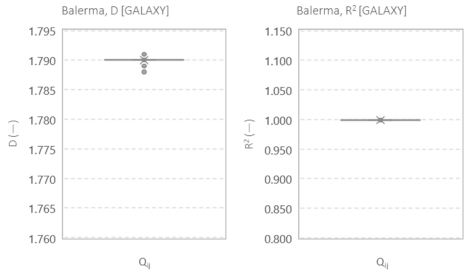


Figure S45. Balerma, GALAXY, box whiskers plots, $w_j = Q_{ij}$: (a) fractal dimensions (D); (b) determination coefficients (R^2).

Table S30. Balerma, GALAXY, statistics, $w_j = Q_{ij}$: (a) fractal dimensions (D); (b) determination coefficients (R^2).

Balerma, GALAXY		Balerma, GALAXY	
D, Q_{ij}		R^2, Q_{ij}	
Q1	1.790	Q1	0.999
Q2	1.790	Q2	0.999
Q3	1.790	Q3	0.999
σ	$3.126 \cdot 10^{-4}$	σ	$1.733 \cdot 10^{-14}$
Min	1.788	Min	0.999
Mean	1.790	Mean	0.999
Max	1.791	Max	0.999

3.2.2.2. NSGA-II

Figure S46 shows the non-dominated Pareto Front (PF) of Balerma obtained through the application of NSGA-II [17]. Figure S47 shows the hydraulic gradient surface (HGS) of the [min(C), min(D)], [knee(C), knee(NRI)], [max(C), max(NRI)] design outcomes representing the extreme values of the energy (HGL) infrastructural (d) and flow distribution patterns of Balerma through this design methodology. Figure S48 shows the achieved fractal dimension (D) of the extreme NSGA-II bi-objective designs. Table S31 shows the magnitudes of the fractal dimensions (D) of the extreme NSGA-II bi-objective designs of Balerma.

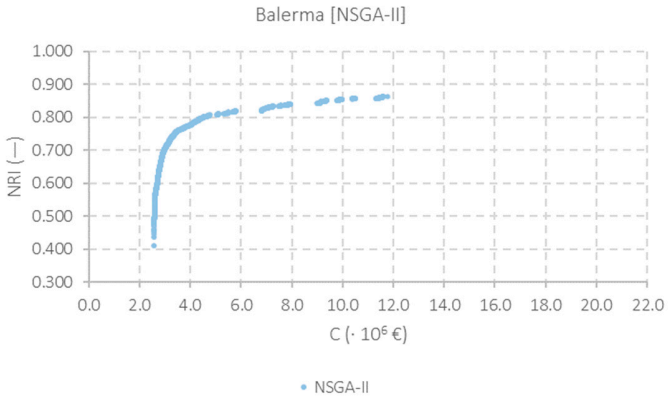
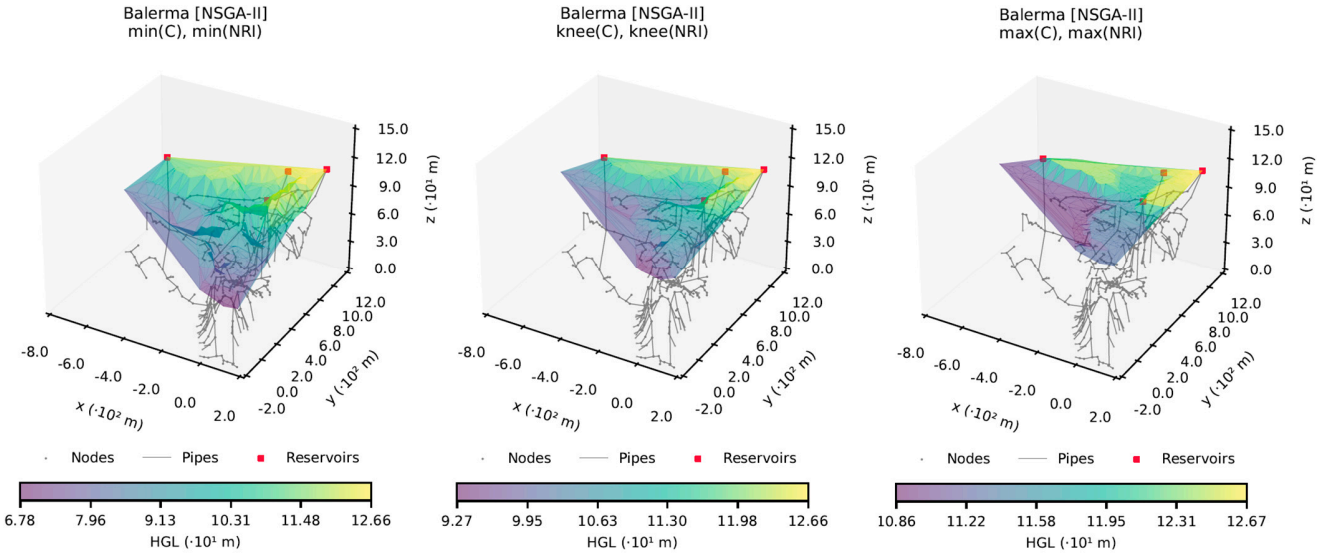
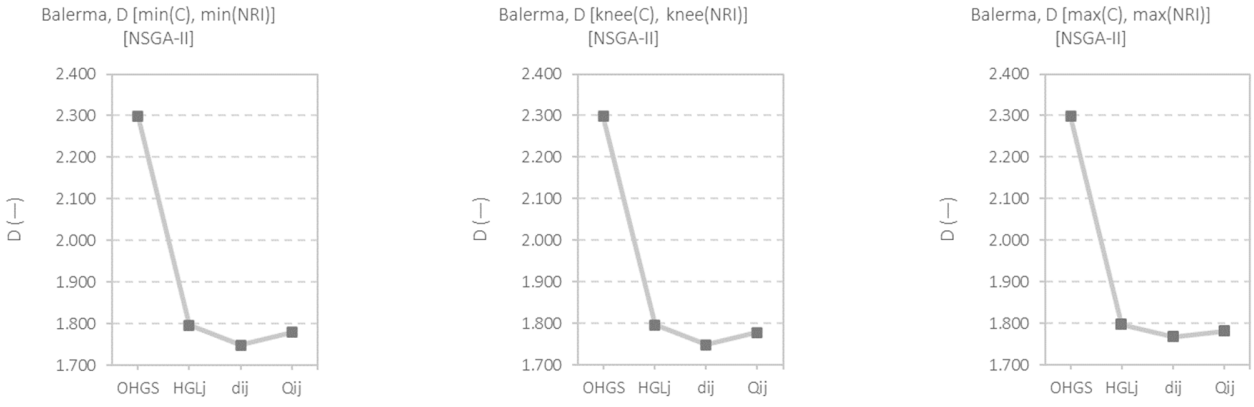


Figure S46. Balerma, NSGA-II, Pareto Front (PF).



(a) *(b)* *(c)*

Figure S47. Balerma, NSGA-II, hydraulic gradient surfaces (HGS): (a) [min(C), min(NRI)]; (b) [knee(C), knee(NRI)]; (c) [max(C), max(NRI)].



(a) *(b)* *(c)*

Figure S48. Balerma, NSGA-II, fractal dimensions (D): (a) [min(C), min(NRI)]; (b) [knee(C), knee(NRI)]; (c) [max(C), max(NRI)].

Table S31. Fractal dimensions (D) of the extreme NSGA-II bi-objective designs of Balerma.

Balerma [min(C), min(NRI)] NSGA-II		
D, OHGS	2.298	
w_j	D	R^2
HGL_j	1.797	0.999
d_{ij}	1.749	1.000
Q_{ij}	1.779	1.000

Balerma [knee(C), knee(NRI)] NSGA-II		
D, OHGS	2.298	
w_j	D	R^2
HGL_j	1.797	0.999
d_{ij}	1.749	1.000
Q_{ij}	1.778	1.000

Balerma [max(C), max(NRI)] NSGA-II		
D, OHGS	2.298	
w_j	D	R^2
HGL_j	1.797	0.999
d_{ij}	1.768	1.000
Q_{ij}	1.780	0.999

Figure S49 shows the fractal dimensions (D) of the individuals of the non-dominated Pareto Front (PF) obtained through NSGA-II organized from minimum constructive cost (C) to maximum constructive cost (C). Figure S50 shows statistics of the design individuals obtained by the implementation of this methodology. Figure S51 to Figure S53 show the box whiskers plot of the fractal dimensions (D) considering the energy (HGL_j), infrastructure (d_{ij}) and flow (Q_{ij}) distribution patterns of each resulting individual. Finally, Table S32 to Table S34 show relevant statistics of the computed fractal dimensions (D) and the determination coefficients (R^2) associated to each computation.

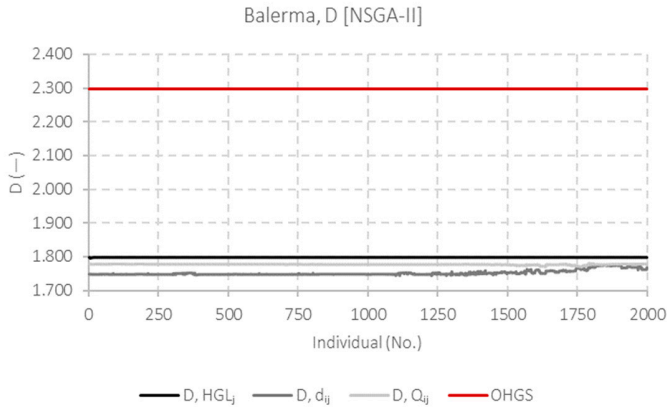
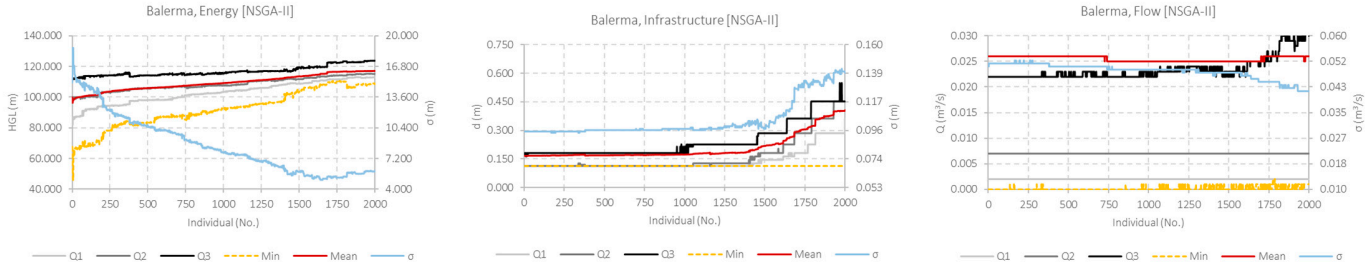


Figure S49. Balerma, NSGA-II, fractal dimensions (D).



(a) *(b)* *(c)*

Figure S50. Balerma, NSGA-II, statistics of the non-dominated individuals: (a) energy (HGL); (b) infrastructure (d); (c) flow (Q).

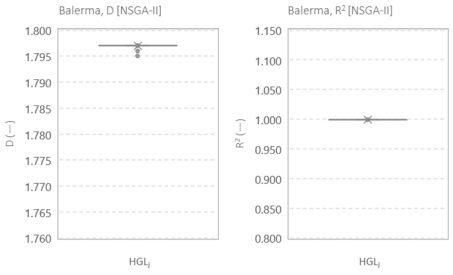


Figure S51. Balerma, NSGA-II, box whiskers plots, $w_j = HGL_j$: (a) fractal dimensions (D); (b) determination coefficients (R^2).

Table S32. Balerma, NSGA-II, statistics, $w_j = HGL_j$: (a) fractal dimensions (D); (b) determination coefficients (R^2).

Balerma, NSGA-II	
D, HGL_j	
Q1	1.797
Q2	1.797
Q3	1.797
σ	$1.070 \cdot 10^{-4}$
Min	1.795
Mean	1.797
Max	1.797

Balerma, NSGA-II	
R^2, HGL_j	
Q1	0.999
Q2	0.999
Q3	0.999
σ	$2.010 \cdot 10^{-14}$
Min	0.999
Mean	0.999
Max	0.999

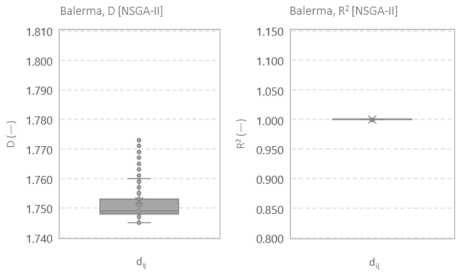


Figure S52. Balerma, NSGA-II, box whiskers plots, $w_j = d_{ij}$: (a) fractal dimensions (D); (b) determination coefficients (R^2).

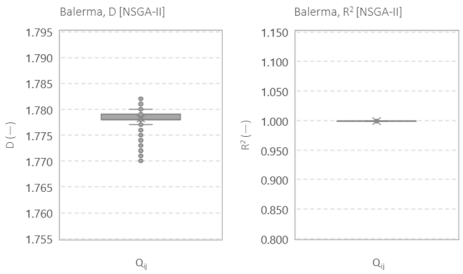


Figure S53. Balerma, NSGA-II, box whiskers plots, $w_j = Q_{ij}$: (a) fractal dimensions (D); (b) determination coefficients (R^2).

Table S33. Balerma, NSGA-II, statistics, $w_j = d_{ij}$: (a) fractal dimensions (D); (b) determination coefficients (R^2).

Balerma, NSGA-II		Balerma, NSGA-II	
D, d_{ij}		R^2, d_{ij}	
Q1	1.748	Q1	1.000
Q2	1.749	Q2	1.000
Q3	1.753	Q3	1.000
σ	$7.048 \cdot 10^{-3}$	σ	$3.672 \cdot 10^{-4}$
Min	1.745	Min	0.999
Mean	1.752	Mean	1.000
Max	1.774	Max	1.000

Table S34. Balerma, NSGA-II, statistics, $w_j = Q_{ij}$: (a) fractal dimensions (D); (b) determination coefficients (R^2).

Balerma, NSGA-II		Balerma, NSGA-II	
D, Q_{ij}		R^2, Q_{ij}	
Q1	1.778	Q1	1.000
Q2	1.778	Q2	1.000
Q3	1.789	Q3	1.000
σ	$1.463 \cdot 10^{-3}$	σ	$2.933 \cdot 10^{-4}$
Min	1.770	Min	0.999
Mean	1.778	Mean	1.000
Max	1.782	Max	1.000

3.2.2.3. OPUS/NSGA-II

Figure S54 shows the non-dominated Pareto Front (PF) of Balerma obtained through the application of OPUS/NSGA-II [17]. Figure S55 shows the hydraulic gradient surface (HGS) of the [min(C), min(D)], [knee(C), knee(NRI)], [max(C), max(NRI)] design outcomes representing the extreme values of the energy (HGL) infrastructural (d) and flow distribution patterns of Balerma through this design methodology. Figure S56 shows the achieved fractal dimension (D) of the extreme OPUS/NSGA-II bi-objective designs. Table S35 shows the magnitudes of the fractal dimensions (D) of the extreme OPUS/NSGA-II bi-objective designs of Balerma.

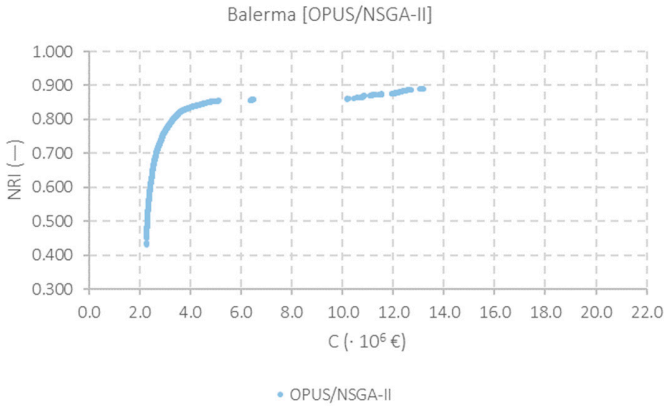
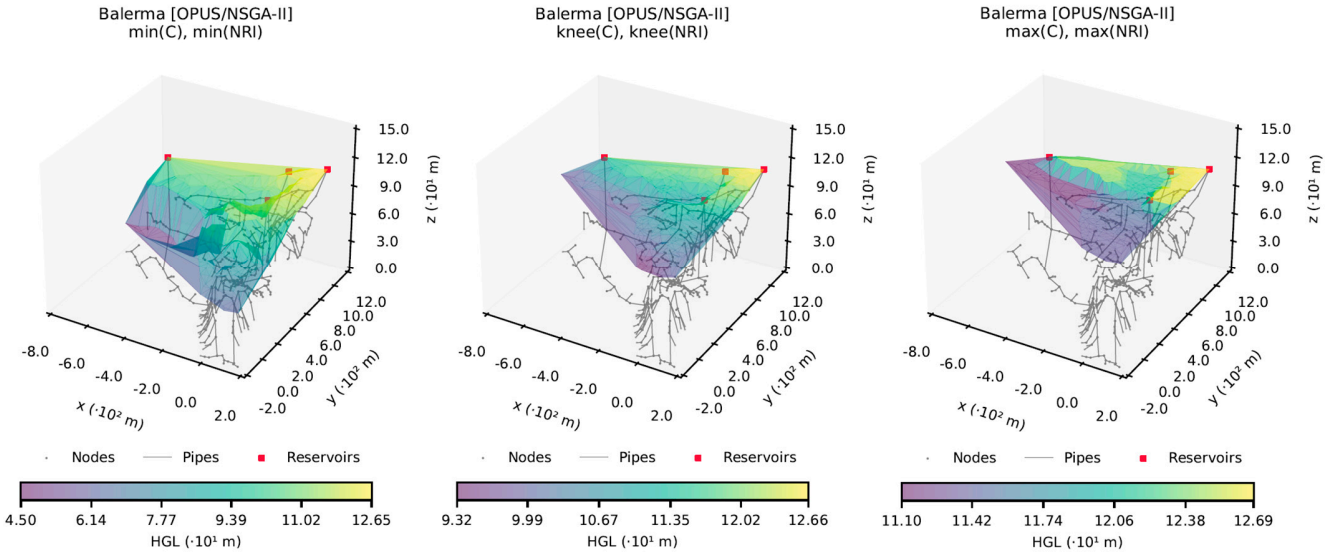
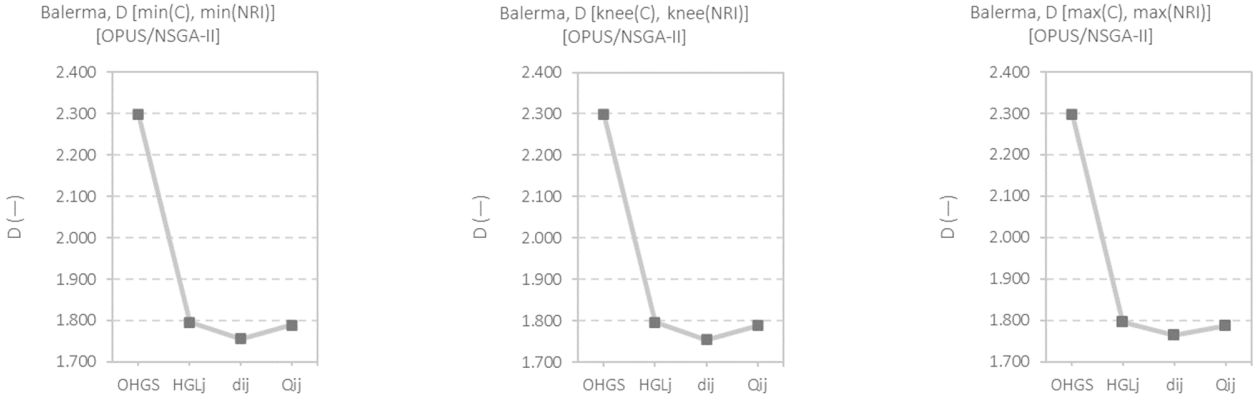


Figure S54. Balerma, OPUS/NSGA-II, Pareto Front (PF).



(a) *(b)* *(c)*

Figure S55. Balerma, OPUS/NSGA-II, hydraulic gradient surfaces (HGS): (a) [min(C), min(NRI)]; (b) [knee(C), knee(NRI)]; (c) [max(C), max(NRI)].



(a) *(b)* *(c)*

Figure S56. Balerma, OPUS/NSGA-II, fractal dimensions (D): (a) [min(C), min(NRI)]; (b) [knee(C), knee(NRI)]; (c) [max(C), max(NRI)].

Table S35. Fractal dimensions (D) of the extreme OPUS/NSGA-II bi-objective designs of Balerma.

Balerma [min(C), min(NRI)] OPUS/NSGA-II			Balerma [knee(C), knee(NRI)] OPUS/NSGA-II			Balerma [max(C), max(NRI)] OPUS/NSGA-II		
D, OHGS	2.298		D, OHGS	2.298		D, OHGS	2.298	
w_j	D	R^2	w_j	D	R^2	w_j	D	R^2
HGL_j	1.796	1.000	HGL_j	1.797	1.000	HGL_j	1.797	0.999
d_{ij}	1.756	0.999	d_{ij}	1.754	0.999	d_{ij}	1.763	0.999
Q_{ij}	1.789	0.999	Q_{ij}	1.789	0.999	Q_{ij}	1.787	0.999

Figure S57 shows the fractal dimensions (D) of the individuals of the non-dominated Pareto Front (PF) obtained through OPUS/NSGA-II organized from minimum constructive cost (C) to maximum constructive cost (C). Figure S58 shows statistics of the design individuals obtained by the implementation of this methodology. Figure S59 to Figure S61 show the box whiskers plot of the fractal dimensions (D) considering the energy (HGL_j), infrastructure (d_{ij}) and flow (Q_{ij}) distribution patterns of each resulting individual. Finally, Table S36 to Table S38 show relevant statistics of the computed fractal dimensions (D) and the determination coefficients (R^2) associated to each computation.

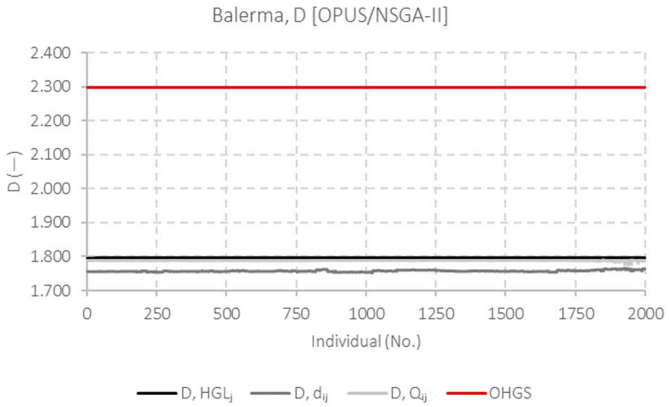
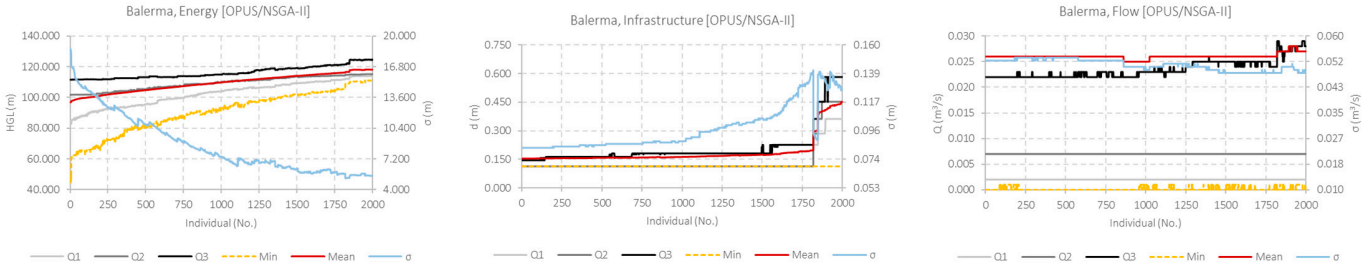


Figure S57. Balerma, OPUS/NSGA-II, fractal dimensions (D).



(a) *(b)* *(c)*

Figure S58. Balerma, OPUS/NSGA-II, statistics of the non-dominated individuals: (a) energy (HGL); (b) infrastructure (d); (c) flow (Q).

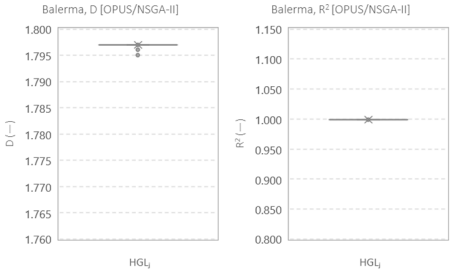


Figure S59. Balerma, OPUS/NSGA-II, box whiskers plots, w_j = HGL_j: (a) fractal dimensions (D); (b) determination coefficients (R^2).

Table S36. Balerma, OPUS/NSGA-II, statistics, w_j = HGL_j: (a) fractal dimensions (D); (b) determination coefficients (R^2).

Balerma, OPUS/NSGA-II		Balerma, OPUS/NSGA-II	
D, HGL_j		R^2, HGL_j	
Q1	1.797	Q1	0.999
Q2	1.797	Q2	0.999
Q3	1.797	Q3	0.999
σ	$1.237 \cdot 10^{-4}$	σ	$2.010 \cdot 10^{-14}$
Min	1.795	Min	0.999
Mean	1.797	Mean	0.999
Max	1.797	Max	0.999

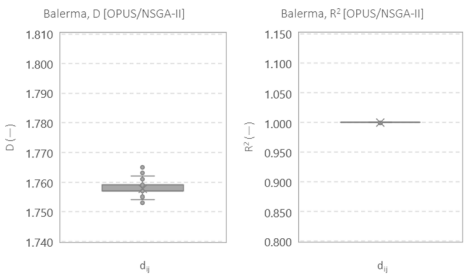


Figure S60. Balerma, OPUS/NSGA-II, box whiskers plots, w_j = d_{ij}: (a) fractal dimensions (D); (b) determination coefficients (R^2).

Table S37. Balerma, OPUS/NSGA-II, statistics, w_j = d_{ij}: (a) fractal dimensions (D); (b) determination coefficients (R^2).

Balerma, OPUS/NSGA-II		Balerma, OPUS/NSGA-II	
D, d_{ij}		R^2, d_{ij}	
Q1	1.757	Q1	1.000
Q2	1.757	Q2	1.000
Q3	1.759	Q3	1.000
σ	$2.059 \cdot 10^{-3}$	σ	$3.185 \cdot 10^{-4}$
Min	1.753	Min	0.999
Mean	1.758	Mean	1.000
Max	1.765	Max	1.000

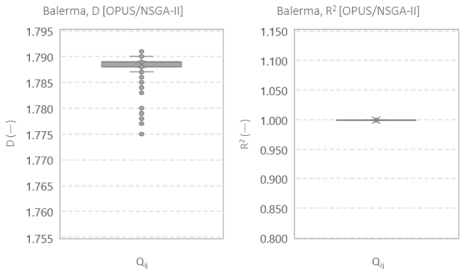


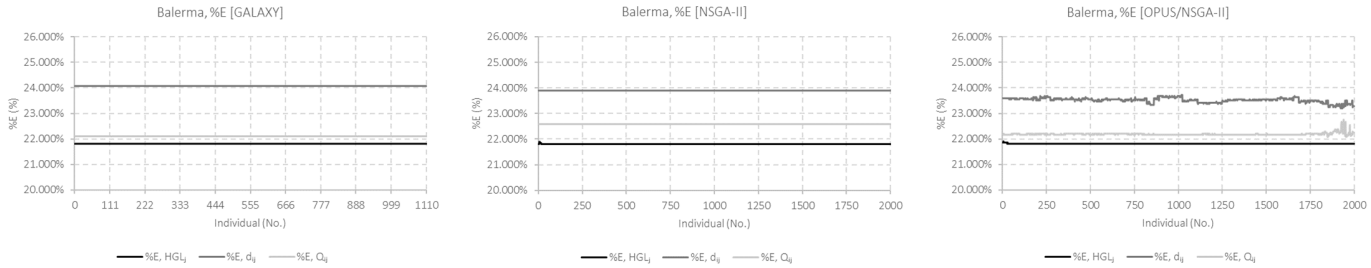
Figure S61. Balerma, OPUS/NSGA-II, box whiskers plots, $w_j = Q_{ij}$: (a) fractal dimensions (D); (b) determination coefficients (R^2).

Table S38. Balerma, OPUS/NSGA-II, statistics, $w_j = Q_{ij}$: (a) fractal dimensions (D); (b) determination coefficients (R^2).

Balerma, OPUS/NSGA-II		Balerma, OPUS/NSGA-II	
D, Q_{ij}		R^2, Q_{ij}	
Q1	1.788	Q1	0.999
Q2	1.789	Q2	0.999
Q3	1.789	Q3	0.999
σ	$1.055 \cdot 10^{-3}$	σ	$3.161 \cdot 10^{-5}$
Min	1.775	Min	0.999
Mean	1.789	Mean	0.999
Max	1.793	Max	1.000

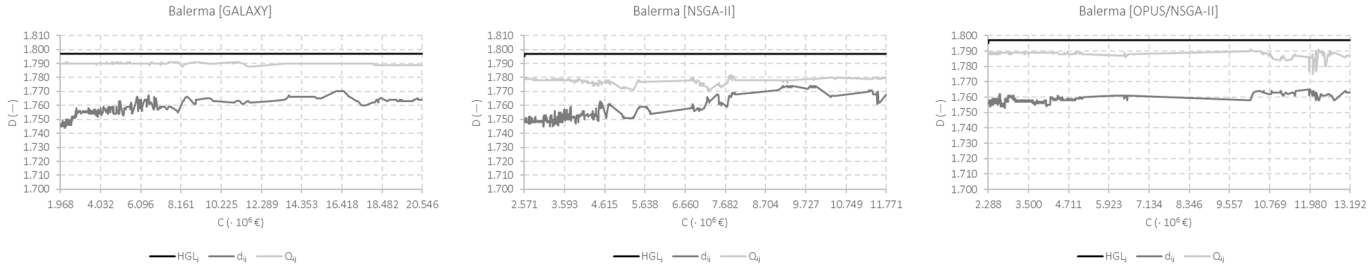
3.2.2.4. Analysis of Results

Figure S62 shows the percent error (%E) between the fractal dimension of the Optimal Hydraulic Gradient Surface (OHGS) with respect to the computed fractal dimensions (D) considering each hydraulic criterion (w_j) by case study. Figure S63 shows the relationship between the computed fractal dimensions (D) and the constructive cost (C) of each design solution by case study. Table S39 shows the reason between the fractal dimensions (D) of the minimum constructive cost (C) individual and the maximum constructive cost (C) individual by design methodology.



(a) *(b)* *(c)*

Figure S62. Percent error (%E) between the fractal dimension of the Optimal Hydraulic Gradient Surfaces (OHGS) and the computed fractal dimensions (D): Balerma (a) GALAXY; (b) NSGA-II; (c) OPUS/NSGA-II.



(a) *(b)* *(c)*

Figure S63. Relationship between the fractal dimensions (D) and the constructive costs (C): Balerma (a) GALAXY; (b) NSGA-II; (c) OPUS/NSGA-II,

Table S39. Reason between the fractal dimension (D) of the minimum and maximum constructive cost (C) individual: Balerma (a) GALAXY; (b) NSGA-II; (c) OPUS/NSGA-II.

Balerma					
GALAXY		NSGA-II		OPUS/NSGA-II	
w_j	$D_{min(C)}/D_{max(C)}$	w_j	$D_{min(C)}/D_{max(C)}$	w_j	$D_{min(C)}/D_{max(C)}$
HGL_j	1.001	HGL_j	1.000	HGL_j	1.000
d_{ij}	1.004	d_{ij}	1.011	d_{ij}	1.011
Q_{ij}	0.999	Q_{ij}	1.001	Q_{ij}	0.999

3.2.3. Modena

Figure S64 shows the non-dominated Pareto Fronts (PF) of Modena obtained through the application of NSGA-II (Deb et al., 2022), OPUS/NSGA-II (Páez et al., 2020) and GALAXY (Wang et al., 2017).

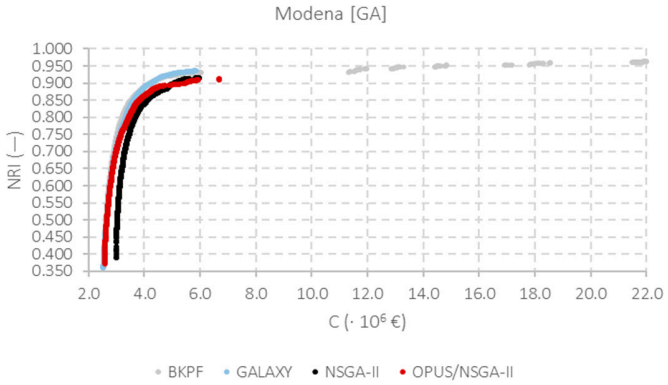


Figure S64. Modena, genetic algorithms. Note: Note: BKPF refers to the Best-Known Pareto Front found in the literature (Wang et al., 2017).

3.2.3.1. GALAXY

Figure S65 shows the non-dominated Pareto Front (PF) of Modena obtained through the application of GALAXY [18]. Figure S66 shows the hydraulic gradient surface (HGS) of the [min(C), min(D)], [knee(C), knee(NRI)], [max(C), max(NRI)] design outcomes representing the extreme values of the energy (HGL) infrastructural (d) and flow distribution patterns of Modena through this design methodology. Figure S67 shows the achieved fractal dimension (D) of the extreme GALAXY bi-objective designs. Table S40 shows the magnitudes of the fractal dimensions (D) of the extreme GALAXY bi-objective designs of Modena.

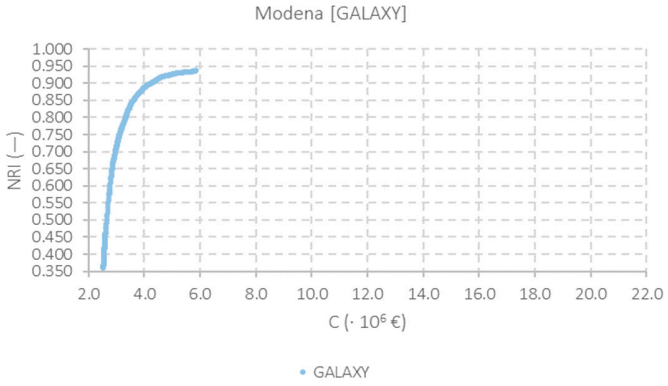
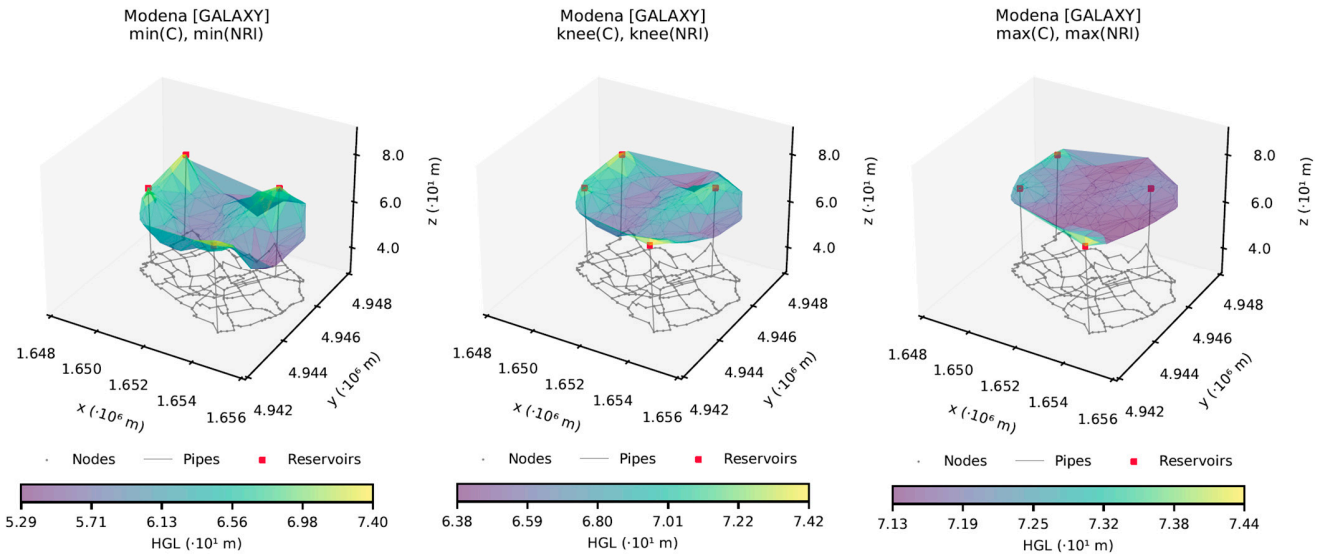
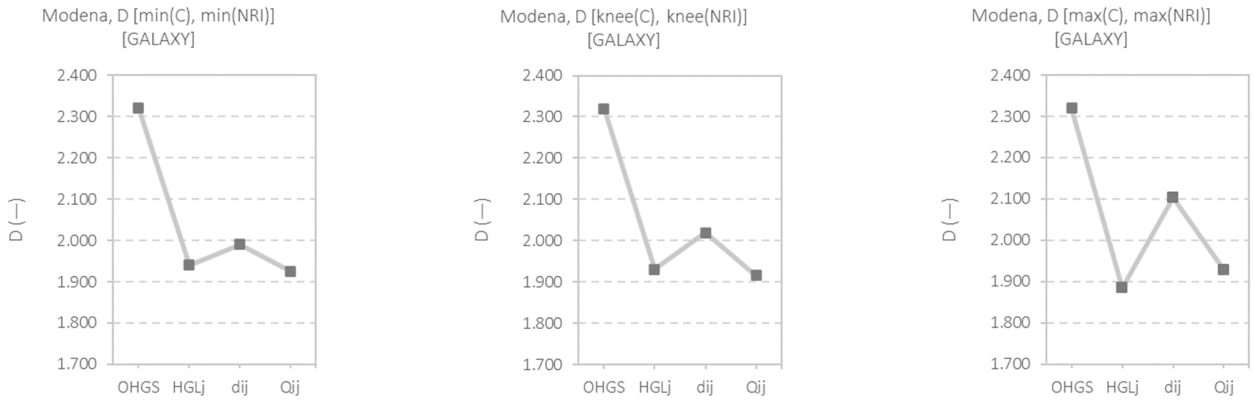


Figure S65. Modena, GALAXY, Pareto Front (PF).



(a) *(b)* *(c)*

Figure S66. Modena, GALAXY, hydraulic gradient surfaces (HGS): (a) [min(C), min(NRI)]; (b) [knee(C), knee(NRI)]; (c) [max(C), max(NRI)].



(a) *(b)* *(c)*

Figure S67. Modena, GALAXY, fractal dimensions (D): (a) [min(C), min(NRI)]; (b) [knee(C), knee(NRI)]; (c) [max(C), max(NRI)].

Table S40. Fractal dimensions (D) of the extreme GALAXY bi-objective designs of Modena.

Modena [min(C), min(NRI)] GALAXY		
D, OHGS	2.320	
w_j	D	R^2
HGL_j	1.940	0.997
d_{ij}	1.991	0.997
Q_{ij}	1.926	0.998

Modena [knee(C), knee(NRI)] GALAXY		
D, OHGS	2.320	
w_j	D	R^2
HGL_j	1.931	0.999
d_{ij}	2.019	0.997
Q_{ij}	1.916	0.998

Modena [max(C), max(NRI)] GALAXY		
D, OHGS	2.320	
w_j	D	R^2
HGL_j	1.884	1.000
d_{ij}	2.102	0.997
Q_{ij}	1.927	0.998

Figure S68 shows the fractal dimensions (D) of the individuals of the non-dominated Pareto Front (PF) obtained through GALAXY organized from minimum constructive cost (C) to maximum constructive cost (C). Figure S69 shows statistics of the design individuals obtained by the implementation of this methodology. Figure S70 to Figure S72 show the box whiskers plot of the fractal dimensions (D) considering the energy (HGL_j), infrastructure (d_{ij}) and flow (Q_{ij}) distribution patterns of each resulting individual. Finally, Table S41 to Table S43 show relevant statistics of the computed fractal dimensions (D) and the determination coefficients (R^2) associated to each computation.

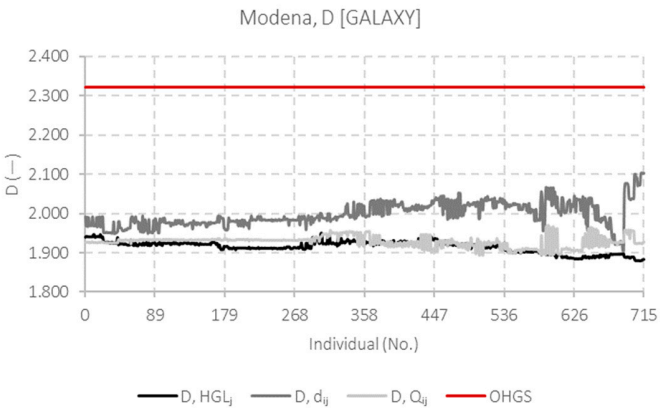
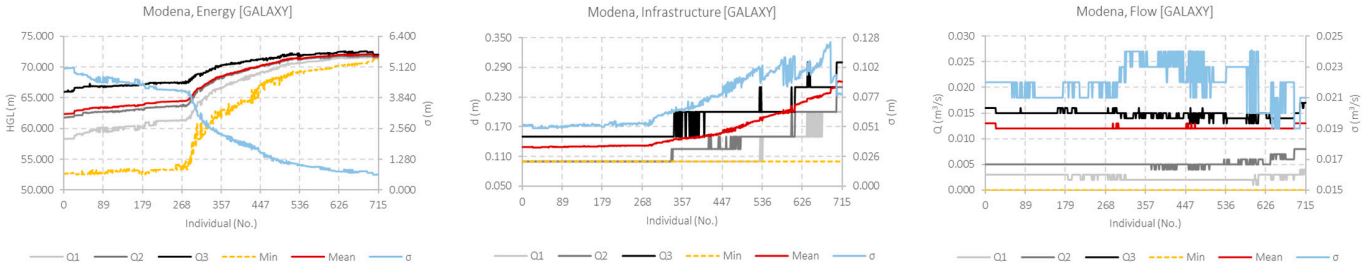


Figure S68. Modena, GALAXY, fractal dimensions (D).



(a) *(b)* *(c)*

Figure S69. Modena, GALAXY, statistics of the non-dominated individuals: (a) energy (HGL); (b) infrastructure (d); (c) flow (Q).

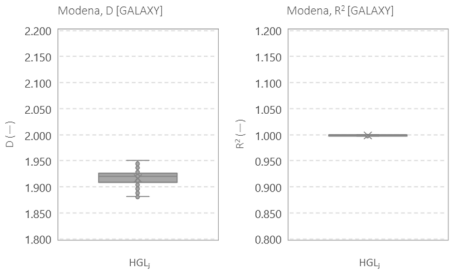


Figure S70. Modena, GALAXY, box whiskers plots, w_j = HGL$_j$: (a) fractal dimensions (D); (b) determination coefficients (R^2).

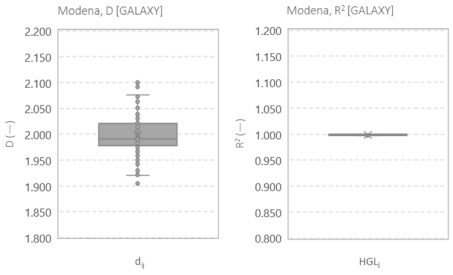


Figure S71. Modena, GALAXY, box whiskers plots, $w_j = d_{ij}$: (a) fractal dimensions (D); (b) determination coefficients (R^2).

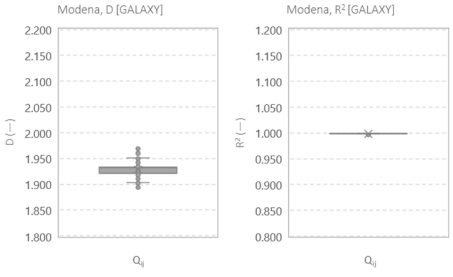


Figure S72. Modena, GALAXY, box whiskers plots, $w_j = Q_{ij}$: (a) fractal dimensions (D); (b) determination coefficients (R^2).

Table S41. Modena, GALAXY, statistics, w_j = HGL$_j$: (a) fractal dimensions (D); (b) determination coefficients (R^2).

Modena, GALAXY		Modena, GALAXY	
D, HGL$_j$		R^2, HGL$_j$	
Q1	1.908	Q1	0.997
Q2	1.920	Q2	0.999
Q3	1.926	Q3	1.000
σ	$1.471 \cdot 10^{-2}$	σ	$1.247 \cdot 10^{-3}$
Min	1.880	Min	0.997
Mean	1.916	Mean	0.999
Max	1.950	Max	1.000

Table S42. Modena, GALAXY, statistics, $w_j = d_{ij}$: (a) fractal dimensions (D); (b) determination coefficients (R^2).

Modena, GALAXY		Modena, GALAXY	
D, d$_{ij}$		R^2, d$_{ij}$	
Q1	1.977	Q1	0.997
Q2	1.991	Q2	0.997
Q3	2.021	Q3	0.998
σ	$3.102 \cdot 10^{-2}$	σ	$8.031 \cdot 10^{-4}$
Min	1.904	Min	0.994
Mean	1.997	Mean	0.997
Max	2.103	Max	0.999

Table S43. Modena, GALAXY, statistics, $w_j = Q_{ij}$: (a) fractal dimensions (D); (b) determination coefficients (R^2)

Modena, GALAXY		Modena, GALAXY	
D, Q$_{ij}$		R^2, Q$_{ij}$	
Q1	1.921	Q1	0.998
Q2	1.932	Q2	0.998
Q3	1.933	Q3	0.998
σ	$1.379 \cdot 10^{-2}$	σ	$4.230 \cdot 10^{-4}$
Min	1.894	Min	0.996
Mean	1.928	Mean	0.998
Max	1.969	Max	0.999

3.2.3.2. NSGA-II

Figure S73 shows the non-dominated Pareto Front (PF) of Modena obtained through the application of NSGA-II [17]. Figure S74 shows the hydraulic gradient surface (HGS) of the [min(C), min(D)], [knee(C), knee(NRI)], [max(C), max(NRI)] design outcomes representing the extreme values of the energy (HGL) infrastructural (d) and flow distribution patterns of Modena through this design methodology. Figure S75 shows the achieved fractal dimension (D) of the extreme NSGA-II bi-objective designs. Table S44 shows the magnitudes of the fractal dimensions (D) of the extreme NSGA-II bi-objective designs of Modena.

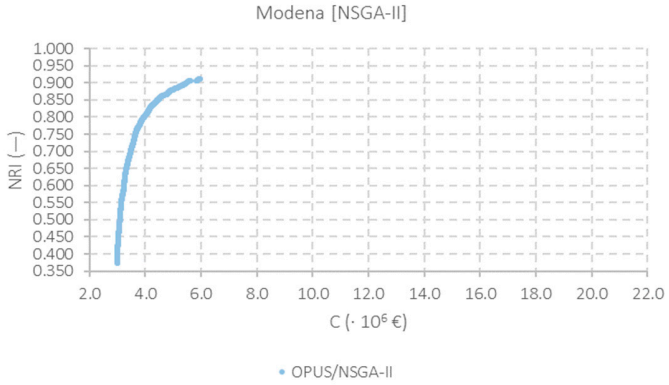
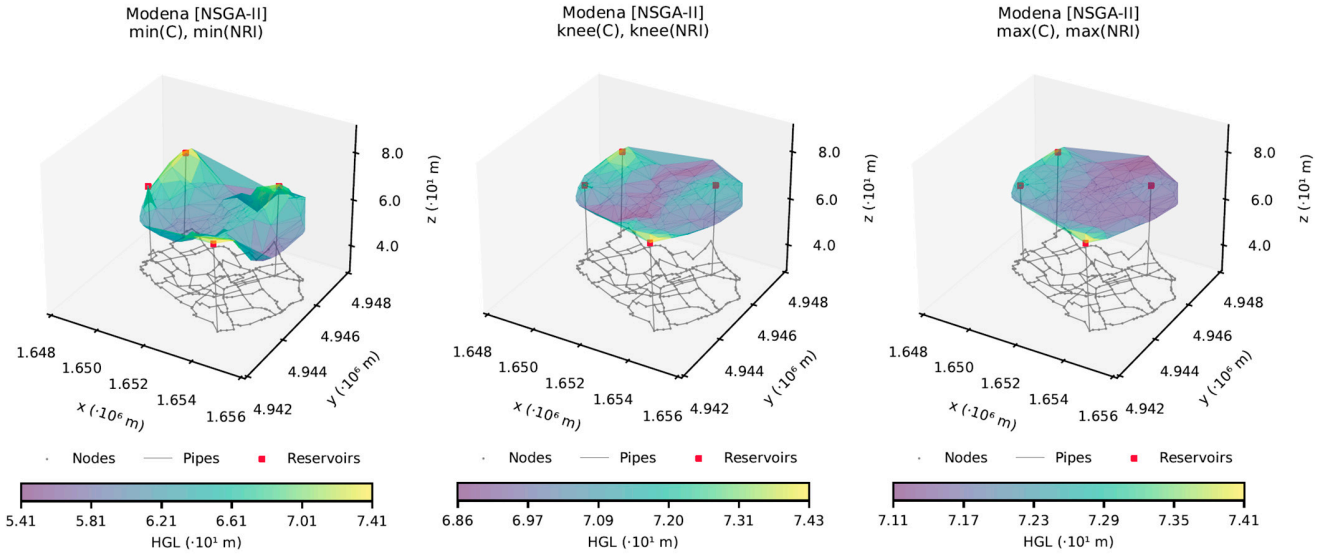
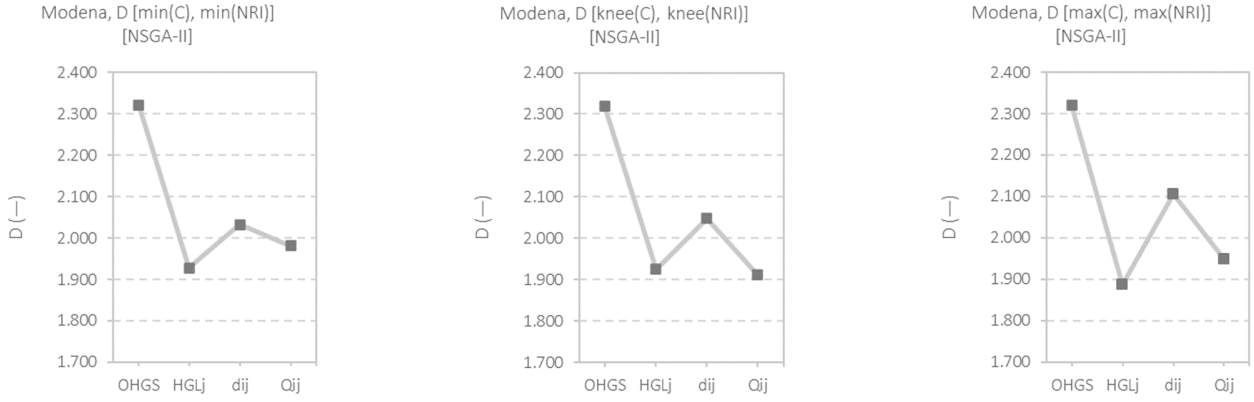


Figure S73. Modena, NSGA-II, Pareto Front (PF).



(a) *(b)* *(c)*

Figure S74. Modena, NSGA-II, hydraulic gradient surfaces (HGS): (a) [min(C), min(NRI)]; (b) [knee(C), knee(NRI)]; (c) [max(C), max(NRI)].



(a) *(b)* *(c)*

Figure S75. Modena, NSGA-II, fractal dimensions (D): (a) [min(C), min(NRI)]; (b) [knee(C), knee(NRI)]; (c) [max(C), max(NRI)].

Table S44. Fractal dimensions (D) of the extreme NSGA-II bi-objective designs of Modena.

Modena [min(C), min(NRI)] NSGA-II			Modena [knee(C), knee(NRI)] NSGA-II			Modena [max(C), max(NRI)] NSGA-II		
D, OHGS	2.320		D, OHGS	2.320		D, OHGS	2.320	
w_j	D	R^2	w_j	D	R^2	w_j	D	R^2
HGL_j	1.928	0.998	HGL_j	1.925	1.000	HGL_j	1.887	1.000
d_{ij}	2.033	0.998	d_{ij}	2.048	0.997	d_{ij}	2.105	0.997
Q_{ij}	1.981	0.999	Q_{ij}	1.911	0.997	Q_{ij}	1.948	0.998

Figure S76 shows the fractal dimensions (D) of the individuals of the non-dominated Pareto Front (PF) obtained through NSGA-II organized from minimum constructive cost (C) to maximum constructive cost (C). Figure S77 shows statistics of the design individuals obtained by the implementation of this methodology. Figure S78 to Figure S80 show the box whiskers plot of the fractal dimensions (D) considering the energy (HGL_j), infrastructure (d_{ij}) and flow (Q_{ij}) distribution patterns of each resulting individual. Finally, Table S45 to Table S47 show relevant statistics of the computed fractal dimensions (D) and the determination coefficients (R^2) associated to each computation.

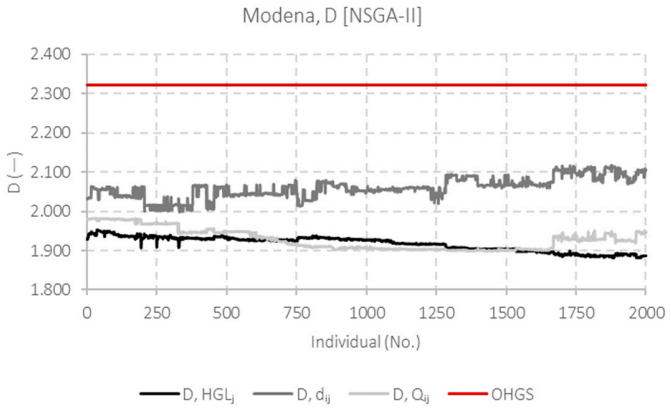
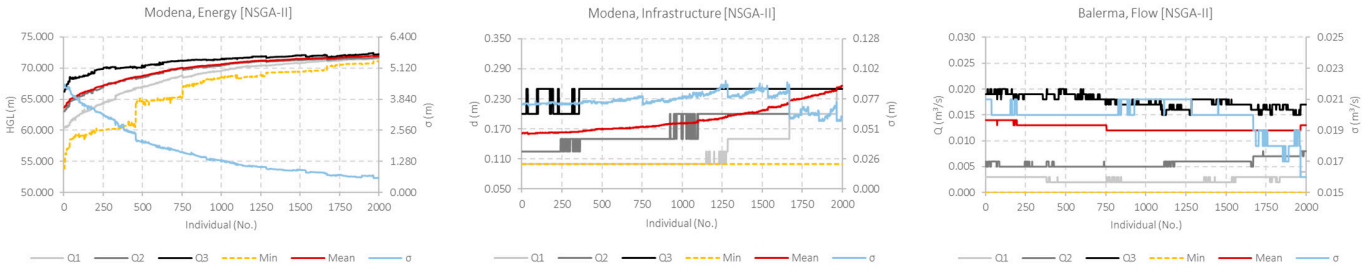


Figure S76. Modena, NSGA-II, fractal dimensions (D).



(a) *(b)* *(c)*

Figure S77. Modena, NSGA-II, statistics of the non-dominated individuals: (a) energy (HGL); (b) infrastructure (d); (c) flow (Q).

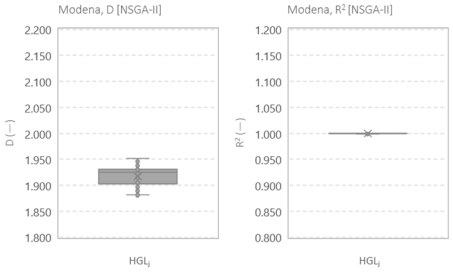


Figure S78. Modena, NSGA-II, box whiskers plots, $w_j = HGL_j$: (a) fractal dimensions (D); (b) determination coefficients (R^2).

Table S45. Modena, NSGA-II, statistics, $w_j = HGL_j$: (a) fractal dimensions (D); (b) determination coefficients (R^2).

Modena, NSGA-II		Modena, NSGA-II	
D, HGL_j		R^2, HGL_j	
Q1	1.903	Q1	0.999
Q2	1.925	Q2	1.000
Q3	1.931	Q3	1.000
σ	$1.803 \cdot 10^{-2}$	σ	$5.913 \cdot 10^{-4}$
Min	1.881	Min	0.998
Mean	1.917	Mean	1.000
Max	1.952	Max	1.000

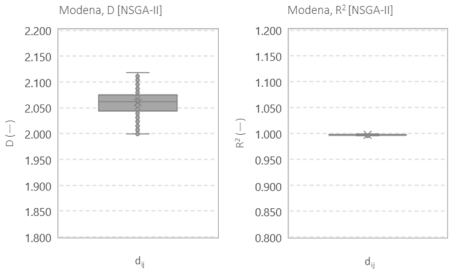


Figure S79. Modena, NSGA-II, box whiskers plots, $w_j = d_{ij}$: (a) fractal dimensions (D); (b) determination coefficients (R^2).

Table S46. Modena, NSGA-II, statistics, $w_j = d_{ij}$: (a) fractal dimensions (D); (b) determination coefficients (R^2).

Modena, NSGA-II		Modena, NSGA-II	
D, d_{ij}		R^2, d_{ij}	
Q1	2.043	Q1	0.997
Q2	2.061	Q2	0.997
Q3	2.075	Q3	0.998
σ	$2.619 \cdot 10^{-2}$	σ	$6.695 \cdot 10^{-4}$
Min	1.999	Min	0.996
Mean	2.060	Mean	0.997
Max	2.118	Max	0.999

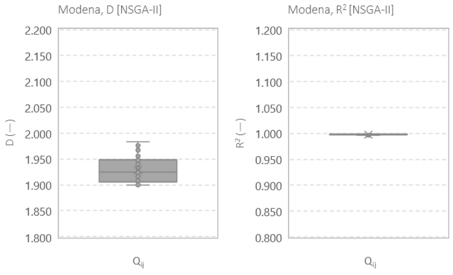


Figure S80. Modena, NSGA-II, box whiskers plots, $w_j = Q_{ij}$: (a) fractal dimensions (D); (b) determination coefficients (R^2).

Table S47. Modena, NSGA-II, statistics, $w_j = Q_{ij}$: (a) fractal dimensions (D); (b) determination coefficients (R^2).

Modena, NSGA-II		Modena, NSGA-II	
D, Q_{ij}		R^2, Q_{ij}	
Q1	1.905	Q1	0.997
Q2	1.925	Q2	0.997
Q3	1.948	Q3	0.998
σ	$2.649 \cdot 10^{-2}$	σ	$5.485 \cdot 10^{-4}$
Min	1.900	Min	0.996
Mean	1.929	Mean	0.997
Max	1.983	Max	0.999

3.2.3.3. OPUS/NSGA-II

Figure S81 shows the non-dominated Pareto Front (PF) of Modena obtained through the application of OPUS/NSGA-II [17]. Figure S82 shows the hydraulic gradient surface (HGS) of the [min(C), min(D)], [knee(C), knee(NRI)], [max(C), max(NRI)] design outcomes representing the extreme values of the energy (HGL) infrastructural (d) and flow distribution patterns of Modena through this design methodology. Figure S83 shows the achieved fractal dimension (D) of the extreme OPUS/NSGA-II bi-objective designs. Table S48 shows the magnitudes of the fractal dimensions (D) of the extreme OPUS/NSGA-II bi-objective designs of Modena.

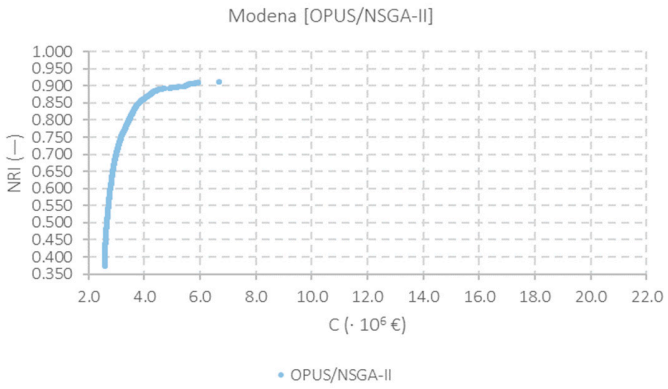
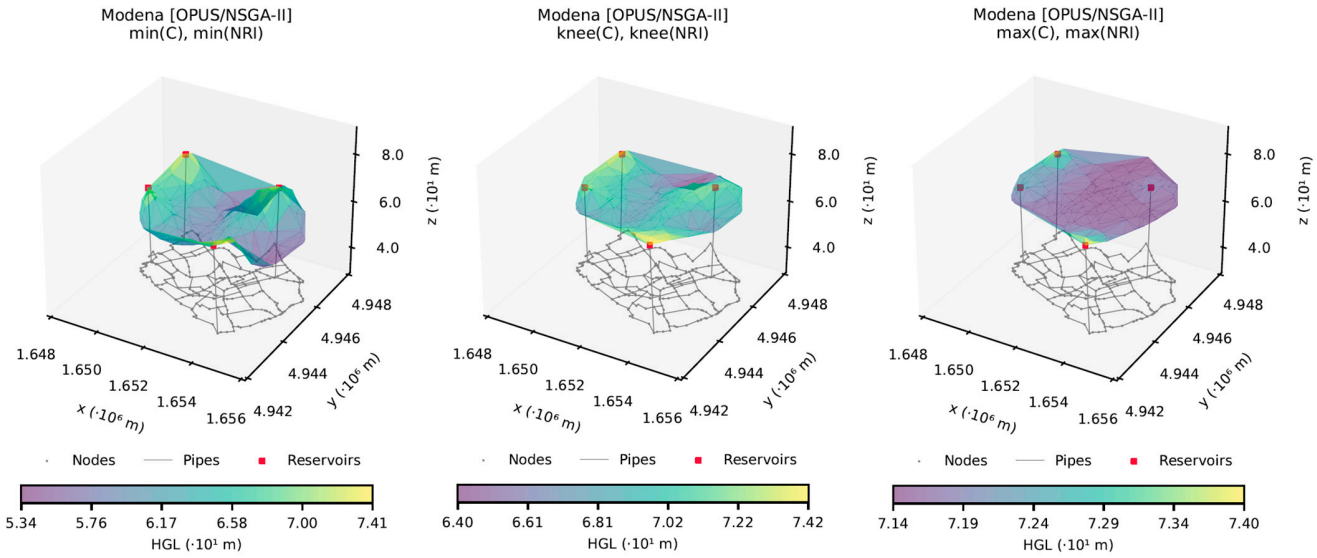
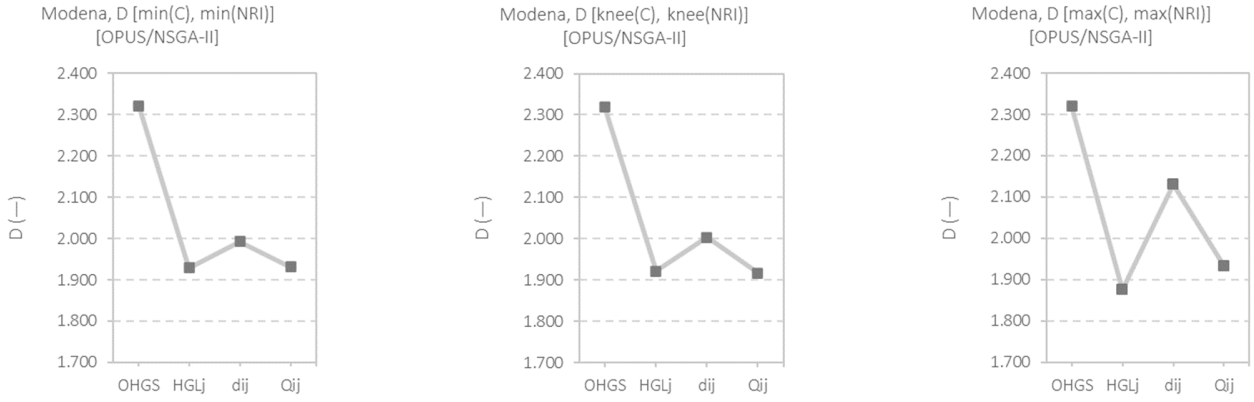


Figure S81. Modena, OPUS/NSGA-II, Pareto Front (PF).



(a) *(b)* *(c)*

Figure S82. Modena, OPUS/NSGA-II, hydraulic gradient surfaces (HGS): (a) [min(C), min(NRI)]; (b) [knee(C), knee(NRI)]; (c) [max(C), max(NRI)].



(a) *(b)* *(c)*

Figure S83. Modena, OPUS/NSGA-II, fractal dimensions (D): (a) [min(C), min(NRI)]; (b) [knee(C), knee(NRI)]; (c) [max(C), max(NRI)].

Table S48. Fractal dimensions (D) of the extreme OPUS/NSGA-II bi-objective designs of Modena.

Modena [min(C), min(NRI)] OPUS/NSGA-II			Modena [knee(C), knee(NRI)] OPUS/NSGA-II			Modena [max(C), max(NRI)] NSGA-II		
D, OHGS	2.320		D, OHGS	2.320		D, OHGS	2.320	
w_j	D	R^2	w_j	D	R^2	w_j	D	R^2
HGL_j	1.929	0.997	HGL_j	1.922	0.999	HGL_j	1.876	1.000
d_{ij}	1.993	0.997	d_{ij}	2.003	0.998	d_{ij}	2.130	0.997
Q_{ij}	1.931	0.998	Q_{ij}	1.917	0.997	Q_{ij}	1.933	0.997

Figure S84 shows the fractal dimensions (D) of the individuals of the non-dominated Pareto Front (PF) obtained through OPUS/NSGA-II organized from minimum constructive cost (C) to maximum constructive cost (C). Figure S85 shows statistics of the design individuals obtained by the implementation of this methodology. Figure S86 to Figure S88 show the box whiskers plot of the fractal dimensions (D) considering the energy (HGL_j), infrastructure (d_{ij}) and flow (Q_{ij}) distribution patterns of each resulting individual. Finally, Table S49 to Table S51 show relevant statistics of the computed fractal dimensions (D) and the determination coefficients (R^2) associated to each computation.

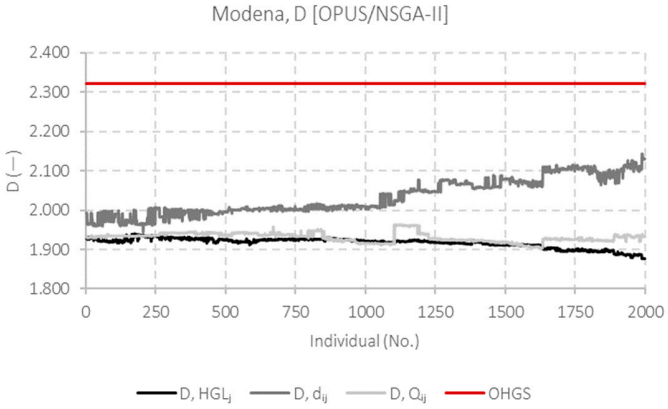
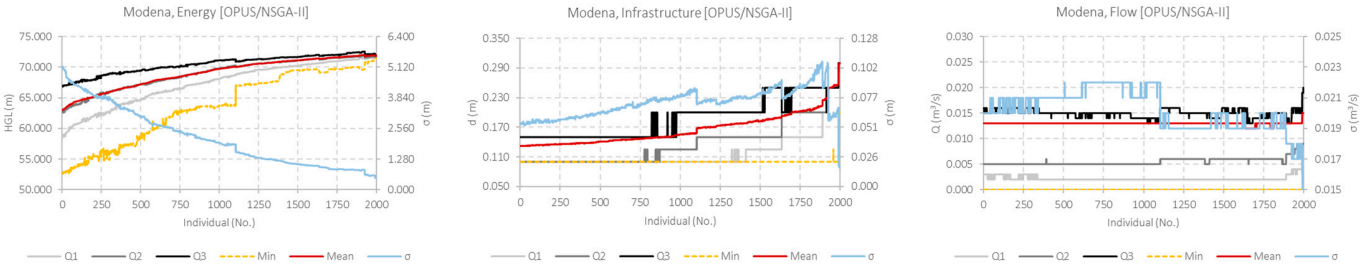


Figure S84. Modena, OPUS/NSGA-II, fractal dimensions (D).



(a) *(b)* *(c)*

Figure S85. Modena, OPUS/NSGA-II, statistics of the non-dominated individuals: (a) energy (HGL); (b) infrastructure (d); (c) flow (Q).

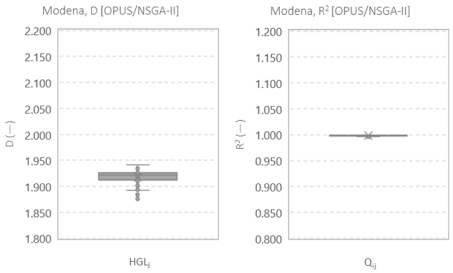


Figure S86. Modena, OPUS/NSGA-II, box whiskers plots, w_j = HGL_j: (a) fractal dimensions (D); (b) determination coefficients (R^2).

Table S49. Modena, OPUS/NSGA-II, statistics, w_j = HGL_j: (a) fractal dimensions (D); (b) determination coefficients (R^2).

Modena, OPUS/NSGA-II		Modena, OPUS/NSGA-II	
D, HGL_j		R^2, HGL_j	
Q1	1.912	Q1	0.998
Q2	1.921	Q2	0.999
Q3	1.926	Q3	1.000
σ	$1.283 \cdot 10^{-2}$	σ	$9.792 \cdot 10^{-4}$
Min	1.876	Min	0.997
Mean	1.917	Mean	0.999
Max	1.941	Max	1.000

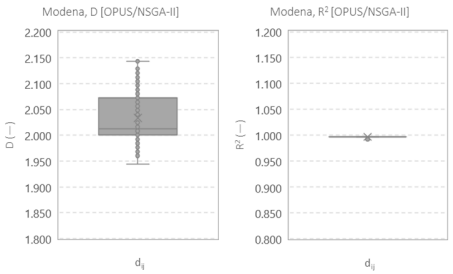


Figure S87. Modena, OPUS/NSGA-II, box whiskers plots, w_j = d_{ij}: (a) fractal dimensions (D); (b) determination coefficients (R^2).

Table S50. Modena, OPUS/NSGA-II, statistics, w_j = d_{ij}: (a) fractal dimensions (D); (b) determination coefficients (R^2).

Modena, OPUS/NSGA-II		Modena, OPUS/NSGA-II	
D, d_{ij}		R^2, d_{ij}	
Q1	2.000	Q1	0.997
Q2	2.012	Q2	0.997
Q3	2.072	Q3	0.997
σ	$4.521 \cdot 10^{-2}$	σ	$7.446 \cdot 10^{-4}$
Min	1.944	Min	0.992
Mean	2.034	Mean	0.997
Max	2.143	Max	0.998

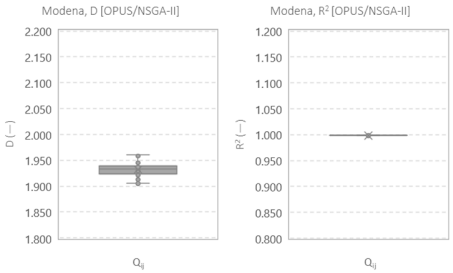


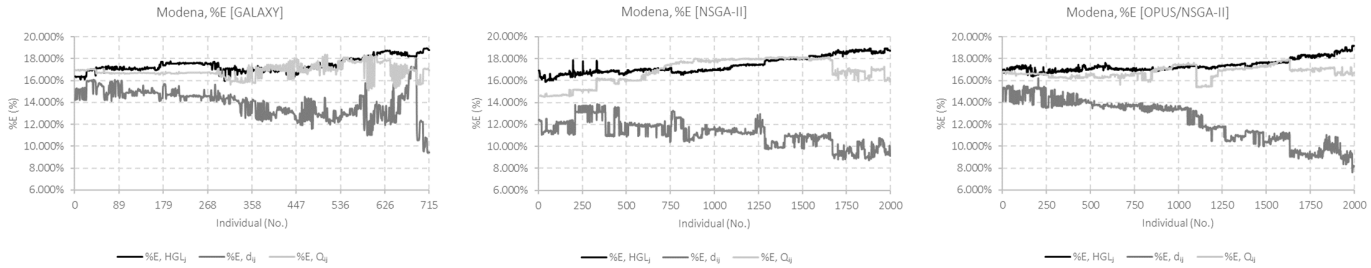
Figure S88. Modena, OPUS/NSGA-II, box whiskers plots, $w_j = Q_{ij}$: (a) fractal dimensions (D); (b) determination coefficients (R^2).

Table S51. Modena, OPUS/NSGA-II, statistics, $w_j = Q_{ij}$: (a) fractal dimensions (D); (b) determination coefficients (R^2).

Modena, OPUS/NSGA-II		Modena, OPUS/NSGA-II	
D, Q_{ij}		R^2, Q_{ij}	
Q1	1.924	Q1	0.997
Q2	1.933	Q2	0.998
Q3	1.939	Q3	0.998
σ	$1.159 \cdot 10^{-2}$	σ	$5.050 \cdot 10^{-4}$
Min	1.905	Min	0.996
Mean	1.932	Mean	0.998
Max	1.963	Max	0.998

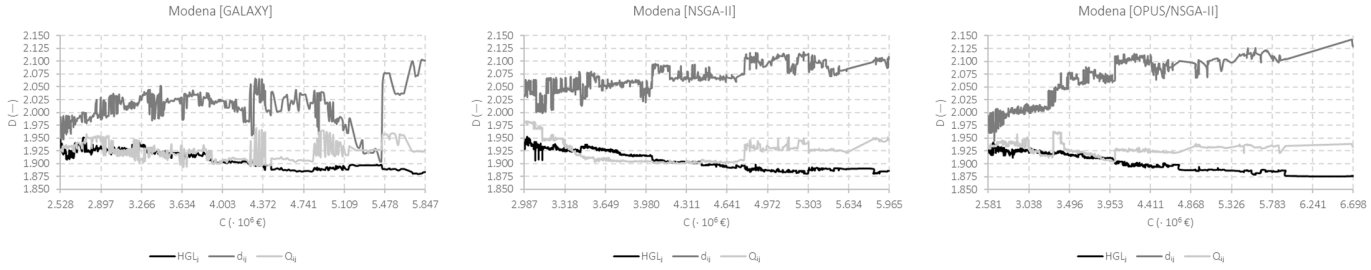
3.2.3.4. Analysis of Results

Figure S89 shows the percent error (%E) between the fractal dimension of the Optimal Hydraulic Gradient Surface (OHGS) with respect to the computed fractal dimensions (D) considering each hydraulic criterion (w_j) by case study. Figure S90 shows the relationship between the computed fractal dimensions (D) and the constructive cost (C) of each design solution by case study. Table S52 shows the reason between the fractal dimensions (D) of the minimum constructive cost (C) individual and the maximum constructive cost (C) individual by design methodology.



(a) *(b)* *(c)*

Figure S89. Percent error (%E) between the fractal dimension of the Optimal Hydraulic Gradient Surfaces (OHGS) and the computed fractal dimensions (D): Modena (a) GALAXY; (b) NSGA-II; (c) OPUS/NSGA-II.



(a) *(b)* *(c)*

Figure S90. Relationship between the fractal dimensions (D) and the constructive costs (C): Modena (a) GALAXY; (b) NSGA-II; (c) OPUS/NSGA-II,

Table S52. Reason between the fractal dimension (D) of the minimum and maximum constructive cost (C) individual: Modena (a) GALAXY; (b) NSGA-II; (c) OPUS/NSGA-II.

Modena					
GALAXY		NSGA-II		OPUS/NSGA-II	
w_j	$D_{min(C)}/ D_{max(C)}$	w_j	$D_{min(C)}/ D_{max(C)}$	w_j	$D_{min(C)}/ D_{max(C)}$
HGL_j	0.971	HGL_j	0.978	HGL_j	0.973
d_{ij}	1.056	d_{ij}	1.035	d_{ij}	1.069
Q_{ij}	1.001	Q_{ij}	0.983	Q_{ij}	1.001

3.2.4. Pescara

Figure S91 shows the non-dominated Pareto Fronts (PF) of Pescara obtained through the application of NSGA-II (Deb et al., 2022), OPUS/NSGA-II (Páez et al., 2020) and GALAXY (Wang et al., 2017).

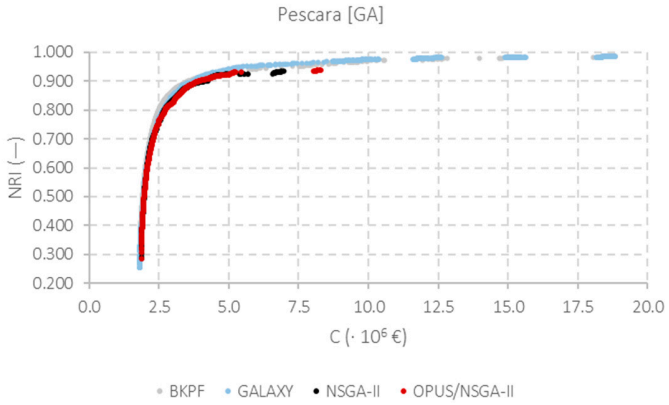


Figure S91. Pescara, genetic algorithms. Note: BKPF refers to the Best-Known Pareto Front found in the literature (Wang et al., 2017).

3.2.4.1. GALAXY

Figure S92 shows the non-dominated Pareto Front (PF) of Pescara obtained through the application of GALAXY [18]. Figure S93 shows the hydraulic gradient surface (HGS) of the [min(C), min(D)], [knee(C), knee(NRI)], [max(C), max(NRI)] design outcomes representing the extreme values of the energy (HGL) infrastructural (d) and flow distribution patterns of Pescara through this design methodology. Figure S94 shows the achieved fractal dimension (D) of the extreme GALAXY bi-objective designs. Table S53 shows the magnitudes of the fractal dimensions (D) of the extreme GALAXY bi-objective designs of Pescara.

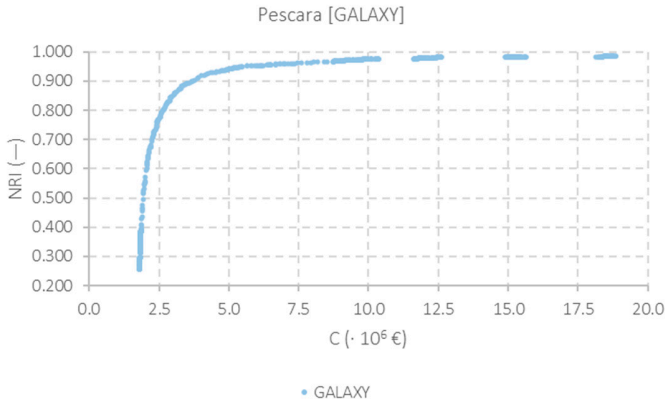
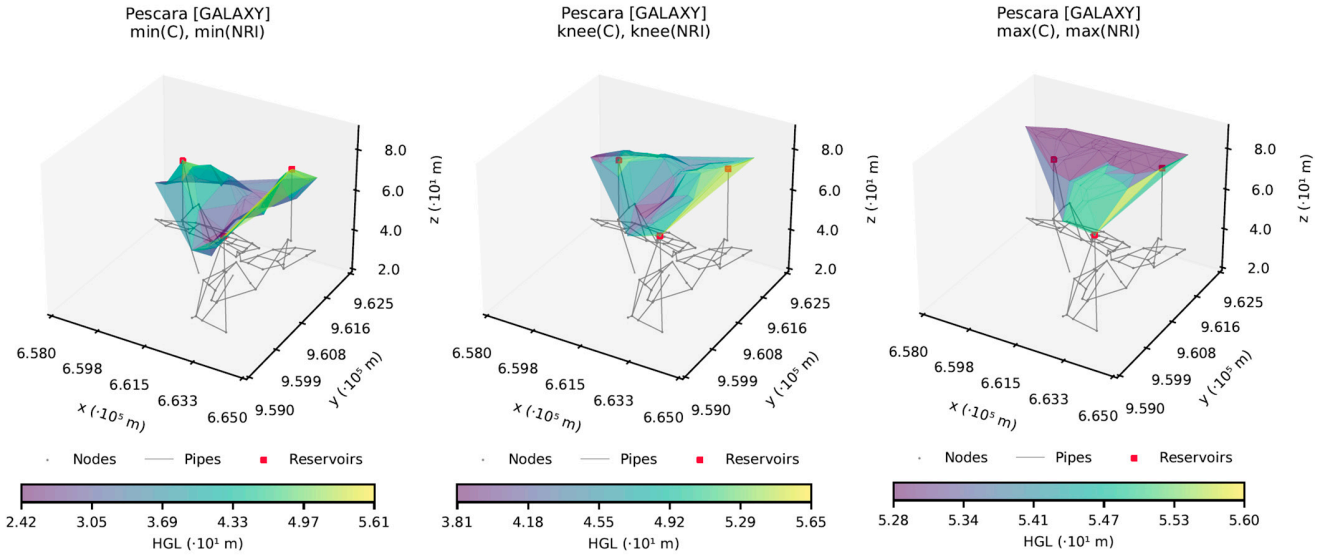
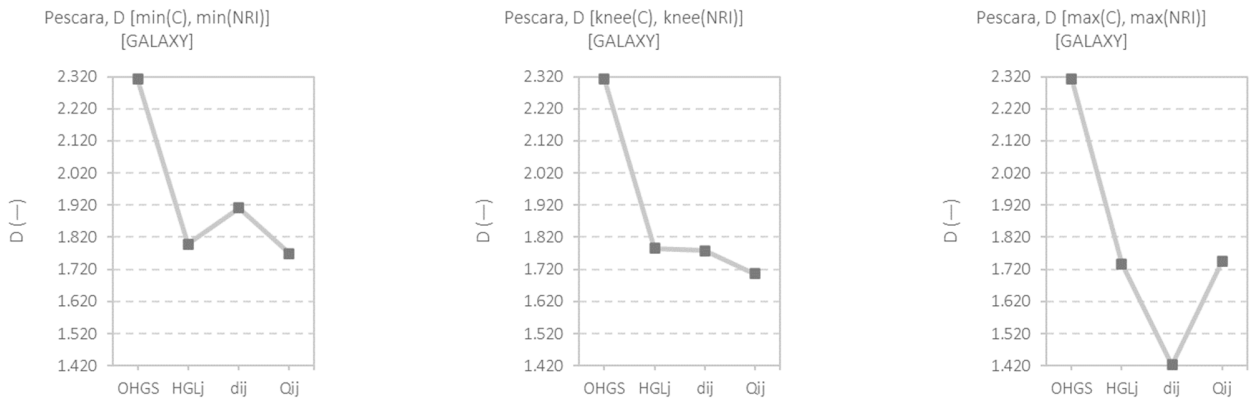


Figure S92. Pescara, GALAXY, Pareto Front (PF).



(a) *(b)* *(c)*

Figure S93. Modena, GALAXY, hydraulic gradient surfaces (HGS): (a) [min(C), min(NRI)]; (b) [knee(C), knee(NRI)]; (c) [max(C), max(NRI)].



(a) *(b)* *(c)*

Figure S94. Pescara, GALAXY, fractal dimensions (D): (a) [min(C), min(NRI)]; (b) [knee(C), knee(NRI)]; (c) [max(C), max(NRI)].

Table S53. Fractal dimensions (D) of the extreme GALAXY bi-objective designs of Pescara.

Pescara [min(C), min(NRI)] GALAXY		
D, OHGS	2.313	
w_j	D	R^2
HGL_j	1.799	0.998
d_{ij}	1.911	0.991
Q_{ij}	1.770	0.999

Pescara [knee(C), knee(NRI)] GALAXY		
D, OHGS	2.313	
w_j	D	R^2
HGL_j	1.786	0.998
d_{ij}	1.778	0.996
Q_{ij}	1.707	0.999

Pescara [max(C), max(NRI)] GALAXY		
D, OHGS	2.313	
w_j	D	R^2
HGL_j	1.737	0.999
d_{ij}	1.422	0.955
Q_{ij}	1.744	0.999

Figure S95 shows the fractal dimensions (D) of the individuals of the non-dominated Pareto Front (PF) obtained through GALAXY organized from minimum constructive cost (C) to maximum constructive cost (C). Figure S96 shows statistics of the design individuals obtained by the implementation of this methodology. Figure S97 to Figure S99 show the box whiskers plot of the fractal dimensions (D) considering the energy (HGL_j), infrastructure (d_{ij}) and flow (Q_{ij}) distribution patterns of each resulting individual. Finally, Table S54 to Table S56 show relevant statistics of the computed fractal dimensions (D) and the determination coefficients (R^2) associated to each computation.

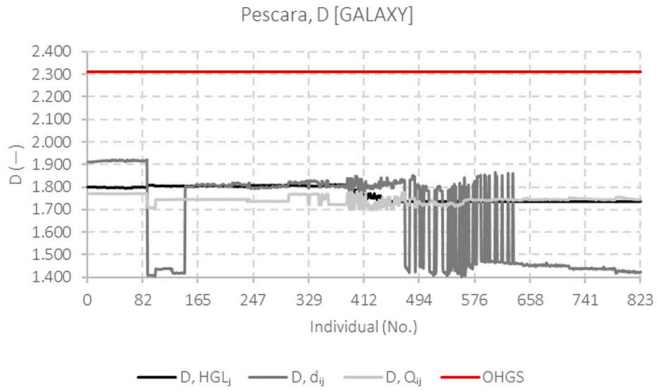
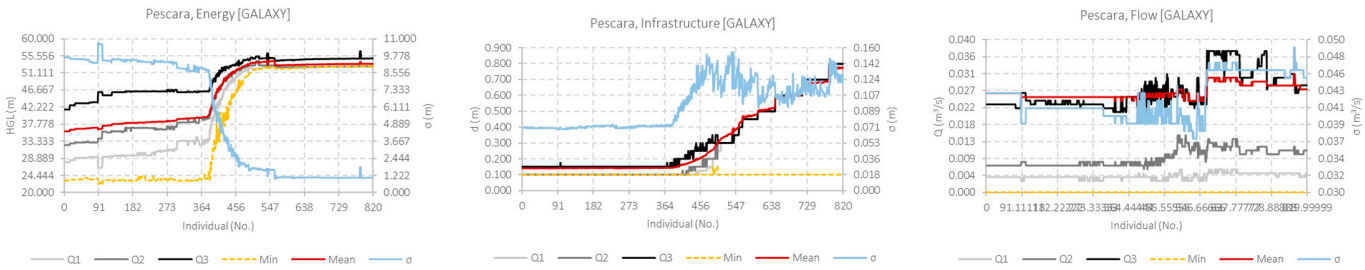


Figure S95. Pescara, GALAXY, fractal dimensions (D).



(a) *(b)* *(c)*

Figure S96. Pescara, GALAXY, statistics of the non-dominated individuals: (a) energy (HGL); (b) infrastructure (d); (c) flow (Q).

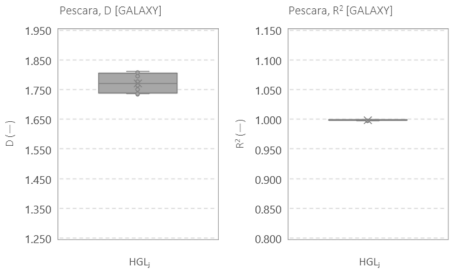


Figure S97. Modena, GALAXY, box whiskers plots, $w_j = HGL_j$: (a) fractal dimensions (D); (b) determination coefficients (R^2).

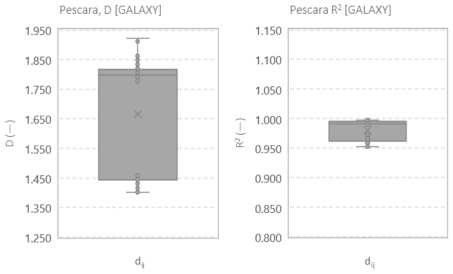


Figure S98. Pescara, GALAXY, box whiskers plots, $w_j = d_{ij}$: (a) fractal dimensions (D); (b) determination coefficients (R^2).

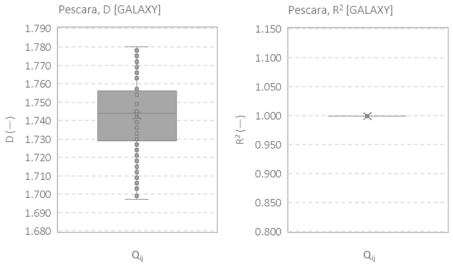


Figure S99. Pescara, GALAXY, box whiskers plots, $w_j = Q_{ij}$: (a) fractal dimensions (D); (b) determination coefficients (R^2).

Table S54. Pescara, GALAXY, statistics, $w_j = HGL_j$: (a) fractal dimensions (D); (b) determination coefficients (R^2).

Pescara, GALAXY		Pescara, GALAXY	
D, HGL_j		R^2, HGL_j	
Q1	1.737	Q1	0.998
Q2	1.771	Q2	0.998
Q3	1.804	Q3	0.999
σ	$3.247 \cdot 10^{-2}$	σ	$5.267 \cdot 10^{-4}$
Min	1.735	Min	0.997
Mean	1.770	Mean	0.998
Max	1.811	Max	0.999

Table S55. Pescara, GALAXY, statistics, $w_j = d_{ij}$: (a) fractal dimensions (D); (b) determination coefficients (R^2).

Pescara, GALAXY		Pescara, GALAXY	
D, d_{ij}		R^2, d_{ij}	
Q1	1.443	Q1	0.962
Q2	1.798	Q2	0.991
Q3	1.816	Q3	0.995
σ	$1.966 \cdot 10^{-1}$	σ	$1.661 \cdot 10^{-2}$
Min	1.400	Min	0.952
Mean	1.666	Mean	0.980
Max	1.922	Max	0.997

Table S56. Pescara, GALAXY, statistics, $w_j = Q_{ij}$: (a) fractal dimensions (D); (b) determination coefficients (R^2)

Pescara, GALAXY		Pescara, GALAXY	
D, Q_{ij}		R^2, Q_{ij}	
Q1	1.729	Q1	0.999
Q2	1.744	Q2	0.999
Q3	1.756	Q3	0.999
σ	$1.884 \cdot 10^{-2}$	σ	$1.244 \cdot 10^{-14}$
Min	1.697	Min	0.999
Mean	1.743	Mean	0.999
Max	1.78	Max	0.999

3.2.4.2. NSGA-II

Figure S100 shows the non-dominated Pareto Front (PF) of Pescara obtained through the application of NSGA-II [17]. Figure S101 shows the hydraulic gradient surface (HGS) of the [min(C), min(D)], [knee(C), knee(NRI)], [max(C), max(NRI)] design outcomes representing the extreme values of the energy (HGL) infrastructural (d) and flow distribution patterns of Pescara through this design methodology. Figure S102 shows the achieved fractal dimension (D) of the extreme NSGA-II bi-objective designs. Table S57 shows the magnitudes of the fractal dimensions (D) of the extreme NSGA-II bi-objective designs of Pescara.

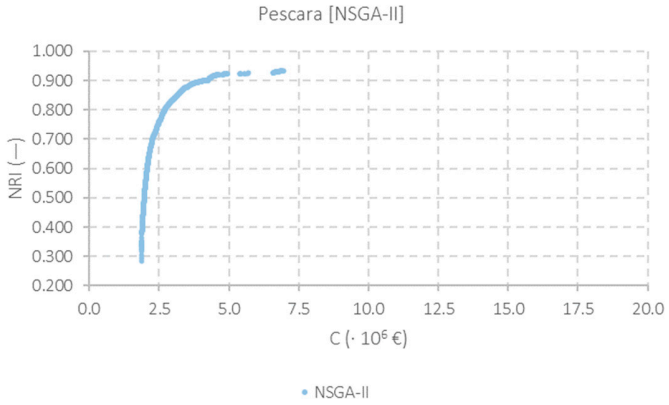
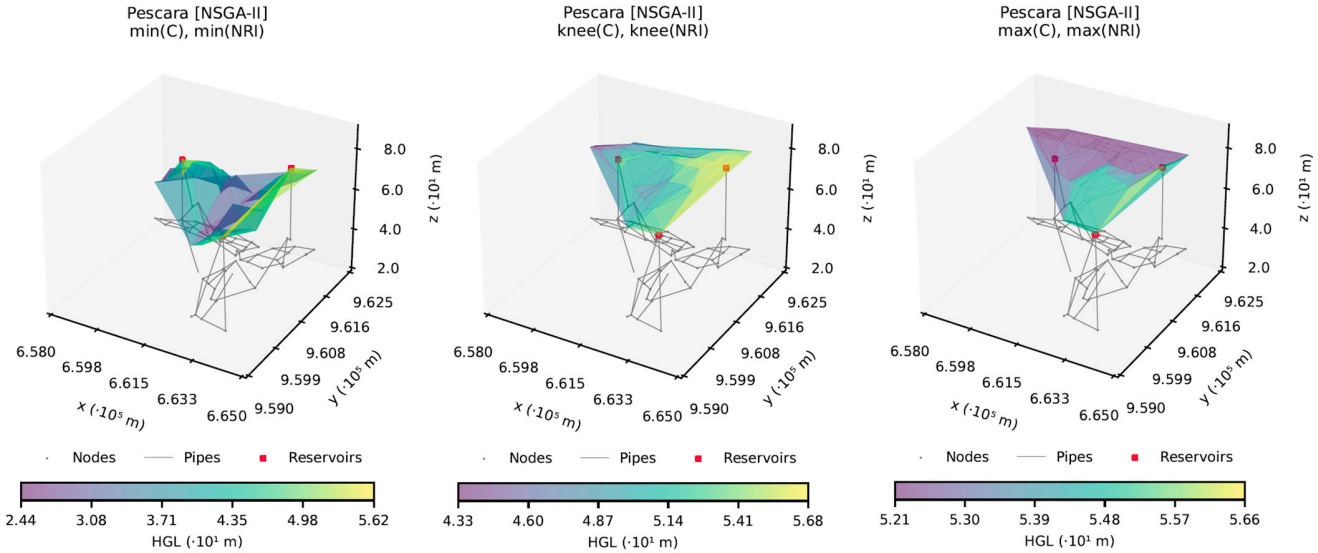
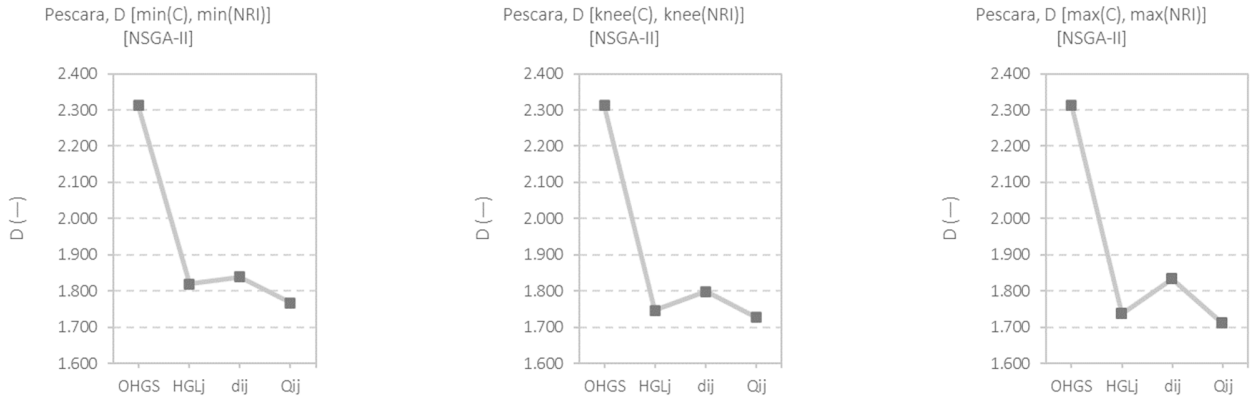


Figure S100. Pescara, NSGA-II, Pareto Front (PF).



(a) *(b)* *(c)*

Figure S101. Pescara, NSGA-II, hydraulic gradient surfaces (HGS): (a) [min(C), min(NRI)]; (b) [knee(C), knee(NRI)]; (c) [max(C), max(NRI)].



(a) *(b)* *(c)*

Figure S102. Pescara, NSGA-II, fractal dimensions (D): (a) [min(C), min(NRI)]; (b) [knee(C), knee(NRI)]; (c) [max(C), max(NRI)].

Table S57. Fractal dimensions (D) of the extreme NSGA-II bi-objective designs of Pescara.

Pescara [min(C), min(NRI)] NSGA-II		
D, OHGS	2.313	
w_j	D	R^2
HGL_j	1.820	0.997
d_{ij}	1.839	0.997
Q_{ij}	1.767	0.999

Pescara [knee(C), knee(NRI)] OPUS/NSGA-II		
D, OHGS	2.313	
w_j	D	R^2
HGL_j	1.747	0.998
d_{ij}	1.799	0.992
Q_{ij}	1.727	0.998

Pescara [max(C), max(NRI)] OPUS/NSGA-II		
D, OHGS	2.313	
w_j	D	R^2
HGL_j	1.737	0.999
d_{ij}	1.834	0.995
Q_{ij}	1.712	0.998

Figure S103 shows the fractal dimensions (D) of the individuals of the non-dominated Pareto Front (PF) obtained through NSGA-II organized from minimum constructive cost (C) to maximum constructive cost (C). Figure S104 shows statistics of the design individuals obtained by the implementation of this methodology. Figure S105 to Figure S107 show the box whiskers plot of the fractal dimensions (D) considering the energy (HGL_j), infrastructure (d_{ij}) and flow (Q_{ij}) distribution patterns of each resulting individual. Finally, Table S58 to Table S60 show relevant statistics of the computed fractal dimensions (D) and the determination coefficients (R^2) associated to each computation.

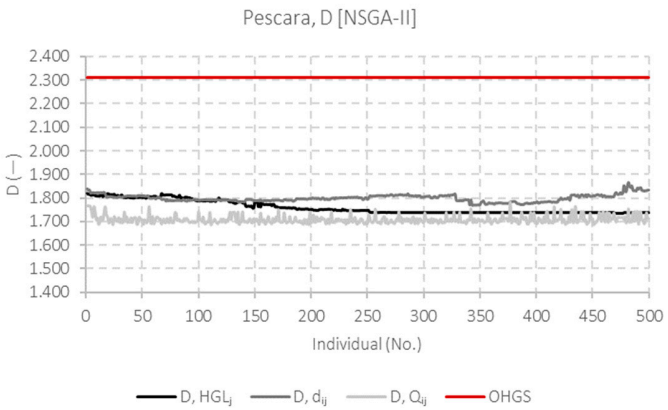
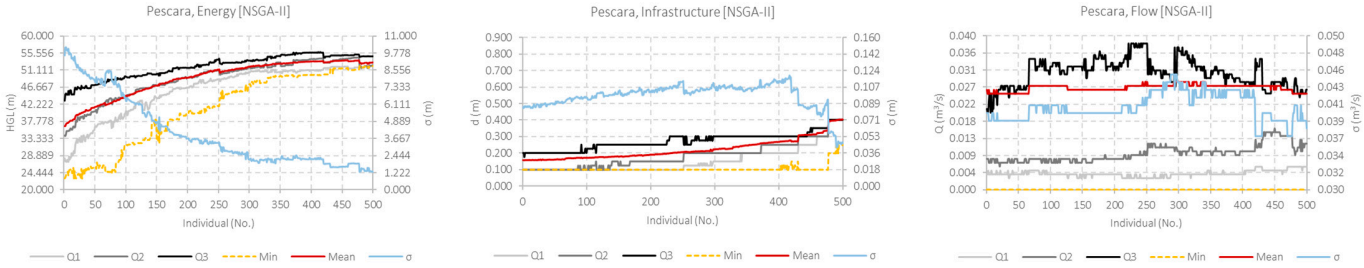


Figure S103. Pescara, NSGA-II, fractal dimensions (D).



(a) *(b)* *(c)*

Figure S104. Pescara, NSGA-II, statistics of the non-dominated individuals: (a) energy (HGL); (b) infrastructure (d); (c) flow (Q).

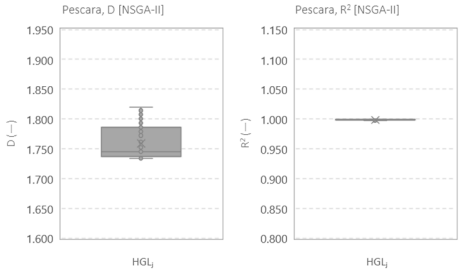


Figure S105. Pescara, NSGA-II, box whiskers plots, $w_j = HGL_j$: (a) fractal dimensions (D); (b) determination coefficients (R^2).

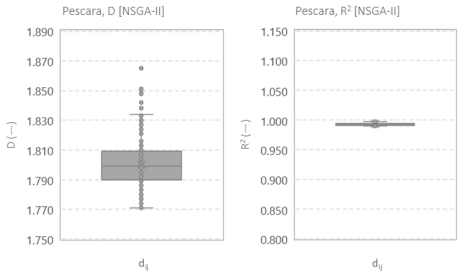


Figure S106. Pescara, NSGA-II, box whiskers plots, $w_j = d_{ij}$: (a) fractal dimensions (D); (b) determination coefficients (R^2).

Table S58. Pescara, NSGA-II, statistics, $w_j = HGL_j$: (a) fractal dimensions (D); (b) determination coefficients (R^2).

Pescara, NSGA-II		Pescara, NSGA-II	
D, HGL_j		R^2, HGL_j	
Q1	1.737	Q1	0.998
Q2	1.745	Q2	0.998
Q3	1.786	Q3	0.998
σ	$2.802 \cdot 10^{-2}$	σ	$7.336 \cdot 10^{-4}$
Min	1.734	Min	0.997
Mean	1.759	Mean	0.998
Max	1.820	Max	0.999

Table S59. Modena, NSGA-II, statistics, $w_j = d_{ij}$: (a) fractal dimensions (D); (b) determination coefficients (R^2).

Pescara, NSGA-II		Pescara, NSGA-II	
D, d_{ij}		R^2, d_{ij}	
Q1	1.790	Q1	0.991
Q2	1.799	Q2	0.993
Q3	1.809	Q3	0.994
σ	$1.491 \cdot 10^{-2}$	σ	$1.532 \cdot 10^{-3}$
Min	1.771	Min	0.990
Mean	1.800	Mean	0.993
Max	1.865	Max	0.997

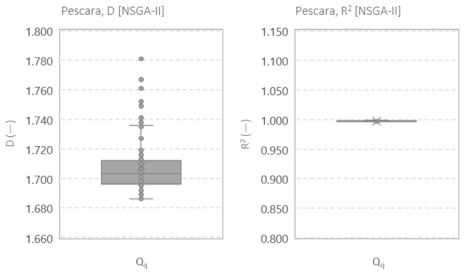


Figure S107. Pescara, NSGA-II, box whiskers plots, $w_j = Q_{ij}$: (a) fractal dimensions (D); (b) determination coefficients (R^2).

Table S60. Pescara, NSGA-II, statistics, $w_j = Q_{ij}$: (a) fractal dimensions (D); (b) determination coefficients (R^2).

Pescara, NSGA-II		Pescara, NSGA-II	
D, Q_{ij}		R^2, Q_{ij}	
Q1	1.696	Q1	0.997
Q2	1.703	Q2	0.997
Q3	1.712	Q3	0.998
σ	$1.672 \cdot 10^{-2}$	σ	$6.586 \cdot 10^{-4}$
Min	1.686	Min	0.997
Mean	1.708	Mean	0.997
Max	1.781	Max	0.999

3.2.4.3. OPUS/NSGA-II

Figure S108 shows the non-dominated Pareto Front (PF) of Pescara obtained through the application of OPUS/NSGA-II [17]. Figure S109 shows the hydraulic gradient surface (HGS) of the [min(C), min(D)], [knee(C), knee(NRI)], [max(C), max(NRI)] design outcomes representing the extreme values of the energy (HGL) infrastructural (d) and flow distribution patterns of Pescara through this design methodology. Figure S110 shows the achieved fractal dimension (D) of the extreme OPUS/NSGA-II bi-objective designs. Table S61 shows the magnitudes of the fractal dimensions (D) of the extreme OPUS/NSGA-II bi-objective designs of Pescara.

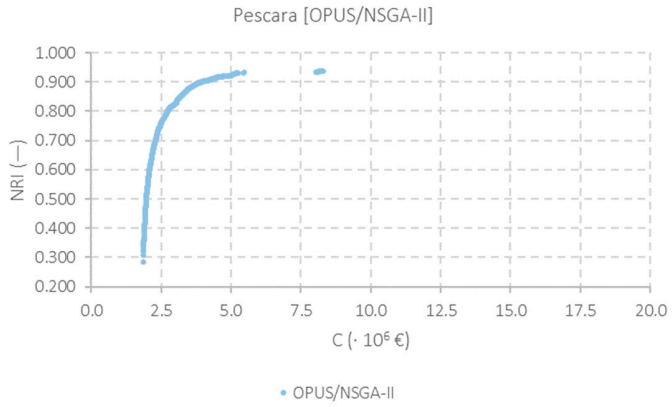
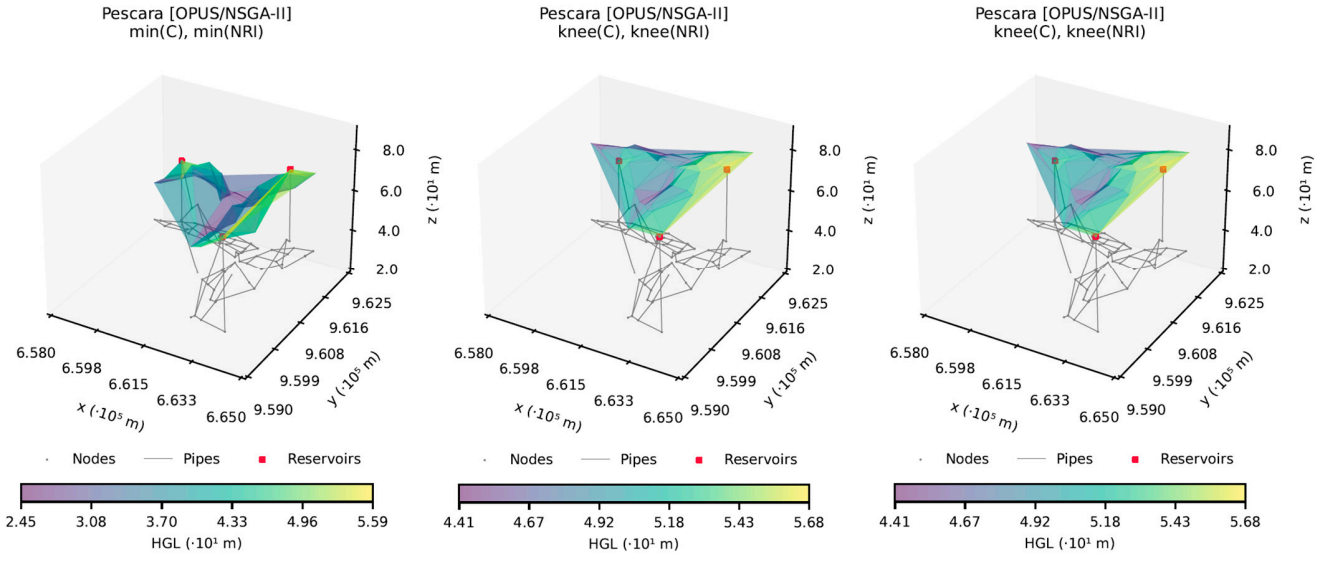
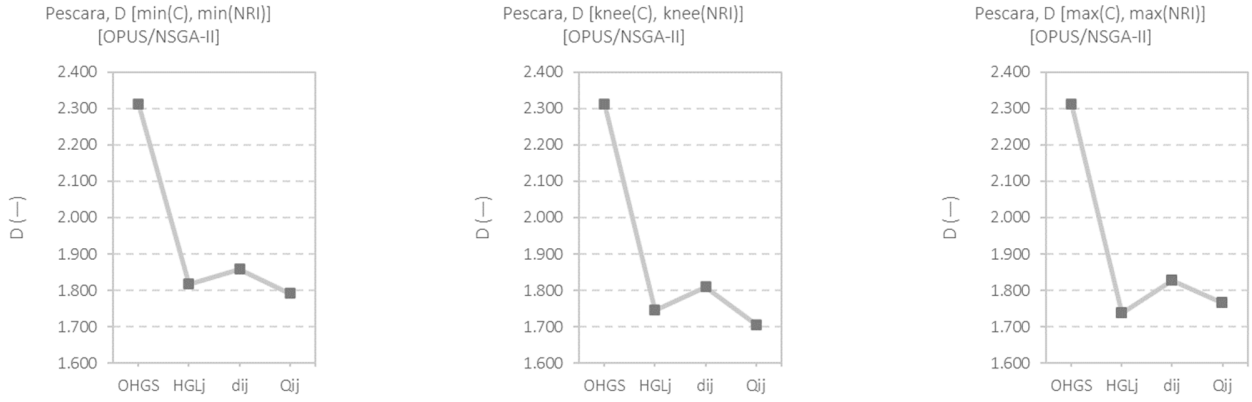


Figure S108. Pescara, OPUS/NSGA-II, Pareto Front (PF).



(a) *(b)* *(c)*

Figure S109. Pescara, OPUS/NSGA-II, hydraulic gradient surfaces (HGS): (a) [min(C), min(NRI)]; (b) [knee(C), knee(NRI)]; (c) [max(C), max(NRI)].



(a) *(b)* *(c)*

Figure S110. Pescara, OPUS/NSGA-II, fractal dimensions (D): (a) [min(C), min(NRI)]; (b) [knee(C), knee(NRI)]; (c) [max(C), max(NRI)].

Table S61. Fractal dimensions (D) of the extreme OPUS/NSGA-II bi-objective designs of Pescara.

Pescara [min(C), min(NRI)] OPUS/NSGA-II			Pescara [knee(C), knee(NRI)] OPUS/NSGA-II			Pescara [max(C), max(NRI)] OPUS/NSGA-II		
D, OHGS	2.313		D, OHGS	2.313		D, OHGS	2.313	
w_j	D	R^2	w_j	D	R^2	w_j	D	R^2
HGL_j	1.817	0.997	HGL_j	1.746	0.998	HGL_j	1.737	0.999
d_{ij}	1.858	0.998	d_{ij}	1.809	0.994	d_{ij}	1.828	0.992
Q_{ij}	1.792	0.999	Q_{ij}	1.706	0.998	Q_{ij}	1.765	0.999

Figure S111 shows the fractal dimensions (D) of the individuals of the non-dominated Pareto Front (PF) obtained through OPUS/NSGA-II organized from minimum constructive cost (C) to maximum constructive cost (C). Figure S112 shows statistics of the design individuals obtained by the implementation of this methodology. Figure S113 to Figure S115 show the box whiskers plot of the fractal dimensions (D) considering the energy (HGL_j), infrastructure (d_{ij}) and flow (Q_{ij}) distribution patterns of each resulting individual. Finally, Table S62 to Table S64 show relevant statistics of the computed fractal dimensions (D) and the determination coefficients (R^2) associated to each computation.

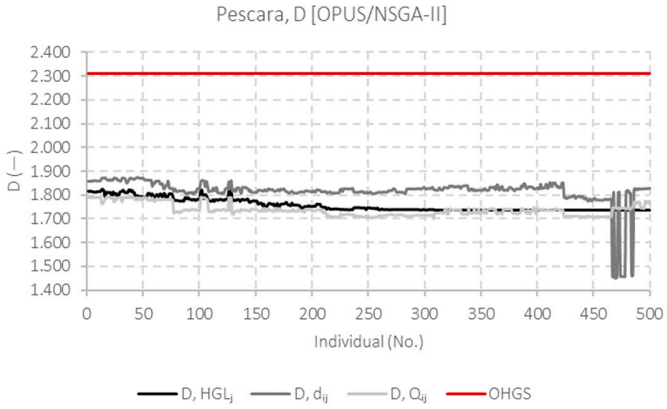
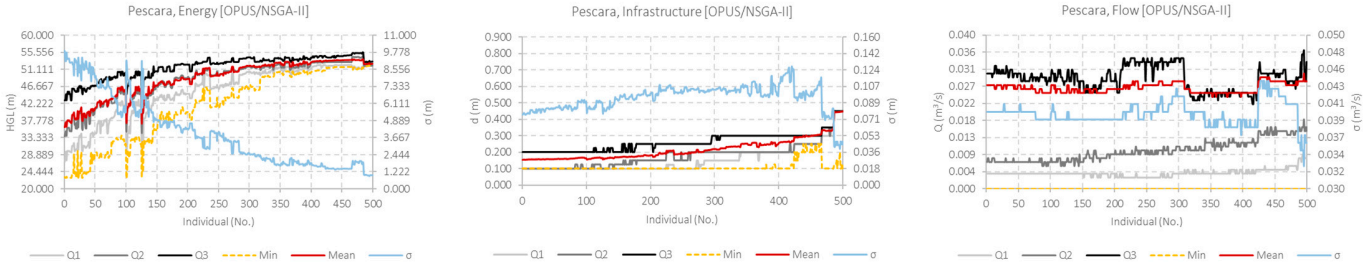


Figure S111. Pescara, OPUS/NSGA-II, fractal dimensions (D).



(a) *(b)* *(c)*

Figure S112. Pescara, OPUS/NSGA-II, statistics of the non-dominated individuals: (a) energy (HGL); (b) infrastructure (d); (c) flow (Q).

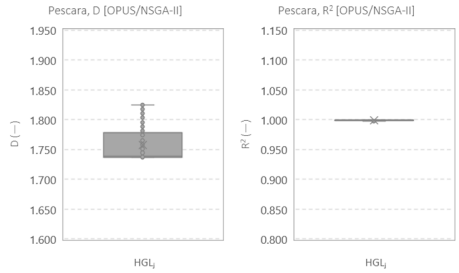


Figure S113. Pescara, OPUS/NSGA-II, box whiskers plots, w_j = HGL_j: (a) fractal dimensions (D); (b) determination coefficients (R^2).

Table S62. Pescara, OPUS/NSGA-II, statistics, w_j = HGL_j: (a) fractal dimensions (D); (b) determination coefficients (R^2).

Pescara, OPUS/NSGA-II		Pescara, OPUS/NSGA-II	
D, HGL_j		R^2, HGL_j	
Q1	1.737	Q1	0.998
Q2	1.739	Q2	0.999
Q3	1.778	Q3	0.999
σ	$2.637 \cdot 10^{-2}$	σ	$6.680 \cdot 10^{-4}$
Min	1.737	Min	0.997
Mean	1.757	Mean	0.998
Max	1.824	Max	0.999

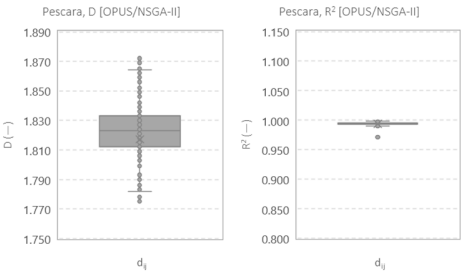


Figure S114. Pescara, OPUS/NSGA-II, box whiskers plots, w_j = d_{ij}: (a) fractal dimensions (D); (b) determination coefficients (R^2).

Table S63. Pescara, OPUS/NSGA-II, statistics, w_j = d_{ij}: (a) fractal dimensions (D); (b) determination coefficients (R^2).

Pescara, OPUS/NSGA-II		Pescara, OPUS/NSGA-II	
D, d_{ij}		R^2, d_{ij}	
Q1	1.812	Q1	0.993
Q2	1.823	Q2	0.994
Q3	1.833	Q3	0.995
σ	$5.791 \cdot 10^{-2}$	σ	$3.746 \cdot 10^{-3}$
Min	1.452	Min	0.971
Mean	1.817	Mean	0.994
Max	1.874	Max	0.998

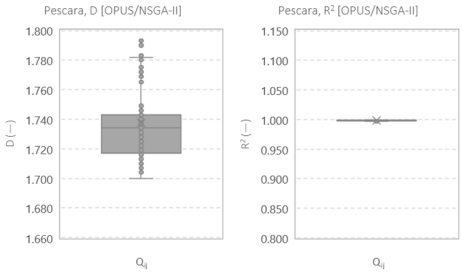


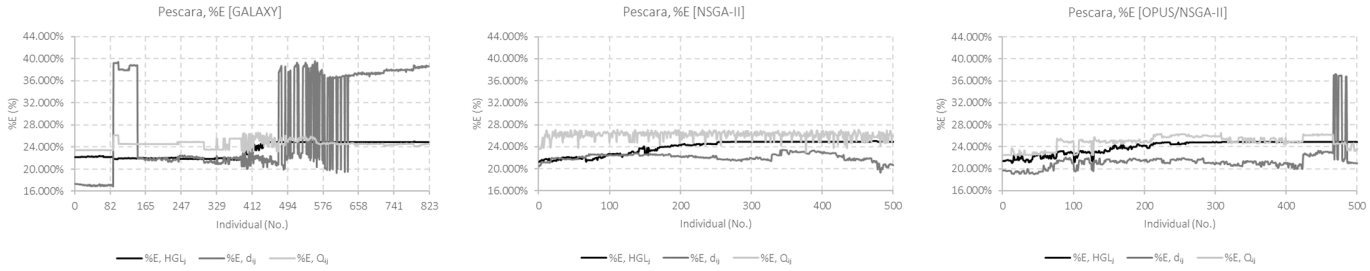
Figure S115. Pescara, OPUS/NSGA-II, box whiskers plots, w_j = Q_{ij}: (a) fractal dimensions (D); (b) determination coefficients (R^2).

Table S64. Pescara, OPUS/NSGA-II, statistics, w_j = Q_{ij}: (a) fractal dimensions (D); (b) determination coefficients (R^2).

Pescara, OPUS/NSGA-II		Pescara, OPUS/NSGA-II	
D, Q_{ij}		R^2, Q_{ij}	
Q1	1.717	Q1	0.998
Q2	1.734	Q2	0.998
Q3	1.743	Q3	0.999
σ	$2.609 \cdot 10^{-2}$	σ	$5.273 \cdot 10^{-4}$
Min	1.700	Min	0.997
Mean	1.738	Mean	0.998
Max	1.793	Max	0.999

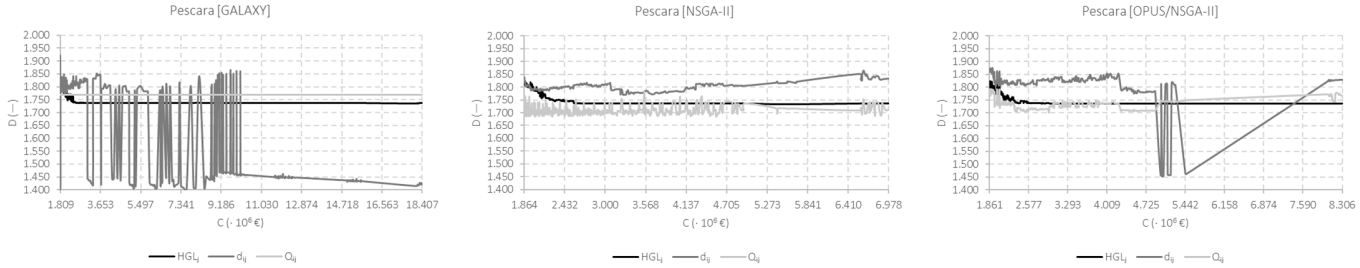
3.2.4.4. Analysis of Results

Figure S116 shows the percent error (%E) between the fractal dimension of the Optimal Hydraulic Gradient Surface (OHGS) with respect to the computed fractal dimensions (D) considering each hydraulic criterion (w_j) by case study. Figure S117 shows the relationship between the computed fractal dimensions (D) and the constructive cost (C) of each design solution by case study. Table S65 shows the reason between the fractal dimensions (D) of the minimum constructive cost (C) individual and the maximum constructive cost (C) individual by design methodology.



(a) *(b)* *(c)*

Figure S116. Percent error (%E) between the fractal dimension of the Optimal Hydraulic Gradient Surfaces (OHGS) and the computed fractal dimensions (D): Pescara (a) GALAXY; (b) NSGA-II; (c) OPUS/NSGA-II.



(a) *(b)* *(c)*

Figure S117. Relationship between the fractal dimensions (D) and the constructive costs (C): Pescara (a) GALAXY; (b) NSGA-II; (c) OPUS/NSGA-II,

Table S65. Reason between the fractal dimension (D) of the minimum and maximum constructive cost (C) individual: Pescara (a) GALAXY; (b) NSGA-II; (c) OPUS/NSGA-II.

Pescara					
GALAXY		NSGA-II		OPUS/NSGA-II	
w_j	$D_{min(C)}/ D_{max(C)}$	w_j	$D_{min(C)}/ D_{max(C)}$	w_j	$D_{min(C)}/ D_{max(C)}$
HGL_j	1.036	HGL_j	1.048	HGL_j	1.046
d_{ij}	1.344	d_{ij}	1.003	d_{ij}	1.016
Q_{ij}	1.015	Q_{ij}	1.032	Q_{ij}	1.015

3.3. Analysis of D

Figure S118 shows the computed D magnitudes derived from NSGA-II designs with individuals arranged from minimum to maximum cost (C). With great significance, Figure S118 shows that D exhibits a nearly constant behavior among all hydraulic criteria (w_j) and marginal sensitivity inside the interval $D \in [1, OHGS]$. Note that Hanoi showed a constant magnitude of $Dd_{ij} = 1.791$ through all iterations, indicating that, in this case, the algorithm repeatedly captured a fractal described by this magnitude of D. The fractal behavior of NSGA-II is strong, given that $R^2 > 0.99$ through all iterations.

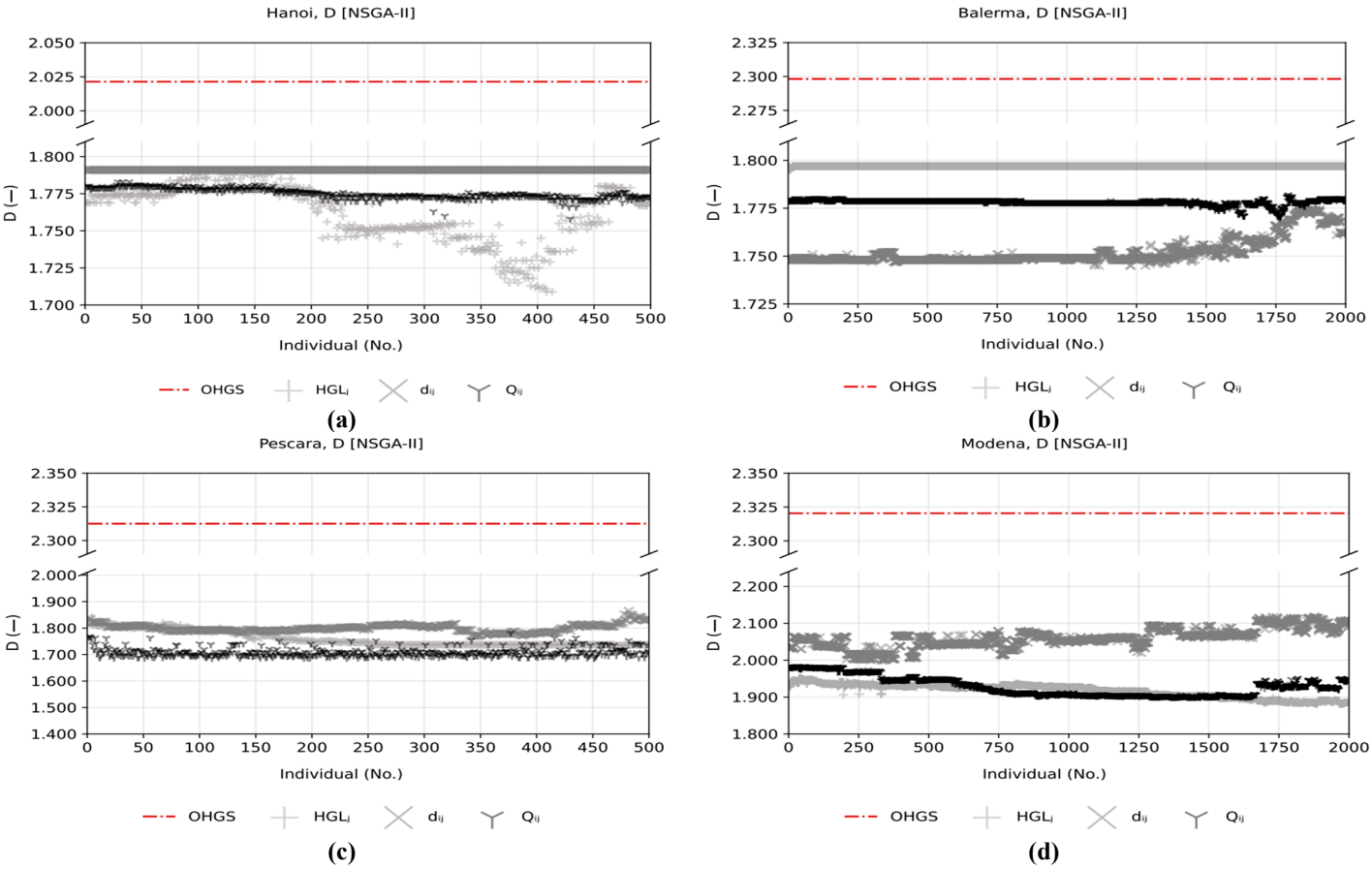


Figure S118. Fractal dimensions (D) computed from the NSGA-II design outcomes considering their energy ($w_j = HGL_j$), infrastructure ($w_j = \Sigma_i d_{ij}$) and flow ($w_j = \Sigma_i Q_{ij}$) distributions: (a) Hanoi; (b) Balerma; (c) Pescara; and (d) Modena.

Figure S119 shows the computed D magnitudes derived from OPUS/NSGA-II designs with individuals arranged from minimum to maximum cost (C). With great significance, Figure S119 derives the same conclusions as for NSGA-II., i.e., D is nearly constant and shows marginal sensitivity to the increase in cost of a WDS inside the interval $D \in [1, OHGS]$. As in the case of NSGA-II, $Dd_{ij} = 1.791$ of Hanoi was consistent among all iterations. D results are similar between NSGA-II and OPUS/NSGA-II, but note that the infrastructural criterion in OPUS/NSGA-II showed weaker fractal behavior in Pescara, where $Dd_{ij} \in [1.452, 1.874]$, a greater interval with lower D magnitudes coupled with lower determination coefficients that lie within the range $R^2 \in [0.971, 1.000]$, indicating that the infrastructural distribution of diameters (d) of Pescara exhibits a weaker fractal behavior with respect to the infrastructural distribution of diameters (d) of the other case studies. Even if Pescara exhibits a weaker fractal behavior, all analyzed fractals show strong fractal behavior, given that $R^2 > 0.97$ through all iterations.

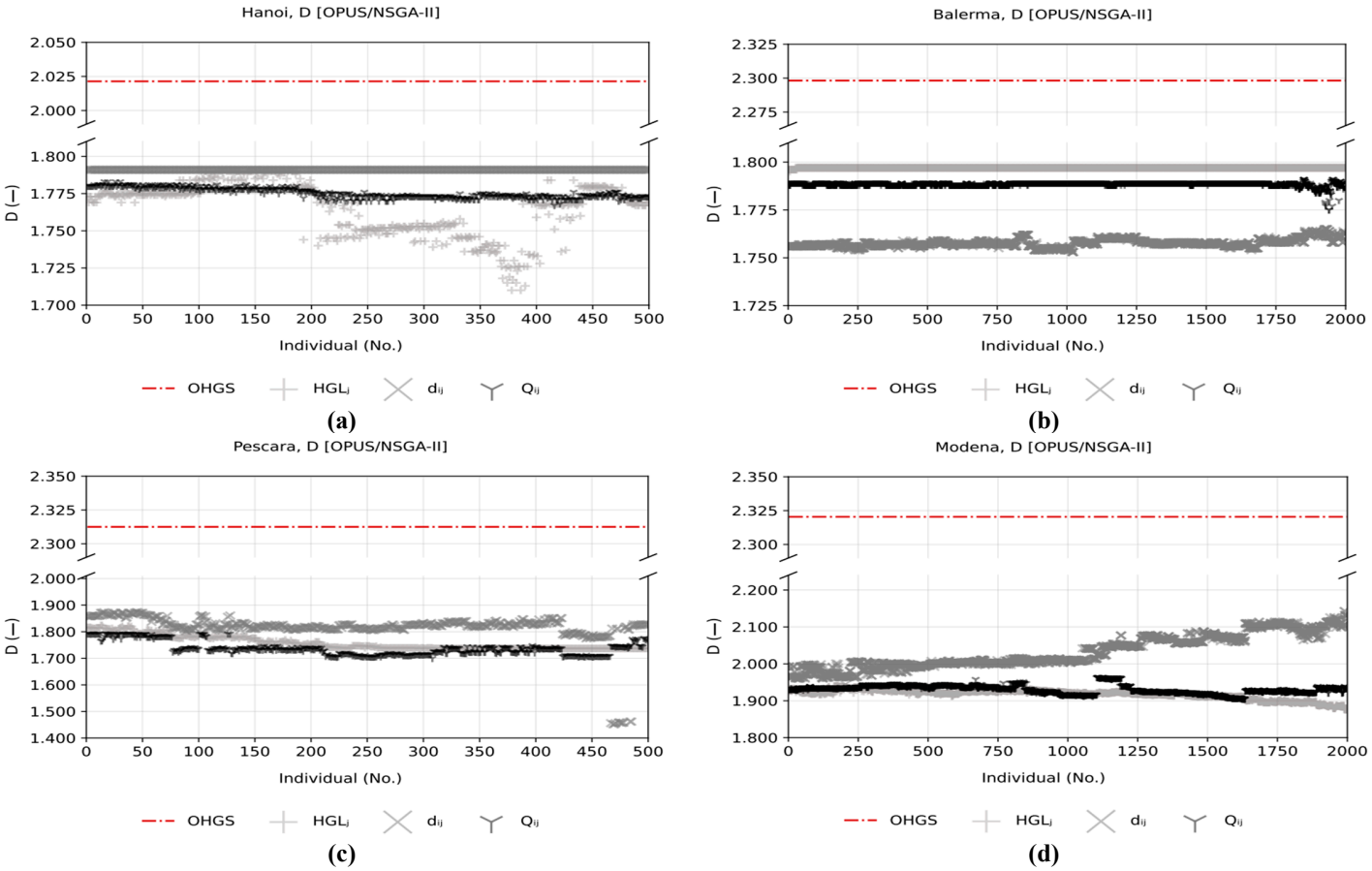


Figure S119. Fractal dimensions (D) computed from the OPUS/NSGA-II design outcomes considering their energy ($w_j = HGL_j$), infrastructure ($w_j = \Sigma_i d_{ij}$) and flow ($w_j = \Sigma_i Q_{ij}$) distributions: (a) Hanoi; (b) Balerma; (c) Pescara; and (d) Modena.

Figure S120 shows the computed D magnitudes derived from GALAXY designs with individuals arranged from minimum to maximum cost (C). With great significance, Table S4 and Figure S7 indicate that D is nearly constant and shows marginal sensitivity to the increase in cost of a WDS inside the interval $D \in [1, OHGS]$. Results from GALAXY show a similar behavior in comparison to NSGA-II and OPUS/NSGA-II. As in OPUS/NSGA-II, the infrastructural criterion of Pescara showed weaker fractal behavior symbolized by lower D magnitudes that lie within the range $Dd_{ij} \in [1.400, 1.922]$. At the same time, all D values are coupled with robust determination coefficients greater than $R^2 > 0.95$, $R^2 \in [0.99, 1.000]$. Given that the design steps of GALAXY differ from NSGA-II and OPUS/NSGA-II, Figure S120 shows different patterns of marginal sensitivity in the computed D magnitudes. However, these patterns do not follow a particular tendency, and the same is true for NSGA-II and OPUS/NSGA-II. Hence, the marginal sensitivity is not explained by the cost (C) or the arrangement of diameters (d) producing a particular HGS, and neither by the design methodology. From this preliminary observation, a correlation between cost (C), resilience (NRI) and D is not evident.

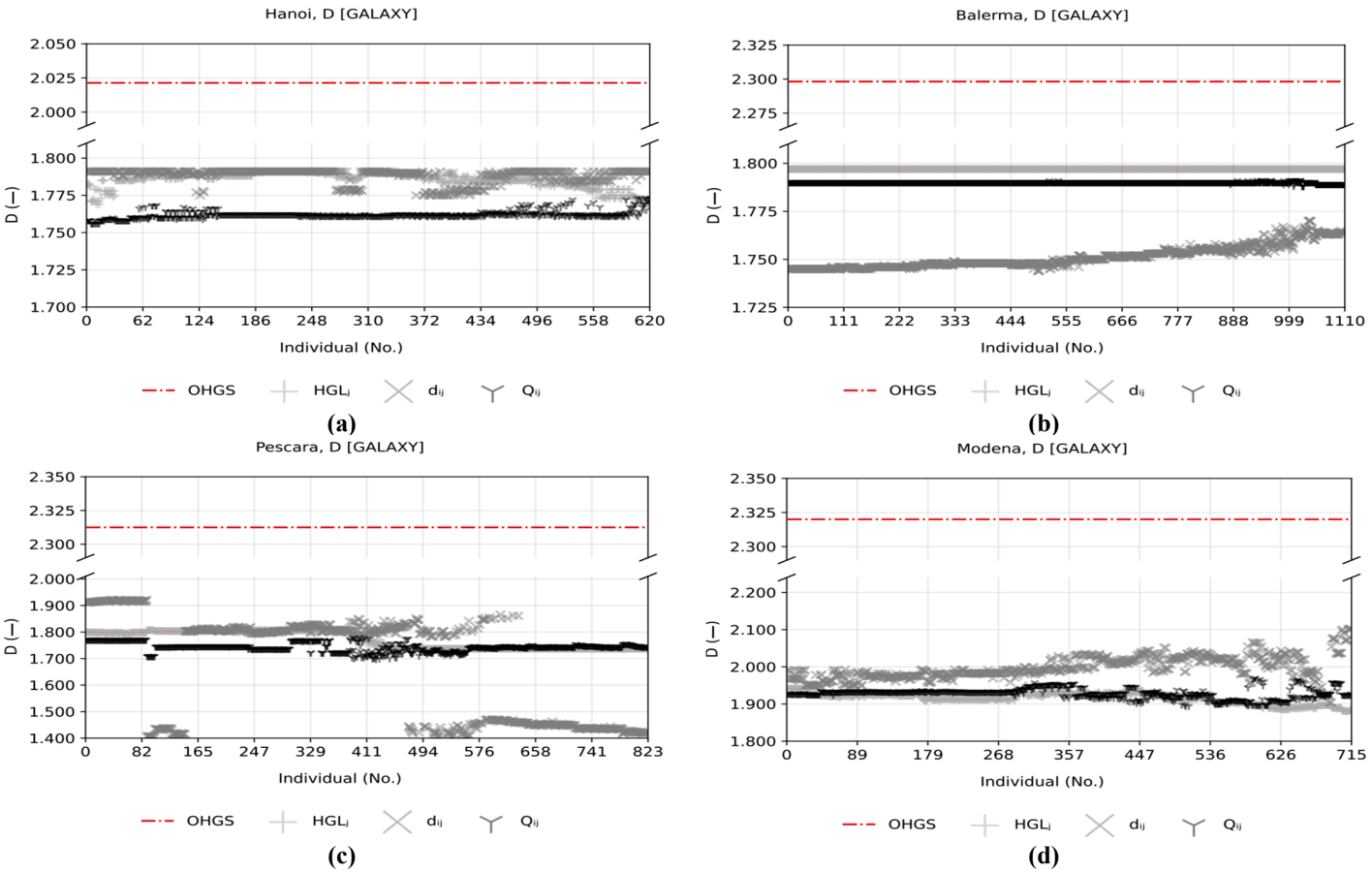
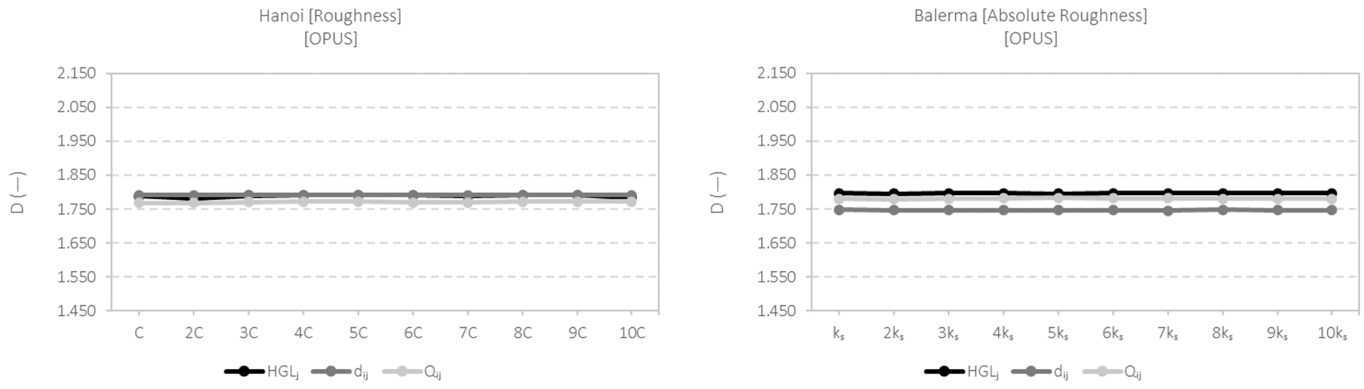


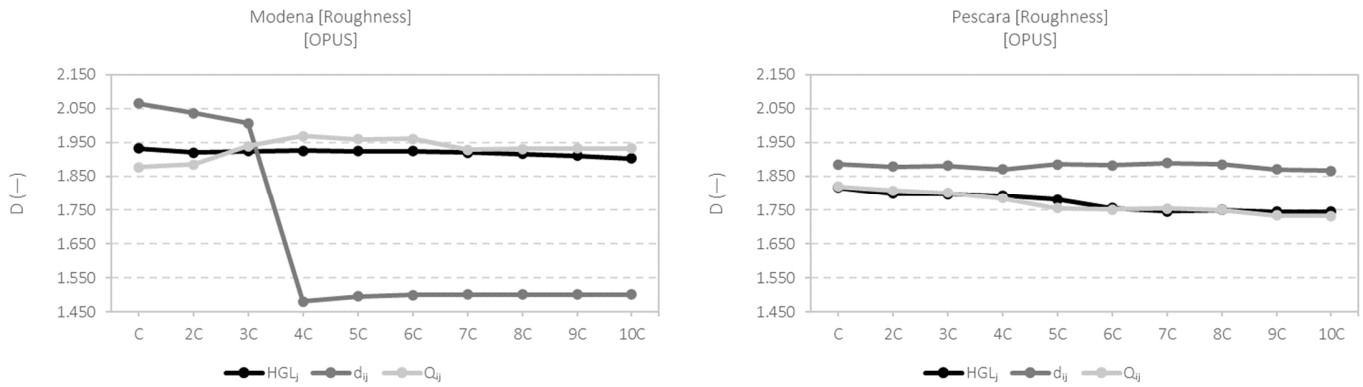
Figure S120. Fractal dimensions (D) computed from the GALAXY design outcomes considering their energy ($w_j = HGL_j$), infrastructure ($w_j = \Sigma_i d_{ij}$) and flow ($w_j = \Sigma_i Q_{ij}$) distributions: (a) Hanoi; (b) Balerma; (c) Pescara; and (d) Modena.

4. Sensitivity Analysis

4.1. Pipe Roughness Sensitivity

Figure S121 shows the results of the pipe roughness sensitivity analysis performed on the mono-objective Optimal Power Use Surface (OPUS) designs calculated varying the pipe roughness magnitudes of the case studies considered in this research.



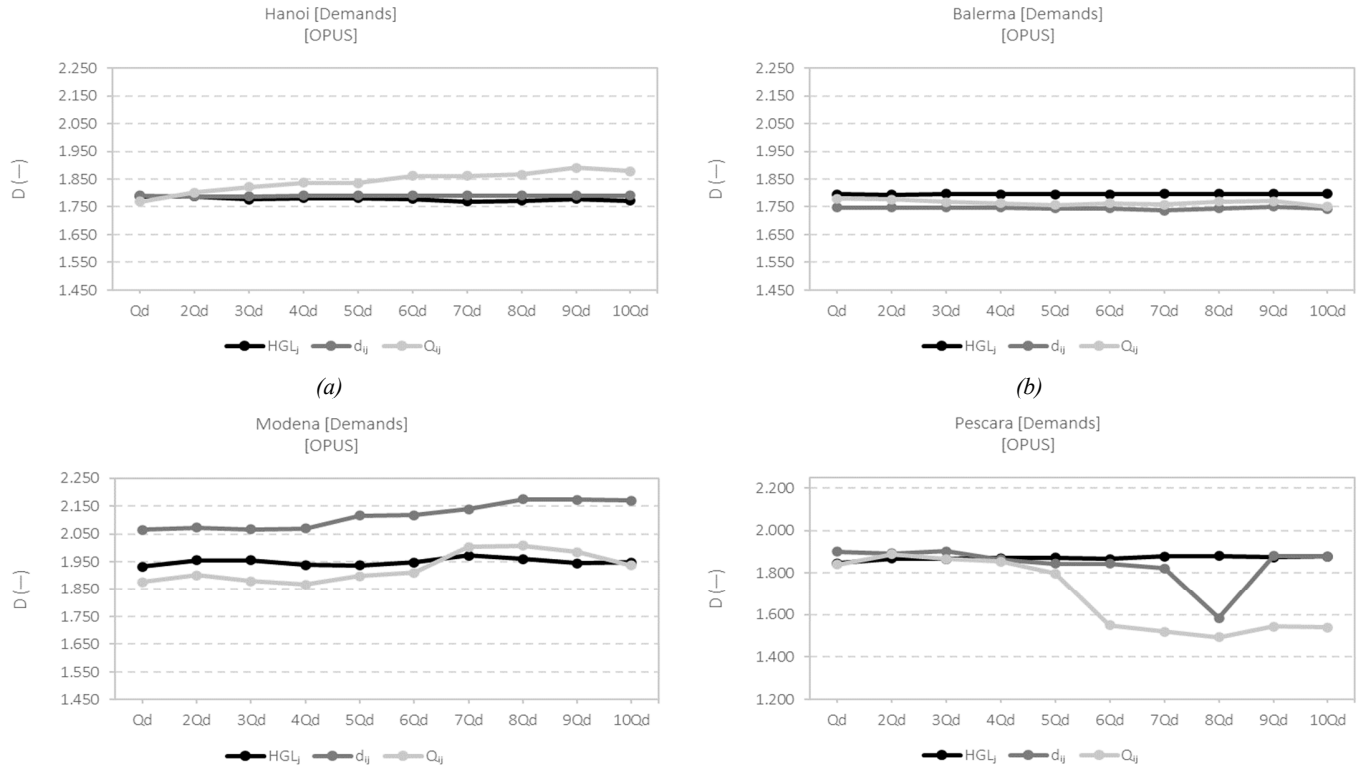


(c) *(d)*

Figure S121. Pipe roughness sensitivity analysis: (a) Hanoi; (b) Balerma; (c) Modena; (d) Pescara.

4.2. Water Demands Sensitivity

Figure S122 shows the results of the water demands sensitivity analysis performed on the mono-objective Optimal Power Use Surface (OPUS) designs calculated varying the water demand magnitudes at the demand nodes of the case studies considered in this research.



(a) *(b)*

(c) *(d)*

Figure S122. Water demands sensitivity: (a) Hanoi; (b) Balerma; (c) Modena; (d) Pescara.

5. Computational Complexity

Table S66 shows the characteristics of the computer devices employed in this research.

Table S66. Properties of the computational devices employed in this research.

Device properties	Number of devices
CPU: Intel® Xeon® Silver 4216, 2.10 GHz (2). RAM: 256 GB	4
CPU: Intel® Core™ i9-12900KF, 3.20 GHz (1). RAM: 64 GB	1
CPU: Intel® Core™ i5-10300H, 2.59 GHz (2). RAM: 16 GB	1
CPU: Intel® Core™ i5-1240P, 1.70 GHz (2). RAM: 16 GB	1
CPU: AMD Ryzen™ 5 2500U, 2.00 GHz (1). RAM: 8 GB	1
CPU: Intel® Core™ i5, 1.40 GHz (2). RAM: 4 GB	1

Table S67 shows the number of individuals considered to perform fractal analysis by criterion and (w_j) and study case. These individuals correspond to the non-dominated solutions of the Pareto Fronts obtained by the application of the bi-objective methodologies considered in this study. Note that these number of iterations only refer to the total number individuals obtained from the bi-objective methodologies. However, each implementation of the box-covering algorithm varied its own number of iterations given its ability to identify an individual as a clear fractal body and given the maximum number of iterations that was imposed to avoid computational power abuse. Therefore, the total number of iterations performed in this research is much greater than the number displayed at the end of Table S67.

Table S67. Total number of iterations on the design individuals performed in this research.

Benchmark	Methodology	Criterion	Individuals	Iterations	%	Status	
Hanoi	Galaxy	HGL	621	621	100%	Complete	Complete
		d	621	621	100%		
		Q	621	621	100%		
	NSGA-II	HGL	500	500	100%	Complete	
		d	500	500	100%		
		Q	500	500	100%		
	OPUS/NSGA-II	HGL	500	500	100%	Complete	
		d	500	500	100%		
		Q	500	500	100%		
Balerma	Galaxy	HGL	1109	1109	100%	Complete	Complete
		d	1109	1109	100%		
		Q	1109	1109	100%		
	NSGA-II	HGL	2000	2000	100%	Complete	
		d	2000	2000	100%		
		Q	2000	2000	100%		
	OPUS/NSGA-II	HGL	2000	2000	100%	Complete	
		d	2000	2000	100%		
		Q	2000	2000	100%		
Modena	Galaxy	HGL	715	715	100%	Complete	Complete
		d	715	715	100%		
		Q	715	715	100%		
	NSGA-II	HGL	2000	2000	100%	Complete	
		d	2000	2000	100%		
		Q	2000	2000	100%		
	OPUS/NSGA-II	HGL	2000	2000	100%	Complete	
		d	2000	2000	100%		
		Q	2000	2000	100%		
Pescara	Galaxy	HGL	823	823	100%	Complete	Complete
		d	823	823	100%		
		Q	823	823	100%		

NSGA-II	HGL	500	500	100%	Complete
	d	500	500	100%	
	Q	500	500	100%	
OPUS/NSGA-II	HGL	500	500	100%	Complete
	d	500	500	100%	
	Q	500	500	100%	
Total		39804	39804	100%	Complete

6. Computed Fractal Dimensions

Table S68 shows the final fractal dimension (D) magnitudes concluded from this research. The final fractal dimensions (D) were computed as simple averages of the fractal dimensions (D) by design approach segregated by fractal analysis criterion (w_j). Then, the final fractal dimension (D) in the right portion of Figure S68 was computed as the simple average of the final fractal dimension (D) of the mono-objective, bi-objective approaches, and the sensitivity analysis.

Table S68. Computed fractal dimensions (D).

	w_j	$D_{Mono\text{-}objective}$	$D_{Bi\text{-}objective}$	$D_{Material}$	$D_{Demands}$	D
Hanoi	HGL_j	1.788	1.772 ($\sigma = 0.019$)	1.790 ($\sigma = 0.002$)	1.779 ($\sigma = 0.006$)	1.778 ($\sigma = 0.015$)
	d_{ij}	1.791	1.790 ($\sigma = 0.003$)	1.791 ($\sigma = 0.001$)	1.791 ($\sigma = 0.001$)	
	Q_{ij}	1.769	1.770 ($\sigma = 0.007$)	1.771 ($\sigma = 0.002$)	1.842 ($\sigma = 0.037$)	
Balerma	HGL_j	1.796	1.797 ($\sigma = 0.000$)	1.795 ($\sigma = 0.001$)	1.796 ($\sigma = 0.001$)	1.779 ($\sigma = 0.019$)
	d_{ij}	1.748	1.754 ($\sigma = 0.006$)	1.748 ($\sigma = 0.001$)	1.746 ($\sigma = 0.004$)	
	Q_{ij}	1.781	1.785 ($\sigma = 0.005$)	1.780 ($\sigma = 0.001$)	1.766 ($\sigma = 0.009$)	
Pescara	HGL_j	1.817	1.765 ($\sigma = 0.031$)	1.769 ($\sigma = 0.027$)	1.871 ($\sigma = 0.010$)	1.744 ($\sigma = 0.104$)
	d_{ij}	1.886	1.723 ($\sigma = 0.175$)	1.880 ($\sigma = 0.013$)	1.842 ($\sigma = 0.095$)	
	Q_{ij}	1.819	1.741 ($\sigma = 0.021$)	1.779 ($\sigma = 0.026$)	1.690 ($\sigma = 0.171$)	
Modena	HGL_j	1.932	1.917 ($\sigma = 0.016$)	1.922 ($\sigma = 0.010$)	1.949 ($\sigma = 0.012$)	1.923 ($\sigma = 0.023$)
	d_{ij}	2.065	2.039 ($\sigma = 0.042$)	1.655 ($\sigma = 0.254$)	2.116 ($\sigma = 0.046$)	
	Q_{ij}	1.769	1.930 ($\sigma = 0.020$)	1.932 ($\sigma = 0.031$)	1.927 ($\sigma = 0.053$)	

7. References

Bragalli, C., D'Ambrosio, C., Lee, J., Lodi, A., & Toth, P. (2012). On the optimal design of water distribution networks: a practical MINLP approach. *Optimization and Engineering*, *13*(2), 219–246. https://doi.org/10.1007/s11081-011-9141-7

Deb, K., Pratap, A., Agarwal, S., & Meyarivan, T. (2002). A fast and elitist multiobjective genetic algorithm: NSGA-II. *IEEE Transactions on Evolutionary Computation*, *6*(2), 182–197. https://doi.org/10.1109/4235.996017

Fujiwara, O., & Khang, D. B. (1990). A two-phase decomposition method for optimal design of looped water distribution networks. *Water Resources Research*, *26*(4), 539–549. https://doi.org/10.1029/WR026i004p00539

Páez, D., Salcedo, C., Garzón, A., González, M. A., & Saldarriaga, J. (2020). Use of Energy-Based Domain Knowledge as Feedback to Evolutionary Algorithms for the Optimization of Water Distribution Networks. *Water*, *12*(11), 3101. https://doi.org/10.3390/w12113101

Reca, J., & Martínez, J. (2006). Genetic algorithms for the design of looped irrigation water distribution networks. *Water Resources Research*, *42*(5). https://doi.org/10.1029/2005WR004383

Saldarriaga, J., Páez, D., Salcedo, C., Cuero, P., López, L. L., León, N., & Celeita, D. (2020). A Direct Approach for the Near-Optimal Design of Water Distribution Networks Based on Power Use. *Water*, *12*(4), 1037.

Wang, Q., Guidolin, M., Savic, D., & Kapelan, Z. (2015a). Two-Objective Design of Benchmark Problems of a Water Distribution System via MOEAs: Towards the Best-Known Approximation of the True Pareto Front. *Journal of Water Resources Planning and Management*, *141*(3). https://doi.org/10.1061/(ASCE)WR.1943-5452.0000460

Wang, Q., Savić, D. A., & Kapelan, Z. (2017). GALAXY: A new hybrid MOEA for the optimal design of Water Distribution Systems. *Water Resources Research*, *53*(3), 1997–2015. https://doi.org/10.1002/2016WR019854